

FACULTY
OF MATHEMATICS
AND PHYSICS
Charles University

DOCTORAL THESIS

Martin Labuta

Assessment of three-dimensional site effects using seismic ambient vibrations

Institute of Geophysics of the Czech Academy of Science

Supervisor of the doctoral thesis: RNDr. Jan Burjánek, Ph.D.
Study programme: Physics of the Earth and Planets

Prague 2025

I declare that I carried out this doctoral thesis on my own, and only with the cited sources, literature and other professional sources. I understand that my work relates to the rights and obligations under the Act No. 121/2000 Sb., the Copyright Act, as amended, in particular the fact that the Charles University has the right to conclude a license agreement on the use of this work as a school work pursuant to Section 60 subsection 1 of the Copyright Act.

In ..... date ....

Author's signature

I would like to express my deepest gratitude to my supervisor, Dr. Jan Burjánek, for his unwavering support, guidance, and inspiration throughout the course of my doctoral studies. His expertise, encouragement, and insightful feedback have been invaluable to the completion of this thesis. I am sincerely thankful for his patience, motivation, and for always challenging me to reach higher standards in my research. This work would not have been possible without his dedicated mentorship. I also wish to dedicate this thesis to my wife, Anita Szabó, and my brother, Ondřej Šoupal, for their constant support and invaluable assistance during field work. My heartfelt thanks go to my mother, Jana Šoupalová, for her unwavering encouragement and support throughout my studies. Special thanks are due to Ivo Opršal and David Aaron Landa for their contributions and help with the published articles. I am also grateful to Radek Klanica and Roman Beránek for their assistance with electric resistivity tomography, and to Jan Mrlina for his expertise and help with the gravimetric survey. Furthermore, I would like to thank Diana Konrádová, Jakub Pokorný, and Josef Müller for their help with field measurements. Their support, collaboration, and dedication have been instrumental in the successful completion of this work. This work was supported by Czech Science Foundation (GACR), project no. GA20-15818S, and by the Ministry of Education, Youth and Sports of the Czech Republic through the e-INFRA CZ (ID:90140).

Title: Assessment of three-dimensional site effects using seismic ambient vibrations

Author: Martin Labuta

Institute: Institute of Geophysics of the Czech Academy of Science

Supervisor: RNDr. Jan Burjánek, Ph.D., Institute of Geophysics of the Czech Academy of Science

Abstract: This dissertation investigates the influence of local geological structures on seismic wave propagation, with a focus on phreatomagmatic craters (so-called maars) in the West Bohemia region. The research primarily focuses on the Mýtina maar, where ambient seismic noise measurements and their numerical modeling were used to analyze subsurface structures and validate the methodological approach. At the newly identified maars of Nežichov and Sepuska, a broader range of methods was applied—including ambient seismic noise measurements, numerical modeling, gravimetric surveys, and electrical resistivity tomography—which enabled a detailed characterization of their geological features and a comparative analysis. The results show that the internal infill of maar craters, typically forming conical structures, significantly amplifies seismic waves, with the amplification characteristics strongly dependent on their geometry and sedimentary composition. Numerical models of seismic response confirm that the elliptical cross-section of the maar leads to the splitting of resonance frequencies along the principal axes of symmetry. The simulated response corresponds well with observed data and allows estimation of structural geometry at depths beyond the reach of conventional geophysical methods. Preliminary studies at other sites, such as Ztracený rybník, Bažina, and Neualbenreuth, suggest that the presence of peat layers within the infill contributes to even greater amplification effects. The results of this work confirm that the combination of ambient seismic noise analysis and 3D modeling of seismic response represents an effective tool for imaging subsurface volcanic structures and assessing local seismic hazards, while also providing a solid foundation for further research in similar geological settings.

Keywords: ambient vibrations, numerical modeling, field measurements, data analysis

Název práce: Odhad trojdimenzionálních lokálních efetků ze seismického neklidu

Autor: Martin Labuta

Ústav: Geofyzikální ústav AV ČR, v.v.i.

Vedoucí dizertační práce: RNDr. Jan Burjánek, Ph.D., Geofyzikální ústav AV ČR, v.v.i.

Abstrakt: Tato dizertační práce zkoumá vliv lokálních geologických struktur na šíření seismických vln se zaměřením na freatomagmatické krátery (tzv. maary) v oblasti západních Čech. Předmětem výzkumu byl především maar Mýtina, kde byla k analýze podpovrchové struktury a ověření metodického postupu využita měření seismického šumu a jejich numerické modelování. U nově identifikovaných maarů (Nežichov a Sepuska) byla následně aplikována širší škála metod – měření seismického šumu, numerické modelování, gravimetrický průzkum a elektrická rezistivitní tomografie – což umožnilo detailní popis jejich geologických vlastností a srovnávací analýzu. Výsledky ukazují, že vnitřní výplně maarových kráterů, které typicky tvoří kuželovité struktury, významně zesilují seismické vlny, přičemž charakter tohoto zesílení výrazně závisí na jejich geometrii a sedimentárním složení. Numerické modely seismické odezvy potvrzují, že eliptický průřez maaru vede k rozdělení rezonančních frekvencí podél hlavních os symetrie. Simulovaná odezva dobře odpovídá pozorovaným datům a umožňuje odhadnout tvar struktury i ve větších hloubkách, než je obvykle dosažitelné tradičními geofyzikálními metodami. Předběžné studie na dalších lokalitách, jako jsou maary Ztracený rybník, Bažina a Neualbenreuth, naznačují, že přítomnost rašelinné vrstvy ve výplni přispívá k ještě výraznějšímu zesílení. Výsledky práce potvrzují, že kombinace analýzy seismického šumu a 3D modelování seismické odezvy představuje účinný nástroj pro zobrazování podpovrchových sopečných struktur a vyhodnocení lokálního seismického ohrožení, a zároveň poskytují pevný základ pro další výzkum v obdobných geologických prostředích.

Klíčová slova: seismický neklid, numerické modelování, terénní měření, analýza dat,

Contents

1 Introduction **8**
- 1.1 Introduction to local seismic site effects . . . 9
- 1.2 Maar volcanic structure . . . 10
- 1.3 Geological and tectonic settings of West Bohemia . . . 11
  - 1.3.1 A brief geological history of the Bohemian Massif . . . 12
  - 1.3.2 Eger rift . . . 14
  - 1.3.3 Selected fault zones of the Western Bohemian Massif related to volcanic and seismic activity . . . 16
  - 1.3.4 Maar diatreme volcanoes in West Bohemia . . . 16
- 1.4 Analysis methods for ambient vibrations in maar crater infills . . . 19
  - 1.4.1 Site-to-Reference Spectral Ratio (SRSR) . . . 20
  - 1.4.2 Horizontal-to-Vertical Spectral Ratio (HVSR) . . . 21
  - 1.4.3 Frequency Domain Decomposition (FDD) . . . 21
  - 1.4.4 Time Frequency Polarization Analysis (TFPA) . . . 22
  - 1.4.5 Frequency-wavenumber (F-K) analysis and the shear velocity inversion from a dispersion curve . . . 22
- 1.5 Numerical modeling of maars' ambient vibrations . . . 23
  - 1.5.1 SW4 settings and properties . . . 24
  - 1.5.2 Synthetic ambient noise generation . . . 27
  - 1.5.3 Example of numerical modeling of Mýtina maar . . . 27
- 1.6 Content of this thesis . . . 28

2 Modelling the seismic response of the Mýtina maar volcanic structure **29**
- 2.1 Introduction . . . 29
- 2.2 Methods . . . 30
  - 2.2.1 The frequency-wavenumber array analysis method . . . 30
  - 2.2.2 The inversion for the seismic velocity profiles . . . 30
  - 2.2.3 The site-to-reference spectral ratio (SRSR) . . . 30
  - 2.2.4 Ambient vibration simulations . . . 31
- 2.3 Field experiments . . . 31
- 2.4 Results . . . 32
  - 2.4.1 Array analysis . . . 32
  - 2.4.2 Development of the 3D model . . . 34
  - 2.4.3 Synthetic seismic noise analysis . . . 36
  - 2.4.4 Comparison with the observed data . . . 40
- 2.5 Discussion . . . 42
- 2.6 Conclusions . . . 44
- 2.7 Acknowledgements . . . 45
- 2.8 Supplementary material . . . 45

3 Ambient Vibrations of a Deep Maar Resonator **50**
- 3.1 Introduction . . . 50
- 3.2 Geological setting . . . 52
- 3.3 Methods used to process ambient seismic noise . . . 52

3.3.1 Site-to-reference spectral ratio (SRSR) . . . 52
3.3.2 Frequency domain decomposition (FDD) . . . 53
3.3.3 Time frequency polarization analysis (TFPA) . . . 53
3.3.4 Horizontal-to-vertical spectral ratio (HVSR) . . . 54
3.3.5 Numerical modelling . . . 54
3.4 Field experiments . . . 54
3.5 Results . . . 56
3.6 Discussion . . . 59
3.7 Conclusions . . . 64
3.8 Acknowledgements . . . 65
3.9 Supplementary material . . . 65

4 3D Resonance and Subsurface Structure of Newly Identified Felsic Maar-Diatremes in West Bohemia: A Multidisciplinary Geophysical Approach 72
4.1 Introduction . . . 72
4.2 Methods . . . 74
4.2.1 Methods for processing the ambient seismic noise . . . 74
4.2.2 Time frequency polarization analysis (TFPA) . . . 75
4.2.3 Numerical modeling . . . 76
4.2.4 Gravimetry . . . 77
4.2.5 Electric resistivity tomography (ERT) . . . 77
4.3 Field experiments . . . 77
4.3.1 Ambient seismic noise survey . . . 77
4.3.2 Gravity survey . . . 79
4.3.3 ERT . . . 79
4.4 Results . . . 79
4.4.1 Ambient noise processing for both structures . . . 79
4.4.2 Gravimetric processing for both structures . . . 86
4.4.3 Electric resistivity tomography . . . 87
4.4.4 Numerical modeling of seismic response . . . 88
4.5 Discussion . . . 90
4.6 Conclusion . . . 92

5 Concluding remarks and Future Directions 94

Bibliography 99

List of Publications 110

1 Introduction

The topic of the thesis is how local geological conditions influence the propagation of seismic waves and how we can utilize it to constrain the shape and dimensions of the local subsurface structures. We based our study on recordings and analysis of ambient vibrations, which are low-amplitude ground motions caused by natural and anthropogenic sources in the environment (Bonnefoy-Claudet et al., 2006). By measuring these vibrations, we can create a three-dimensional model of the subsurface, identifying variations in soil and rock properties that affect seismic wave behavior (Wathelet et al., 2004). This approach is also valuable for understanding site-specific seismic hazards, as it helps predict how different areas might amplify or attenuate seismic energy during an earthquake. Such assessments are then crucial for designing earthquake-resistant structures and improving urban planning in seismically active regions.

Our research focuses on understanding local site effects associated with maar volcanoes, particularly in the western part of the Bohemian Massif. In this chapter, we briefly outline motivation of the study, introduce the local seismic site effects, the geological setting of the studied area and characteristics of maar volcanoes, which are essential for our investigations. We also briefly introduce the methods we apply, and in particular, the numerical method which is used for the simulation of synthetic ambient vibrations which are still not so common in practice.

Maar diatreme volcanoes represent a distinctive and globally distributed type of monogenetic volcano (White & Ross, 2011), frequently encountered across diverse geological settings. Studying maar volcanoes in general is important for understanding volcanic activity and related hazards in a given area (Lorenz, 2007). Maar volcanoes are formed through explosive interactions between magma and groundwater, known as phreatomagmatic eruptions. These eruptions are sudden and violent, posing significant risks to nearby communities (Valentine & White, 2012). By examining existing maar volcanoes generated during past eruptions, we can gain insights into the mechanisms driving these eruptions, which helps improve hazard assessments and develop better predictive models (Dellino et al., 2011). This knowledge is essential for implementing effective safety measures and emergency response strategies in areas where maar volcanoes are likely in future (Brand et al., 2014).

Additionally, maar volcanoes offer valuable geological insights into the subsurface environment (Lorenz, 2003). The formation of a maar involves the excavation of a crater, which can expose layers of rock and sediment that provide information about the geological history of an area (Skilling et al., 2002). This can be particularly useful for understanding the composition and structure of the Earth's crust, as well as the presence of aquifers and other subsurface features (Sebazungu, 2006). Such information is important for geological research and resource exploration, including the search for minerals and groundwater (Jousset et al., 2011).

Moreover, maar volcanoes often create and preserve a time track of unique ecosystems. After an eruption, many maar craters become lakes, fostering diverse habitats that support a wide range of plant and animal life (Tavsanoglu et al., 2015). Studying these ecosystems can provide insights into the development of ecological succession, biodiversity, and the interactions between different species in

time (Brauer et al., 1999). Further, paleopalynology, the study of fossilized pollen and spores, can be used to reconstruct past vegetation and climate conditions in these maar lake sediments (Lirer et al., 2013). This research can contribute to conservation efforts and enhance our understanding of how ecosystems develop and adapt over time (Hessen et al., 2023).

1.1 Introduction to local seismic site effects

Seismic site effects refer to the phenomenon where the characteristics of earthquake ground motion are significantly modified by the local geological conditions beneath and near a specific site (Bard et al., 1999). This modification typically involves the amplification of seismic waves as they propagate through superficial geological layers, particularly soft sediments, leading to increased ground shaking at the surface (Field & Jacob, 1995). These altered ground motions can exhibit higher amplitudes, longer durations, and different frequency contents compared to the seismic waves propagating through the underlying bedrock (Borcherdt, 1994). The study of these local site effects is a crucial component of assessing strong ground motions, evaluating seismic hazards (Assimaki et al., 2008). Initial theoretical analyses of seismic site effects often employed simplified one-dimensional (1D) models, which assumed that the geological layers were horizontal and that seismic waves propagated vertically through these layers (Kawase & Aki, 1989). However, the assumption of purely horizontal layering is often an oversimplification of actual geological settings, especially when considering complex features such as sedimentary basins and irregular topography (Steidl et al., 1996). Sedimentary basins, with their intricate three-dimensional geometry of alluvial fillings, can trap and amplify seismic waves in ways that cannot be captured by 1D models, giving rise to what are known as 2D/3D effects (Graves et al., 1998). Similarly, surface irregularities like hills, ridges, and valleys introduce another variation in ground motion due to the focusing and scattering of seismic waves (Spudich et al., 1996). A fundamental aspect of seismic site effects is the phenomenon of resonance. Resonance occurs when seismic waves of certain frequencies are selectively amplified by superficial geological structures (e.g., layers, basins), particularly if these frequencies are close to the natural vibrational frequencies of the structures. This amplification happens because of the constructive interference of seismic waves that are reflected and refracted within the structure (Aki & Richards, 2002).

Seismic wave attenuation is another phenomenon that strongly modifies the wavefield. As seismic waves radiate outwards from their source, their energy spreads over an increasingly larger area, causing a decrease in wave amplitude known as geometrical attenuation (Aki & Richards, 2002). In addition to the geometrical spreading, seismic waves also lose energy as they travel through the Earth's materials due to internal friction, scattering, and other energy dissipation mechanisms within the medium. This process is referred to as material or intrinsic attenuation and contributes to the overall decay in wave amplitude with the propagation distance (Mitchell & Xie, 1994). The intrinsic attenuation is more pronounced in the uppermost crust.

The seismic impedance contrast between the relatively soft near-surface layers and the underlying, stiffer bedrock is a primary factor in trapping seismic waves and causing them to reverberate, leading to significant amplification (Dobry et al.,

1976). Therefore, distribution of shear wave velocity (Vs) is a key parameter, which controls the development of site effects. Several geological factors contribute to the existence and characteristics of so-called three-dimensional (3D) local seismic site effects (Olsen, 2000). These primarily include the presence and properties of sedimentary basins, complex subsurface structures like salt diapirs (Kühn et al., 2011), and specific form of rock damage or weathering – for example, rock fracturing, found at unstable rock slopes (e.g., Burjánek et al. 2019). The geometry of a basin, including its depth, width, and overall shape, plays a crucial role in determining the level of ground motion amplification and the specific frequencies that are most affected (Komatitsch et al., 2002). In deeper and narrower basins, often characterized by a high shape ratio (the ratio of maximum sediment thickness to half the basin width), resonance of the entire structures develops, so that they exhibit stronger amplification of seismic waves, particularly in the central parts of the basin (Sato et al., 2012). Conversely, in the relatively wider basins (with respect to the previous case), the maximum amplification may occur closer to the basin edges, where local surface waves are generated that propagate across the basin and further significantly enhance the amplification of ground motion (Kawase & Aki, 1989). This "basin-edge effect" can result in increased damage intensity in relatively narrow zones located near the margins of the basin (Bard et al., 1999). Furthermore, the presence of steep interfaces at the basin edges can effectively reflect high-frequency seismic waves, contributing to complex interference patterns (Kawase, 1996). The internal structure of a sedimentary basin, including variations in the thickness and seismic wave velocity of the sediments, can further complicate the propagation and amplification of seismic waves (Olsen, 2000).

Topographical factors, related to the shape and form of the Earth's surface, are another contributors to three-dimensional local seismic site effects. Surface irregularities, such as hills and ridges, can focus seismic waves and leading to increased amplitudes of ground motion, particularly at the crests of these features (Spudich et al., 1996). The degree of amplification can vary depending on the azimuth, or the direction of the incoming seismic waves relative to the orientation of the topographical feature (Bard et al., 1999). Conversely, valleys and canyons can trap and reflect seismic waves, potentially leading to either amplification or de-amplification of ground motion depending on their specific geometry and the characteristics of the incident wavefield (Sanchez-Sesma & Luzon, 1995). Slopes can also influence seismic wave propagation, with amplification often occurring along the slope and de-amplification at the base; steeper slopes may exhibit more pronounced variations in ground motion (Ashford et al., 1997).

1.2 Maar volcanic structure

Maar formation primarily results from explosive interactions between subsurface magma and shallow groundwater—a process known as phreatomagmatic eruption (Lorenz, 1986, 2003, 2007; White & Ross, 2011). Maar-diatreme volcanoes are defined by a broad, shallow crater (the maar) and a subsurface, rock-filled volcanic conduit (the diatreme), both formed through this process (Lorenz, 1975, 1985, 1986). Although often perceived as smaller than stratovolcanoes, maar-diatreme volcanoes are the second most common volcanic type on continents and

islands (Cas & Wright, 1987; Schmincke, 2004; Vespermann & Schmincke, 2000; Wohletz & Heiken, 1992; Wood, 1980)).

The maar crater typically forms below the pre-eruptive ground surface, distinguishing it from other small volcanoes like tuff rings (Lorenz, 1986). These craters are usually bowl-shaped, may contain lakes, and range from tens of meters to several kilometers in diameter (Lorenz, 1986). Their low rims are made of unconsolidated volcanic and country rock fragments ejected during eruptions (Lorenz, 1986, 2007; White & Ross, 2011).

The term "maar" originates from the lake-filled craters of Germany's Eifel region (Steininger, 1819). The presence of water in a maar is closely tied to its formation, reflecting the crucial role of groundwater in the eruption process (Lorenz, 1986). The variability in maar size corresponds to differences in the scale and energy of phreatomagmatic explosions.

Beneath the maar lies the diatreme, a cone-shaped structure filled with fragmented rocks (breccia), extending hundreds of meters to over a kilometer deep (Lorenz, 2007). The diatreme fill comprises both juvenile (magmatic) and lithic (country rock) clasts, often including large blocks and evidence of multiple explosive events. At its base, a root zone marks the transition from the magmatic feeder dike to the fragmented deposits, characterized by irregular forms and deformed dikes (Ross et al., 2017). The diatreme records the eruption's history and disrupts subsurface stratigraphy, reflecting episodic, multi-phase explosions.

Surrounding the maar is the ejecta or tephra ring—a low, broad accumulation of ash, lapilli, and abundant lithic clasts, formed by pyroclastic surges and fallout. Its low height and wide extent distinguish it from other volcanic cones, and its composition provides insight into the disrupted geology during eruption (White & Ross, 2011).

While maar volcanoes are most associated with mafic volcanic rocks (Figure 1.1a), such as basalt, they can also form in association with more felsic compositions like rhyolite or dacite (Figure 1.1b). The key factor is not the magma type itself, but the explosive interaction between magma and groundwater that drives phreatomagmatic eruptions. Mafic magmas tend to be hotter and less viscous, which can favor more vigorous steam explosions, but felsic magmas, despite being cooler and more viscous, can also produce maar-diatreme volcanoes if the conditions for magma-water interaction are met. The resulting maar morphology and deposit characteristics may vary depending on the magma's composition, influencing the grain size, mineralogy, and chemistry of the erupted material. Thus, both mafic and felsic magmas can generate maar volcanoes given suitable hydrological and geological settings (Ross et al., 2017).

1.3 Geological and tectonic settings of West Bohemia

The studied maar diatremes lie in West Bohemia, the main geomorphological unit in this region is the Bohemian Massif (BM). The entire massif exhibits a complex geological history, though the general geophysical research interest lies in the western part due to its ongoing tectonic activity, manifested by phenomena such as Quaternary volcanism (Mrlina et al., 2007), earthquake swarms at the Eger

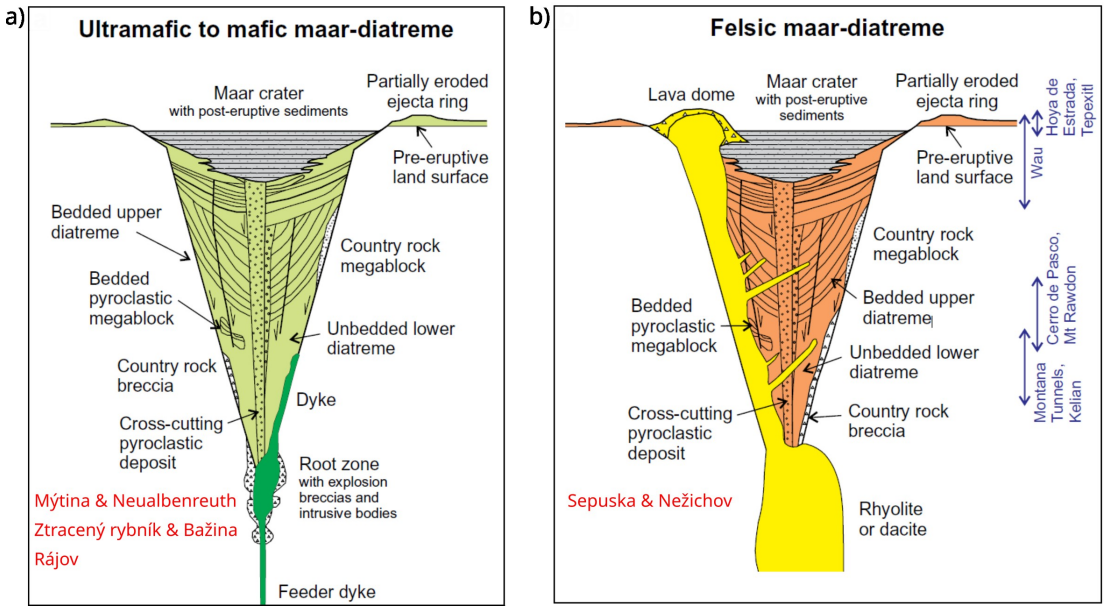


Figure 1.1 Schematic cross-sections of maar diatremes modified after Ross et al. (2017). a) Scheme of a mafic to ultramafic maar diatreme, in West Bohemia that includes Mýtina, Neualbenreuth, Ztracený rybník, Bažina and Rájov. b) Scheme of a felsic maar diatreme, e.g. newly discovered maars Sepuska and Nežichov, where the chemistry of rock material was described by Ulrych et al. (2003).

rift / Leipzig – Regensburg fault zone junction (Fischer et al., 2014), substantial degassing of carbon dioxide (Weinlich et al., 1999), and the migration of crustal fluids (Babuška et al., 2016). The BM is an integral component of the broader European Cenozoic Rift System (ECRIS), a network of rift valleys that developed across Europe in response to the Alpine and Pyrenean orogenies (Dèzes et al., 2004).

1.3.1 A brief geological history of the Bohemian Massif

The geological evolution of the Bohemian Massif spans an extensive period, commencing with the fragmentation of ancient continental crust and the subsequent development of the upper Proterozoic (Brioverian) basin, culminating in the transition to a platform development stage towards the close of the Paleozoic era (Chaloupský, 1989). A significant early tectonic event was the Cadomian Orogeny (approximately 570 to 545 million years ago), which involved the formation of a continental magmatic arc along the periphery of the West African Craton, accompanied by the development of a related back-arc basin. The following arc-continent collision initiated diachronously (variously in time), starting in the east, within the area that would become the Bohemian Massif, around 570 to 560 million years ago.1This period of intense Cadomian tectonism affected the entirety of the Bohemian Massif (Chaloupský, 1989; Linnemann, 2007).

The subsequent Variscan Orogeny (Devonian and Carboniferous periods, 408 to 286 Ma) results from the closure of the Rheic Ocean and the collision between the supercontinents of Gondwana and Laurussia. This orogenic event led to the subdivision of the Bohemian Massif into several distinct tectonic zones, separated by major thrust faults. These zones include the northern Rhenohercynian

Zone (marginal to the massif), the Saxothuringian Zone, and the more internal Moldanubian Zone of Central Europe to the south. The Saxothuringian Zone, forming the northern part of the massif, is characterized by late Neoproterozoic to Lower Carboniferous marine sediments deposited within the Saxothuringian Basin. The Moldanubian Zone, constituting the central parts of the massif, is distinguished by crystalline rocks exhibiting generally higher metamorphic grades and the presence of voluminous granitoid intrusions dating back to approximately 520 million years ago. The Moravian-Silesian Zone is located in the southeast of the massif. The Variscan evolution involved a complex sequence of events, including Late Devonian oceanic subduction and Early Carboniferous continental underthrusting of the Saxothuringicum beneath the Teplá-Barrandian Unit on the western side (Schulmann & Gayer, 2000; Schulmann et al., 2014).

Following the Variscan Orogeny, during the Permian period and onwards, the Variscan mountain belt underwent significant erosion and became partially covered by younger sedimentary deposits. During the Cenozoic era the development of the extensive European Cenozoic Rift System (ECRIS) occurred as a response to the compressional forces exerted by the Alpine and Pyrenean orogenies (Dèzes et al., 2004). The Eger Graben, situated in the western Bohemian Massif, represents the easternmost segment of this rift system and experienced two notable phases of extensional tectonics during the Late Eocene and Early Miocene epochs (Rajchl et al., 2009). Throughout the post-Variscan period, the dominant tectonic regime in the region has been extensional, characterized by normal faulting, the formation of halfgrabens, and the development of graben structures (Ziegler & Dèzes, 2006).

In this context, the volcanic activity in the Eifel volcanic field in western Germany is a significant geological feature linked to the tectonic evolution of the region. The Eifel volcanism began around 45 million years ago during the Tertiary period, coinciding with the major expansion of the Earth's crust related to the formation of the Alps (Ritter et al., 2001). This initial phase formed the Hocheifel volcanic field, centered around the Hohe Acht, the highest mountain in the Eifel. A second, much more recent volcanic phase started about one million years ago and continued until roughly 10,900 years ago, producing the East and West Eifel volcanic fields. These younger fields are characterized by volcanic structures such as maars and lava domes, with the Laacher See volcano in the East Eifel being notable for its massive eruption about 13,000 years ago, which had widespread climatic and environmental impacts across central Europe (Schmincke et al., 1999). The volcanism in the Eifel is related to mantle plume activity beneath the region, with magma sources varying in depth from the upper mantle to deeper zones influenced by this plume, demonstrating ongoing volcanic activity within the European Cenozoic Rift System framework (Hensch et al., 2019).

Similarly, the Massif Central in France represents another important post-Variscan geological and volcanic province. It is an ancient massif that was also affected by Variscan orogeny and later experienced significant erosion and sedimentation. During the Cenozoic, the Massif Central underwent extensive volcanic activity, largely related to the tectonic reactivation and extension associated with the European Cenozoic Rift System and the Alpine orogeny (Merle & Michon, 2001). The volcanic activity in the Massif Central is characterized by a variety of volcanic landforms, including stratovolcanoes, lava domes, and extensive basaltic plateaus. This volcanism reflects the complex interplay between lithospheric exten-

sion, mantle melting, and crustal processes in a post-orogenic setting, contributing to the distinctive landscape of south-central France and providing important insights into the tectono-magmatic evolution of western Europe after the Variscan orogeny (Downes, 1987).

Thus, both the Eifel volcanic field and the Massif Central illustrate the prolonged geological evolution following the Variscan orogeny, where extensional tectonics and mantle dynamics associated with the European Cenozoic Rift System have led to significant volcanic activity and landscape development in western and central Europe.

1.3.2 Eger rift

The Eger Graben depression overlying the rift zone, also referred to as the Ohře Graben, is a prominent geological structure located in the northwestern part of the Czech Republic and extends into eastern Germany (Dèzes et al., 2004). It forms an integral part of the extensive European Cenozoic Rift System (ECRIS), representing its easternmost expression. The ECRIS itself is a vast network of rift valleys stretching over approximately 1,100 kilometers across Europe, formed in the foreland of the Alps as the lithosphere responded to the immense forces generated by the Alpine and Pyrenean orogenies (Dèzes et al., 2004).

The ENE-WSW trending axis of the Eger rift roughly aligns with a major crustal inhomogeneity, which is interpreted as a significant Variscan suture zone separating the Saxothuringian, Tepla-Barrandian, and Moldanubian terranes. This pre-existing zone of weakness within the lithosphere is believed to have been reactivated during the Cretaceous and Tertiary periods, playing a crucial role in the rift's development (Cajz & Valečka, 2010). The geological structure of the Eger Rift is characterized by a system of faults and associated sedimentary basins and volcanic fields. The main graben is defined by two primary fault systems: the ENE-striking Erzgebirge Fault, which forms the northwestern shoulder of the rift and has accommodated the tilting and uplift of the Erzgebirge block, and the Czech Low Mountains Fault, which separates the main basin from the adjacent low mountain ranges (Cajz & Valečka, 2010). The Eger Graben itself contains a relatively thin Cenozoic volcano-sedimentary infill, with a maximum thickness of around 500 meters. Within the rift zone, several NE-trending sedimentary basins, such as the Cheb Basin, the Sokolov Depression (approximately 40 km long and 10 km wide), and the Most Basin (80 km long and up to 30 km wide), have developed, filled with Paleogene to Neogene sediments (Andreani et al., 2014).

Volcanic activity within the Eger Rift and the broader Bohemian Massif has been episodic, spanning distinct geological epochs from the Late Cretaceous to the Late Pleistocene, reflecting the complex neotectonic rejuvenation of the Bohemian Massif. The earliest identified phase, often termed the prerift period, occurred between approximately 79 and 49 million years ago (Ma), during the Late Cretaceous to Paleocene. This initial stage of rifting is characterized by rare occurrences of ultramafic melilitic rocks, such as those found in the Osečná Complex and the associated Devil's Dyke swarm, typically located in the outer parts of the rift zone (Ulrych et al., 2008). These primitive melilitic rocks, with their low SiO2 and high CaO, MgO, and CO2 contents, are thought to derive from the partial melting of a heterogeneous, CO2-rich, veined mantle at high

pressures (27-40 kbar), suggesting an early interaction with carbonate-rich fluids during incipient rifting.11 This early, deep-sourced, CO2-rich ultramafic volcanism suggests incipient lithospheric weakening (Ulrych et al., 2008).

Following this, the main synrift period unfolded from approximately 42 to 16 Ma, encompassing the Eocene to Miocene. This phase experienced a voluminous bimodal suite of basanites and phonolites, predominantly found in the inner part of the Ohře Rift zone. Simultaneously, in the western and northwestern part of the Bohemian Massif, volcanic activity, including the formation of the Doupovské hory Volcanic Complex, occurred between 35 and 17 Ma, specifically during the end of the Oligocene and into the early Miocene. The Doupov Intrusive Complex, for instance, shows K-Ar ages of approximately 30-29 Ma for its phaneritic intrusive rocks, which are notably older than the overlying tephrite-basanite and foidite lavas, indicating a complex intrusive-extrusive relationship within the magmatic system (Holub et al., 2010). Another example from this period is the Říp Hill, an Oligocene volcanic structure near the Eger Rift, which is interpreted to have formed from a nephelinite lava lake fed by segmented dikes, with its eroded crater speculated to be of a phreatomagmatic maar-type (Tomek et al., 2025). The voluminous bimodal suite in this synrift stage indicates more mature rifting with greater melt production and differentiation, signifying a co-evolution of the magmatic system and the rift itself.

The most recent phase, referred to as the late-rift period, spans from approximately 16 to 0.3 Ma, covering the late Miocene to the Pleistocene. This period includes a significant stage of volcanic activity in the late Miocene (between 9.0 and 6.4 Ma) and a later phase from the late Pliocene to the Pleistocene (between 3.0 and 0.17 Ma). The western Eger Rift, particularly the Cheb Basin, exhibits Miocene-to-Pleistocene basaltic volcanoes, including cinder cones and maars. This area accommodates several significant volcanic structures, including the well-known Komorní Hůrka and Železná hůrka, as well as the larger Doupov Mountains Volcanic Complex. Komorní Hůrka, a small, inconspicuous scoria cone, holds historical significance in Earth science, as its basaltic feeder dike, exposed through adits, provided crucial evidence in the 19th-century debate between Plutonists and Neptunists, definitively proving the magmatic origin of such rocks (Rapprich et al., 2019). Geophysical investigations have further elucidated its internal structure, revealing the precise position of its feeder dike and the geometry of its lava flow, offering rare direct evidence of a magma plumbing system (Hrubcová et al., 2017).

Železná hůrka, located near Mýtina in the Cheb District, is an extinct Quaternary volcano, with its oldest parts dated to approximately 519,000 years ago, and later tephra deposits to 300,000 years (Brandl et al., 2015). This volcano is notable for its pyroclastic cone, formed by discontinuous eruptions, and for exhibiting a transition in eruption styles from early phreatomagmatic activity, which deposited brownish, layered material containing low-porosity hydroclasts, to later purely magmatic activity, which produced black to dark-brown, slightly welded material with porous lava fragments, volcanic bombs, and lapilli. A unique geochemical feature of Železná hůrka is the presence of metallic iron fragments within its basalt deposits, believed to have formed naturally through the interaction of iron-rich magma with coal deposits, akin to a natural smelting process. (Brandl et al., 2015).

1.3.3 Selected fault zones of the Western Bohemian Massif related to volcanic and seismic activity

The western part of the Bohemian Massif is traversed by several significant fault zones that play a crucial role in its tectonic framework. These include the Tepla Fault Zone, the Marianske Lazne Fault Zone, and the Tachov Fault Zone.

The Tepla Fault Zone acts as a major geological boundary, separating the Teplá-Barrandian and Moldanubian complexes within the Bohemian Massif (Babuška et al., 2007), trending in a general NNW-SSE direction. To the east of this fault zone, the Teplá-Barrandian Unit transitions into lower-grade Proterozoic rocks, to the east, occurrences of small, metamorphosed, and deformed Cadomian plutonic bodies have been documented (Havíř et al., 2005).

The Tachov fault zone (TAZ) is another significant tectonic feature in the western Bohemian Massif, elongated in a NNW-SSE direction. TAZ isrecognized as a major NNW-SSE trending shear zone, extending for at least 100 kilometers along the boundary between the Moldanubian unit to the west and the Teplá-Barrandian unit to the east (Babuška et al., 2007).

The Mariánské Lázně Fault (MLF) stands out as a morphologically, geologically, and tectonically prominent structure in the western Bohemian Massif. It extends for approximately 100 kilometers with a general NNW-SSE orientation (Babuška et al., 2007). This fault zone plays a significant role in defining the eastern boundary of the Cenozoic Cheb Basin and acts as a major tectonic boundary between several principal geological units of the Bohemian Massif: the Saxo-Thuringian unit to the northwest, the Moldanubian unit to the south and southwest, and the Teplá-Barrandian unit to the east. The MLF is notably associated with present-day earthquake swarms (Fischer et al., 2014), emanations of mantle-derived carbon dioxide, and has been the subject of extensive geophysical and paleoseismological investigations (Blecha et al., 2018; Štěpančíková et al., 2019). In the vicinity of Nový Kostel, the fault splays into two distinct scarps (Fischer et al., 2012; Štěpančíková et al., 2019). Further south, the MLF forms the eastern limit of the Cheb-Domažlice Graben. Paleoseismic trenching studies conducted near Kopanina village (Štěpančíková et al., 2019) have revealed evidence of repeated movements along multiple fault strands within the MLF. These movements have displaced sedimentary deposits dating back to the Oligocene epoch, with the most recent event estimated to have occurred between 792 and 1020 CE. Geophysical data indicates that the MLF is characterized by a zone up to 100 meters in width, exhibiting low electrical resistivity, low density and low seismic velocity, suggesting the presence of intensely fractured and weathered rocks along the fault zone (Blecha et al., 2018; Fischer et al., 2012; Štěpančíková et al., 2019).

1.3.4 Maar diatreme volcanoes in West Bohemia

Mýtina & Neualbenreuth maars

The Mýtina Maar (Flechsig et al., 2015; Lied et al., 2020; Mrlina et al., 2007, 2009) (Figure 1.2), discovered in 2007 in West Bohemia, approximately 1 kilometer north of the Železná hůrka volcano and 10 kilometers southeast of Cheb, is notable as the first Quaternary maar identified in Central Europe north of the Alps and east of the Volcanic Eifel. This location places it within the western part of the

Cheb Basin, an area known for Quaternary volcanic activity. Both the Mýtina maar and the nearby Neualbenreuth maar (Rohrmüller et al., 2018) are reported to penetrate phyllites belonging to the Dyleň massif, indicating a common geological substrate for these two volcanic structures. The spatial association of the Mýtina maar with the Železná hůrka scoria cone suggests a potential link between different styles of volcanism within this localized area.

It is a dry maar, meaning it does not currently contain a lake, and it lacks prominent morphological features that would readily identify it as a volcano. Despite this, extensive geophysical surveys, including gravimetry, magnetometry, and electrical resistivity tomography, along with borehole drilling, have provided insights into its subsurface structure (Mrlina et al., 2009). Gravity modeling of the area suggests a layered structure, with a near-surface cover of sediments, underlain by low-density volcanic material at shallow depths, and a zone of higher density volcanic breccia at greater depths within the maar diatreme. Electrical resistivity tomography data show a layer of lower resistivity in the upper 100 meters, which is consistent with the presence of sedimentary infill as indicated by borehole drilling (Mrlina et al., 2009).

The Neualbenreuth Maar (Rohrmüller et al., 2018) (Figure 1.2) is located approximately 2.5 kilometers east-southeast of Neualbenreuth in northeastern Bavaria, Germany. Its position aligns with the northwest-southeast trending Tachov fault zone, suggesting that this fault system played a role in facilitating magma ascent to this location. Similar to the Mýtina maar, the Neualbenreuth maar also penetrates phyllites of the Dyleň massif, indicating a shared geological context. The alignment of this maar with other volcanic features along the Tachov fault zone underscores the importance of fault zones as conduits for magmatic activity within the Bohemian Massif region. Both maar eruptions were dated between 0.29 and 0.27 Ma within the Mid-Pleistocene.

It was discovered through geophysical prospecting and further investigated by drilling (Rohrmüller et al., 2018), which revealed a sequence of lake sediments reaching a depth of 100 meters. This accumulation of lacustrine sediments suggests that a maar lake was present at this location for a considerable period, offering a potential archive for paleo-environmental studies.

Bažina & Ztracený rybník maars

The Bažina and Ztracený rybník (Hrubcová et al., 2023) (Figure 1.2) maars are also situated in western Bohemia within the western Eger Rift, in proximity to the Cheb Basin (see Figure1.1). Both maar eruptions were estimated to occur more than 0.78 Ma ago.

The Bažina maar has been studied through geophysical surveys and borehole drilling, which revealed the presence of coherent volcanic rocks and volcaniclastic deposits within the maar structure. Notably, a pyroclastic cone with an olivine nephelinite feeding conduit has been identified within the maar crater, indicating subsequent volcanic activity after the initial maar-forming eruption. Furthermore, a distinctive vein of apatite-dominated rock has been found to penetrate the volcaniclastic fill of the maar, suggesting either unusual magmatic processes or post-eruptive hydrothermal alteration within the volcanic system.

The Ztracený rybník maar was investigated using LiDAR-derived digital elevation models, revealing well-preserved crater morphologies with sharp edges, a

characteristic attributed to the hard granitic rock in which they formed. Electrical resistivity tomography suggests the presence of a significant thickness, approximately 100 meters, of fine-grained sedimentary infill within the crater structures, overlying material with higher resistivity, potentially coarser-grained sediments or granitic bedrock. Analysis of the uppermost part of this infill has identified Holocene peat and underlying lacustrine sediments, indicating the past presence of maar lakes within the crater.

Sepuska & Nežichov

The Sepuska and Nežichov maar lie close to the city of Teplá in West Bohemia, in its eastern part. Tectonically, they belong to the Teplá fault zone, where series of phreato-magmatic eruptions occurred around 12.1 Ma ago. The chemistry of magma was determined as felsic, specifically as trachyandesite (Ulrych et al., 2003). Both maars create a visible depression in the topography, Nežichov maar is also delineated by the Třebouňský and Branišovský hill in the western part. The larger depression, the Nežichov maar spans across about 1.5 km in diameter while smaller Sepuska appears to be about half the size. Both depressions are currently used as pastures and meadows with an artificial lake in their centers. These newly discovered maars are described in Chapter 4.

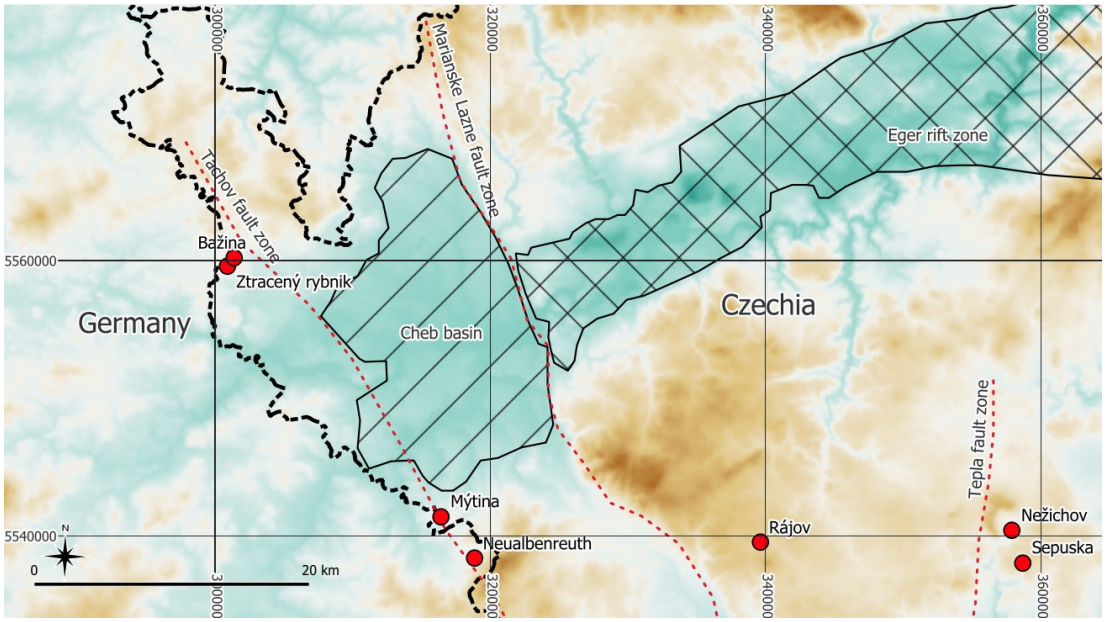


Figure 1.2 Map of the discovered and currently studied maar volcanoes (red circles) in West Bohemia region. Black dashed line is the country border between Czechia and Germany. Red dashed lines representing the described fault zones, the Cheb basin (left slated polygon) and the Eger rift zone (cross slated polygon) are based on Hrubcová et al. (2017). Map coordinates are in the WGS 84 / UTM zone 33N system. Mýtina maar is described in the chapter 2 and 3, Nežichov and Sepuska in Chapter 4. Ztracený rybník and Bažina are discussed in Chapter 5. At Rájov our observed results were inconclusive, however Rájov was identifed as a maar volcano by Valenta et al. (2014).

1.4 Analysis methods for ambient vibrations in maar crater infills

Maar craters pose unique challenges and opportunities for geophysical investigation. These structures often contain water or sediments and hide complex subsurface architectures, including diatremes, which are pipe-like conduits filled with fragmented volcanic and country rock. Understanding their morphology, eruption history, and magmatic processes usually requires a multidisciplinary approach that combines geophysical techniques with drilling and morphological analysis (e.g., Hrubcová et al. 2023; Kašing et al. 2025; Mrlina et al. 2007; Rohrmüller et al. 2018; Skácelová et al. 2010; Tomek et al. 2025; Valenta et al. 2014).

Various geophysical methods are crucial for surveying maar craters' infills. Gravity surveys help identify density contrasts between maar deposits and surrounding bedrock, while magnetic surveys exploit variations in magnetic susceptibility to delineate volcanic materials within maar structures. Electrical resistivity tomography (ERT) and transient electromagnetic (TEM) methods map subsurface resistivity contrasts, differentiating between conductive lake sediments and resistive volcanic breccias or country rocks. Seismic methods provide high-resolution images of maar sediments and diatreme boundaries, and LiDAR generates high-resolution digital elevation models to identify subtle maar morphologies.

The integration of these geophysical techniques, along with calibration through borehole data, enhances the understanding of maar volcanoes. Drilling into identified anomalies allows for the interception of pyroclastic deposits and other geological features, revealing eruptive sequences and aiding in the reconstruction of volcanic phases. Nevertheless, drilling is expensive and the unfavorable craters' aspect ratios (depth $>$ lateral dimensions) limit the depth resolution of the standard geophysical methods.

Our aim was to investigate possible 3D site effects at selected maars in West Bohemia and try to use them for craters' characterization. We have utilized previously developed methods for assessment of local site effects and applied them onto the recordings and numerical simulations of the ambient vibration of craters infills. The use of ambient seismic noise is a convenient approach to assess local site effects, since it does not rely on earthquakes, which might not be present in low seismicity areas. Origin of the seismic noise comes both from human and natural activity (Bonnefoy-Claudet et al., 2006). Naturally occurring seismic noise named in general microseisms consists of ocean-induced microseisms at 0.3 Hz and other meteorological exhibitors, usually occurring locally like wind generating noise around 1 Hz. Above 1 Hz, the sources of the seismic noise named microtremors are prevalently man-made, like traffic, industry etc. The temporal variations of microseisms are linked to oceanic activity, while microtremors show daily and weekly variations based on human activity. Both microseisms and microtremors propagate dominantly as surface waves – Love and Rayleigh waves (Bonnefoy-Claudet et al., 2006).

Various methods for the processing of ambient vibrations data are presented in the following subsections.

1.4.1 Site-to-Reference Spectral Ratio (SRSR)

The Site-to-Reference Spectral Ratio (SRSR) method is used to evaluate the seismic response of a specific site by comparing the spectral characteristics of seismic waves recorded at that site with those from a nearby reference site, typically located on stable ground. This method helps in assessing site effects, which are crucial for earthquake engineering and designing structures to withstand seismic events. SRSR was originally developed to analyze recordings of earthquakes (Borcherdt, 1970), but it was later implemented to process ambient seismic noise recordings as well (Irikura & Kawanaka, 1980; Kleinbrod et al., 2017; Pischiutta et al., 2017). The advantage of this method lies in its simplest principle that only two (preferably 3-component) seismic stations recording simultaneously are required (though more stations are preferred), one placed at the studied structure and the other one, the reference one, in proximity to the structure and preferably on the outcropping bedrock. This reference point should ideally present minimal site effects. It should be as close as possible to the site of interest to ensure similar seismic wave propagation conditions. The ratio between inter-station distance and the distance to the sources of the ambient vibrations must be as low as possible. The ratio between the inter-station distance and the distance to the sources of ambient vibrations should be as small as possible. This ensures that the sources can be considered far-field, allowing the assumption that source and path effects are nearly identical at both the reference station and the stations within the structure. Under this condition, the normalization procedure described in Equation 1.1 yields a spectral ratio that effectively isolates the local site response by dividing the spectrum recorded at the structure by that at the reference bedrock site:

$$\begin{aligned} SRSR_j(f) = \frac{|u_j(f)|}{|u_{ref}(f)|} &= \frac{|S\left(f, \mathbf{x}_j, \mathbf{x}_o\right) P\left(f, \mathbf{x}_j, \mathbf{x}_o\right) A\left(f, \mathbf{x}_j\right)|}{|S\left(f, \mathbf{x}_{ref}, \mathbf{x}_o\right) P\left(f, \mathbf{x}_{ref}, \mathbf{x}_o\right) A\left(f, \mathbf{x}_{ref}\right)|} \\ &\approx \frac{|A\left(f, \mathbf{x}_j\right)|}{|A\left(f, \mathbf{x}_{ref}\right)|} \approx |A\left(f, \mathbf{x}_j\right)| \end{aligned} \tag{1.1}$$

where $SRSR_j(f)$ is the Site-to-Reference spectral ratio at the j-th station, $|u_j(f)|$ is the displacement spectrum at the j-th station, which is comprised of $S\left(f, \mathbf{x}_j, \mathbf{x}_o\right)$, that is the source effect for the position $\mathbf{x}_j$ of j-th station and $\mathbf{x}_o$ position of the source, $P\left(f, \mathbf{x}_j, \mathbf{x}_o\right)$ path effects between the station and the source and the $A\left(f, \mathbf{x}_j\right)$ local amplification at the j-th station. The $u_{ref}(f)$ is the displacement spectrum for the reference station, the $S\left(f, \mathbf{x}_{ref}, \mathbf{x}_o\right) P\left(f, \mathbf{x}_{ref}, \mathbf{x}_o\right) A\left(f, \mathbf{x}_{ref}\right)$ are the source, path and local amplification for the reference station in relation to the source. When the reference site is appropriately selected, its amplification term $A\left(f, \mathbf{x}_{ref}\right)$ can be assumed to be equal to one. In this case, $SRSR_j(f)$ becomes directly proportional to the local amplification at the j-th station.

The SRSR method is the primary approach used for site effect characterization in this thesis. In the case of maars, selecting a reference site is straightforward, as the craters are formed directly in bedrock, making outcropping bedrock readily accessible nearby.

1.4.2 Horizontal-to-Vertical Spectral Ratio (HVSR)

The Horizontal-to-Vertical Spectral Ratio is a widely used method to characterize the local site effects. This method utilizes only one 3-component seismic station at a time and does not require the reference station to be recording as well. It is calculated as a ratio of the Fourier amplitude spectra between each horizontal component (North-South and East-West) and the vertical component of the ambient seismic noise (Nakamura & Samizo, 1989). A number of different interpretations of HVSR curves exist based on different assumptions, especially related to the noise wavefield composition. In general, the first prominent peak in HVSR indicates the fundamental resonance frequency (f_0) of the site. This can usually be interpreted as the resonance of the surface layer over the stiffer bedrock. This principle works in general well in case of a laterally homogeneous 1-D layered subsurface. In case of more complex geometry and geology, the interpretation might not be straightforward, which is exactly the case of maar craters. HVSR is a widely used method, even when its underlying assumptions are not fully met or explicitly considered during interpretation. In this thesis, the method is applied to demonstrate the influence of 3D subsurface geometry on HVSR curves and to highlight potential pitfalls for users who may apply it at maar sites without accounting for its limitations.

1.4.3 Frequency Domain Decomposition (FDD)

Frequency Domain Decomposition (FDD) is a modal analysis technique used to extract the dynamic properties of structures or subsurface profiles from ambient vibration data. It is particularly suited for structures where resonance, or standing wave patterns, develop under dynamic loading. That is for structures whose response can be described by the sum of modes - independent single-degree-of-freedom systems (SDOF), e.g. (Brincker & Ventura, 2015). The method decomposes the power spectral density matrix of the recorded signals using eigen value decomposition, enabling the identification of natural frequencies, mode shapes, and damping ratios of the different modes (SDOF) without requiring information about the input excitation. Although it was initially implemented for engineering structures by Brincker et al. (2001), it was later successfully applied to characterize seismic response of rock columns, landslides, sedimentary valleys and glaciers (Bottelin et al., 2013; Häusler et al., 2019; Poggi et al., 2014; Preiswerk et al., 2019). It computes the cross-power spectral density matrix of all components of the noise recordings for every discrete frequency through the whole investigated frequency band and then carries out an eigen value value decomposition for all those matrices. The first singular eigenvalues represent roughly the sum of the auto-spectral densities of the dominant normal modes. Its peaks correspond to the different modes (SDOF) of the structure. The related eigenvectors describe the 3-dimensional shapes of these resonant modes, including their relative phases. The method is sensitive to outliers. Therefore, time windows containing transient signals, as well as erroneous recordings, must be excluded from the analysis to prevent biasing the results and distorting the identified modal properties. The number of sensors or components used in FDD is not limited - it can be applied to data from a single sensor or an array of sensors. However, the extraction of detailed mode shapes and higher modes requires recordings from a spatially

distributed array, as single-sensor measurements do not provide sufficient spatial information for resolving complex modal behavior (Brincker & Ventura, 2015). In this thesis, the method was found to be well suited for characterizing the dynamic response of maars, providing valuable insight into their resonant behavior and modal properties.

1.4.4 Time Frequency Polarization Analysis (TFPA)

Time-Frequency Polarization Analysis (TFPA) characterizes the particle motion of ambient vibrations by analyzing polarization attributes as a function of frequency. Since ambient vibrations are assumed to be stationary over time, only statistical analysis is performed over the time domain, while the frequency-dependent behavior of the wavefield is the primary focus. The directionality of the resonances in the structure can be evaluated by this method (if present). The method is based on the approach of Vidale (1986) complex polarization analysis combined with the continuous wavelet transformation as implemented by (Burjánek et al., 2010, 2012). The algorithm uses a sliding time window, for which it describes the frequency-dependent particle motion by a tilted ellipse, defined by strike, dip, and ellipticity. Strike represents the azimuth of the major semi-axis, dip its tilt, and ellipticity the ratio between the minor and major semi-axes of the ellipse. All these parameters are time and frequency-dependent, so for averaging we require a long-recorded time sequence (usually a few hours), during which we assume the quasi-stationarity of the seismic sources, i.e., the sources of the ambient seismic noise keep their properties (position, frequency content) during the whole recording. The method, as implemented, is conceptually very similar to FDD described above. In principle, it corresponds to FDD applied to a single three-component station recording. The polarization attributes are derived from the eigenvalue decomposition of the three-component covariance matrix in the case of TFPA. However, unlike FDD, the method is less sensitive to outliers, as it focuses solely on polarization attributes (strike, dip, ellipticity), rather than averaging the full particle motion, including phase relationships between components. In this thesis, the method is applied as a supplementary approach to FDD and, additionally, to demonstrate its feasibility for analyzing single-station recordings.

1.4.5 Frequency-wavenumber (F-K) analysis and the shear velocity inversion from a dispersion curve

The frequency-wavenumber (f-k) array method is used to estimate phase velocities of presumably planar seismic waves within an ambient noise wavefield by analyzing multiple simultaneous recordings from an array of sensors distributed on the Earth's surface. While theoretically, two stations with known positions and wave azimuths suffice to determine wave velocity, real ambient noise consists of multiple waves arriving from unknown directions and frequencies, complicating the estimation. Therefore a 2D array of seismic sensors is required in practice. Since the noise wavefield is predominantly composed of surface waves (Love and Rayleigh; Bonnefoy-Claudet et al. 2006), the phase velocities estimated from the 2D surficial arrays primarily correspond to the phase velocities of seismic surface waves.

We applied the f-k spectral method, specifically a high-resolution three-component variant implemented in the open-source Geopsy software (Wathelet et al., 2020). The recorded time-domain signals are divided into windows, and f-k spectra are computed and averaged. Peaks in these spectra correspond to incoming waves characterized by specific azimuths and phase velocities. The array geometry defines the resolvable wavenumber range: the largest interstation distance sets the minimum wavenumber, while the smallest distance sets the maximum. Assuming the wavefield is dominated by surface waves, phase velocities of Rayleigh waves are estimated from vertical and radial components, while Love wave velocities are derived from the transverse component relative to wave propagation.

Surface wave phase velocities vary with frequency due to subsurface layering, and this frequency dependence is described by dispersion curves. While Love wave particle motion is linear and horizontal, Rayleigh wave particle motion is elliptical and generally frequency-dependent. It is characterized by frequency-dependent ellipticity, defined as the ratio of horizontal to vertical displacement components. The Rayleigh wave ellipticity peak can be estimated from f-k analysis (Poggi & Fäh, 2010) or from the HVSR curve, assuming it is dominated by fundamental-mode Rayleigh waves (e.g.,Bard et al. 1999; Lachetl and Bard 1994). Both dispersion and ellipticity curves can be used to constrain subsurface elastic parameters, assuming a one-dimensional layered elastic medium—particularly shear wave velocity profiles. This inverse problem is addressed in this thesis using the Dinver module in Geopsy. The subsurface model is parameterized by the number of layers and specified parameter ranges (e.g., layer thicknesses and seismic velocities). The inversion begins by randomly generating a large number of models within these bounds and computing synthetic dispersion and ellipticity curves for each (e.g., Wathelet et al. 2008). The forward problem—calculating dispersion and ellipticity for a given model—is highly nonlinear. Synthetic curves are then compared to observed data to calculate misfits. Models with lower misfits are retained for further exploration, thereby focusing the search on promising regions of the parameter space. Optimization proceeds using the neighborhood algorithm, which partitions the parameter space into cells and iteratively refines them to identify regions yielding minimal misfits. The process continues until a predefined number of models have been evaluated, resulting in a set of elastic parameter models consistent with the observed surface waves properties (dispersion curves, Rayleigh wave ellipticities). A detailed description of the overall methodology for site characterization using f-k analysis and ambient noise array measurements is beyond the scope of this thesis; comprehensive overviews can be found in (Okada, 2006; Tokimatsu et al., 1992; Wathelet et al., 2004). In this thesis, the methodology was used to infer the shear-wave velocity structure of the maar crater infills, which served as input for developing the 3D velocity model used in the numerical simulations.

1.5 Numerical modeling of maars' ambient vibrations

To support the interpretation of the observations, a 3D velocity model of the maar crater infill was developed, and ambient noise wavefields within the

infills were simulated. We followed the approach described in Burjánek et al. (2019). Numerical simulation of ambient noise is carried out in two steps: first, the medium's Green's functions are computed; then, synthetic noise records are formed by superposing the responses to multiple random source excitations. In practice, we compute Green's tensors with a 3-D finite-difference solver (here the 4th-order code SW4), using reciprocity (swapping source and receiver) to reduce the number of simulations (Eisner & Clayton, 2001). In the second step, ambient-noise time series are generated by summing the responses from a large ensemble of point-force sources that are randomly distributed in space, each convolved with a stochastic (randomized) source-time function. This strategy treats cultural noise as uncorrelated body-force perturbations (with random locations, orientations and timing) – an approach originally introduced by Moczo et al. (2002) and later implemented by Burjánek et al. (2019) for unstable rock-slope environments. We apply this methodology to maar volcanoes: computing Green's functions in a 3-D velocity model with SW4, then building long synthetic noise records by superposition of random source responses. The resulting synthetic noise can then be analyzed using all the methods previously introduced for ambient vibration processing, in direct analogy to the processing of observational data. The simulated ambient vibrations can be compared with the observed ones in terms of resonance frequencies, amplification levels, and spatial patterns by applying the same methods (SRSR, HVSR, and FDD).

1.5.1 SW4 settings and properties

SW4 (Seismic Waves, 4th order) is a specialized simulation tool for seismic wave propagation, optimized for parallel computing. It uses a node-based finite difference approach with fourth-order accuracy in both space and time, which allows for more efficient and stable long-term simulations compared to lower-order methods. This design choice enables coarser grids and reduces phase error accumulation. The software supports complex 3D modeling, including realistic topography, free surface conditions, advanced absorbing boundaries, and flexible source definitions. A detailed description of the numerical method is beyond the scope of this thesis; further details can be found in the SW4 manual (e.g., N. A. Petersson and Sjögreen 2015). Below, we provide only a brief summary of the main practical steps involved in the preparation and execution of the simulations.

Establishing the Simulation Environment: Initial Configuration

Setting up an SW4 simulation involves defining the computational domain, simulation duration, boundary conditions, and optional pre-filtering of source functions. Users have significant control over these parameters, but SW4 automates many aspects to ensure optimal stability and performance, balancing user flexibility with robust defaults. Details of the specific simulation setup used in this study are provided in later chapters.

Defining the Computational Domain

Users can specify the simulation domain in SW4 by setting grid points and spacing, physical dimensions, or a combination, with built-in checks to prevent

over-specification. The number of grid points per wavelength is a critical parameter that directly affects the accuracy and stability of seismic wave simulations. To accurately resolve wave propagation, especially at high frequencies, the numerical method requires a sufficient number of grid points per shortest wavelength present in the simulation. It is recommended to use at least between 6–12 points per wavelength to adequately capture the wavefield without introducing significant numerical dispersion or attenuation. We used at least 6 points per wavelength in our simulations.

Configuring Super-Grid Damping Layers

SW4 uses super-grid damping layers to absorb outgoing waves and minimize artificial reflections at domain boundaries. Users can control the thickness and damping coefficient of these layers, but must avoid placing sources or receivers within them, as the solution there is artificial. While thicker layers improve absorption, they increase computational cost, and improper settings can cause instabilities, requiring users to balance accuracy, efficiency, and stability. We used the default 300 m buffer zone in our simulations.

Implementing Mesh Refinement

Users can define multiple refinement levels and specify their spatial extents, resolutions, and transition criteria. SW4 automates the management of grid interfaces, ensuring proper communication and stability between different refinement levels. The software also handles the interpolation and synchronization of wavefields across these interfaces, minimizing numerical artifacts. This mesh refinement capability enables high-resolution modeling where needed (such as near sources or receivers) without incurring the computational cost of a uniformly fine grid across the entire domain. We used mesh refinements at 40 and 100 m of depth in our simulations to keep the requirement of 6 grid points per wavelength.

Controlling Simulation Duration

The simulation's time span is set using either a total duration or a specific number of time steps. SW4 automatically calculates the time step (δt) based on the Courant-Friedrichs-Lewy (CFL) stability condition, using the grid size and maximum wave speed, which ensures stability and removes the need for manual, potentially error-prone, time step selection.

Material Model Specification and Attenuation Mechanisms

SW4 allows users to define the subsurface material properties using a variety of commands that support isotropic elastic, isotropic viscoelastic, and anisotropic elastic models. The software requires all interior and boundary grid points to have specified material properties. Before running a simulation, SW4 checks that material parameters are physically valid, such as ensuring positive density and wave speeds. This automation helps prevent common user errors and ensures that the simulation operates on a realistic and stable physical model.

For simulations that require modeling energy loss (attenuation), SW4 provides support for isotropic viscoelastic materials. Users can specify attenuation parameters such as Qp (for P-waves) and Qs (for S-waves), which represent the quality factors controlling energy dissipation. The software applies these parameters according to the chosen viscoelastic model, allowing for more realistic simulation of seismic wave propagation in media where attenuation is significant. This capability is important for accurately modeling real-world seismic responses, especially in sedimentary basins or other lossy environments.

Creating a material model file, in our case the r-file option for numerical modeling in SW4 presents several challenges, particularly in ensuring the accurate representation of complex geological and geophysical material properties. The file must define spatially varying parameters like density, seismic velocities (P-wave and S-wave), and attenuation coefficients with high precision and in formats strictly compatible with SW4's input requirements. This demands careful preprocessing of observational or synthetic data, often involving interpolation onto a Cartesian grid, unit consistency, and validation of physical plausibility. Moreover, errors in formatting or data alignment can lead to simulation failures or misleading results, making thorough verification essential. For large-scale models, managing file size and computational performance also becomes critical, especially when handling high-resolution data over extensive domains. The material model was prepared in Matlab.

Characterizing Seismic Sources

Users can specify an arbitrary number of sources, each with parameters such as location, source type (point force or moment tensor), orientation, amplitude, and source time function. The software supports a variety of source time functions, including analytic shapes (e.g., Ricker, Gaussian, Dirac) and user-supplied time histories. SW4 automatically handles the insertion of sources into the computational grid, accounting for grid spacing and ensuring correct alignment with the mesh. The software also checks for potential issues, such as sources placed within absorbing boundary layers, and provides warnings to the user. We used the Ricker wavelet due to its convenient properties: it has an analytic expression in both the time and frequency domains, a well-defined frequency band with monotonically decaying spectra (eliminating the need for pre-filtering; see below), and a limited, well-defined duration in the time domain.

Pre-filtering Source Time Functions

The prefilter command allows users to apply frequency filters to all source time functions before running the simulation, reducing the need for post-processing and mitigating numerical artifacts from high-frequency content. Users can specify filter type, corner frequencies, order, and phase characteristics. This is particularly important for sources like the Dirac function, which can excite unresolved frequencies and cause unphysical results. SW4 also warns users if filter settings might cause abrupt or unrealistic source onsets. However, this was not necessary in the case of the Ricker wavelet with a properly selected central frequency.

1.5.2 Synthetic ambient noise generation

In our calculations, Green's function computation is required for many seismic noise sources and a small number of recording stations, yielding great asymmetry in the computation. Therefore, we employ the reciprocity method to help us decrease the number of calculations required to compute the seismic wave propagation from every source (utilized by e.g. Eisner and Clayton 2001), which states the elastodynamic Green's tensor for the source – station can be computed by switching the position of the source for position of the station and switching the station for the source. This is based on the reciprocity theorem for anelastic continuous body (Dahlen & Tromp, 1999).

To generate an arbitrarily long time series of ambient seismic noise, the Green's functions are transformed into spectral domain, normalized with the spectrum of a corresponding Ricker pulse, and are summated to randomly distributed point force sources with randomized source time functions (e.g. Moczo et al. 2002). We utilize the approach of Burjánek et al. (2019), which employs uniform probability distribution of point sources, origin times of the sources, point-force directions and characteristics of source time functions. It randomly samples four different source time functions: Dirac delta function, Morlet wavelet, modified Brune's pulse and Ricker's pulse.

1.5.3 Example of numerical modeling of Mýtina maar

We include this section to provide an example of the numerical modeling performed for the Mýtina maar, as the details of the simulations were beyond the scope of the published papers (Chapters 2 and 3). Here, we present key parameters from a representative simulation to give a general overview of the computational setup. The simulation domain measured 4 × 4 × 2 km with a base grid spacing of 10 m and refinements at 100 m (5 m spacing) and 40 m (2.5 m spacing) depths to ensure sufficient resolution for low-velocity near-surface layers. One hour of seismic noise was simulated by summing responses from randomly distributed point-force sources in three orthogonal directions represented by Ricker pulses with a central frequency of 4 Hz, convolved with randomized source time functions, and utilizing Green's functions computed for the duration of 20 seconds via the reciprocity method. Two virtual source grids (92 × 92), located at 0 m and 1 km depth, were used with 30 m spacing and a 600 m offset from grid boundaries. Material properties were defined for three main units—lacustrine sediments, inner breccia, and outer breccia—based on surface wave array measurements. S-wave velocities increased with depth from 166 m/s (sediments) to 1153 m/s (outer breccia), with deeper breccia assumed to have Vs = 1500 m/s. The P-wave velocity was defined using a uniform Vp/Vs ratio of 3, and density was set at 2.2 g/cm^3. Attenuation was introduced using empirical relations, with Qs = 7.17 + 0.0276×Vs and Qp = 2×Qs. The origin of all these specific values is discussed in detail in Chapter 2. The most representative model featured an elliptical conical breccia body (160–200 m minor and major half-axis, 800 m deep), and a 100 m in radius, 100 m thick sediment layer. The details on the development of the velocity models can be found later in Chapter 2. We run the calculations on the Karolina supercomputer belonging to the IT4I project in Ostrava, Czechia. To compute one full visco-elastic Green's tensor (9 Green's functions, i.e. for 3

orthogonal source forces received on 3 orthogonal recordings) for one station we required around 6 node hours, where one node has 128 CPU cores, resulting in about 768 core hours. For Mýtina maar, we computed Green's functions for six stations—including the reference station—using the final elastic and visco-elastic model. During the testing of different velocity models, Green's functions were calculated for only one station at the maar's center, resulting in approximately 20 station-specific simulations in total. Since each station required 768 core hours, the total computational cost amounted to roughly 15,360 core hours. The overall computational budget was even higher, as additional resources were used for testing different model setups, parameter tuning, and verification runs.

1.6 Content of this thesis

In general, we start by analyzing local site effects at the well-documented Mýtina maar volcano in West Bohemia, using it as a reference point to validate our research methods, as detailed in Chapter 2 and 3. Our approach involves the use of ambient seismic noise and numerical modeling to estimate the structural parameters of these volcanic formations. This methodology is thoroughly described in chapter one, emphasizing its importance in understanding the subsurface characteristics of maar volcanoes. In Chapter 4, we extend our study to newly discovered maar volcanoes at Nežichov and Sepuska (Figure 1.2), applying our validated techniques to uncover their geological features. We utilize ambient seismic noise surveys, gravimetric measurements and electric resistivity tomography. In Chapter 5 we summarize our findings from Mýtina maar, conclude the Nežichov and Sepuska maars and present preliminary results from Ztracený rybník, Bažina and Neualbenreuth maars, where a layer of peat soil increases spread of observed amplification in the maar infill.

2 Modelling the seismic response of the Mýtina maar volcanic structure

This chapter was published as Labuta et al. (2023) in Earth, Planets and Space.

2.1 Introduction

Maar is a broad, low-relief volcanic crater, caused by a phreatomagmatic eruption. It is filled with volcanic eruption breccia, lava and sediments, and often housing a shallow lake on top (so-called maar lake). A dry maar results when the maar lake dries out, for example, due to the deposition of sediments. The Mýtina dry maar belongs to a series of recently discovered Quaternary volcanic structures in Czechia (Mrlina et al., 2009). It is situated in West Bohemia, 1 km north of the Železná hůrka Quaternary volcano, and 10 km SE from the city of Cheb, Czechia. It is the first Quaternary maar discovered in Central Europe north of the Alps and east of Volcanic Eifel (Mrlina et al., 2007).

Included in the past and up-to-date are borehole drilling and logging of the core, gravimetric, magnetic prospecting, electric resistivity tomography (ERT), and shallow seismic tomography (SST) (Flechsig et al., 2015; Mrlina et al., 2007, 2009). The gravimetric survey and modelling suggests a structure with near-surface sedimentary cover, low-density volcanic material in the shallow depth, and higher density volcanic breccia in the lower part of the maar (Mrlina et al., 2007). The magnetic survey shows small circular peaks of increased magnetic intensity on the north and south edges of the maar as well as in the Železná hůrka volcano. Between these two volcanic structures, there is a zone of linearly elongated profiles of increased magnetic intensity orientated in the direction of the Tachov fault zone (TFZ) (NW-SE) (Flechsig et al., 2015). Flechsig et al., 2015 also conducted the ERT and SST, reaching modelled depths of circa 150 and 80 metres, respectively. The ERT results exhibit a lower-resistivity layer in the first 100 metres of depth which confirms the lithological results from borehole drilling (Mrlina et al., 2009).

The above methods determined the lateral dimensions of the studied structure but did not determine the depth of the crater, since they reached only down to the shallow subsurface (Flechsig et al., 2015; Mrlina et al., 2007, 2009). Therefore, in this study, we try to evaluate the dimensions of the maar structure and its sedimentary and volcanic fills by modelling the seismic ambient vibrations generated outside of the maar. The amplification of ground motions inside the maar body we simulate by technique described in Burjánek et al. (2019). Due to efficient acquisition of ambient vibrations, their use has become increasingly attractive in studies on local site effects. However, the interpretations of recordings are usually based on layered media assumption. In this study, the synthetic ambient vibrations are generated using a finite-difference method for generally heterogeneous three-dimensional media. They synthetics are processed in the same way as measurements and are compared to observed results from the ambient vibration survey. To test the different depths of the maar, we propose multiple

material models consisting of P-wave and S-wave seismic velocities of conical and cylindrical shapes with various dimensions.

2.2 Methods

2.2.1 The frequency-wavenumber array analysis method

The frequency-wavenumber (F-K) method, which was used in this study was developed by Capon, 1969, and improved in the Geopsy software by Wathelet et al., 2020 to a high-resolution three-component F-K analysis Wathelet et al., 2018. The seismogram is split into individual partially overlapping windows in the time domain, for which then the F-K spectra are calculated and averaged. The local spectral maxima representing the incoming waves of specific azimuth and phase velocity are then processed for each discrete frequency step within the investigated frequency range given by the geometry of the seismic stations array on surface. The minimum wavenumber resolution is controlled by the maximum distance between the neighbouring array stations (e.g., Wathelet et al. 2008). Meanwhile, the maximum resolved wavenumber relates to the minimum distance between the array stations. The considered seismic ambient noise is assumed (e.g., Bonnefoy-Claudet et al. 2006) to consist mainly of surface waves, the vertical and radial components can be used to determine phase velocities of Rayleigh waves. Similarly, the transversal component can then be used to analyse Love waves. The surface waves' phase velocities are frequency-dependent and the relation between the phase velocity and frequency is given by dispersion curves. We estimated the dispersion curves from array recordings using the Geopsy software (Wathelet et al., 2020), Wavedec (Maranò et al., 2012, 2017), and ArrayTools3C (Poggi & Fäh, 2010) to verify the integrity of the obtained dispersion curves of the Rayleigh and Love waves.

2.2.2 The inversion for the seismic velocity profiles

We used the dispersion curves to invert the seismic velocity profiles in Dinver module (part of Geopsy software). We assumed 1-D layered media with a fixed density of 2.2 g/cm^3 (Mrlina et al., 2007), and increasing velocities with depth. Therefore, we set our parametrization as a multi-layered model with variable thickness starting at 2.5 metres at the surface and ending at 20 metres at 200 metres depth. For each layer we set its possible velocity range and apply a constraint of the above mentioned increasing seismic velocity with depth. The software then randomly generates a given number of models which fit the input criteria. The synthetic dispersion curves are computed and compared with the observed dispersion curves, followed by optimization of the final model selection by the neighborhood algorithm (Sambridge, 1999; Wathelet et al., 2008), searching for the models within the given misfit range.

2.2.3 The site-to-reference spectral ratio (SRSR)

To determine the resonance frequency and the amplification ratio of the studied local effects of the maar, we used the site-to-reference spectral ratio computed

from ambient vibrations. The SRSR method was originally introduced for analysis of earthquake recordings (Borcherdt, 1970), nevertheless, SRSR calculated using noise recordings can still be representative of local site conditions (e.g., Irikura and Kawanaka 1980; Kleinbrod et al. 2017; Pischiutta et al. 2017). At least two simultaneous noise recordings were required, one located in the studied area and the second one in a near vicinity placed on the outcropping bedrock. Thus, we can determine the local site effect of the maar by eliminating source directivity and path effects by dividing the Fourier spectrum of each component of the station inside the maar by the spectrum of the corresponding component at the reference station outside. The Fourier spectra are determined by the multitaper method (Prieto et al., 2009). Assuming the seismic noise sources are all directional and randomly distributed in time and space (e.g., Bonnefoy-Claudet et al. 2006), the source and path effects are the same for stations located far away from the noise sources. Since we conducted the measurement in a secluded location, we did not see any effect of a nearby directional man-made source.

2.2.4 Ambient vibration simulations

Numerical simulations of ambient vibrations follow a two-step procedure based on generating Green's functions and the subsequent assembly of the noise time series for a given source distribution (Burjánek et al., 2019). In the first step, Green's functions are estimated using the reciprocity method by swapping the position of the source and the receiver (e.g., Eisner and Clayton 2001). In this way, it is possible to reduce the number of numerical simulations to 3 times the number of receivers by using three orthogonal point forces at the receiver locations to obtain a response from an arbitrary number of sources. In the second step, the synthetic noise time histories are generated by summation of responses to randomly distributed point-force sources, convolved with randomized source time functions. The details of the procedure can be found in Burjánek et al. (2019). For the numerical calculations of Green's functions, we used a finite difference method implemented in the SW4 code of N. Petersson and Sjogreen (2017). It can simulate seismic wave generation and propagation through a 3D inhomogeneous visco-elastic medium. The elastodynamic equations are approximated by the fourth order of accuracy in space using a grid-node-based finite difference approach, and by explicit time formulation. The SW4 also utilizes a curvilinear grid below topography and grid refinements allowing smaller grid spacing at the surface. The time step is calculated automatically based on the grid spacing, the computed frequencies, and local Vs velocities. The quality factors Qp and Qs are realized by viscoelastic modelling using three standard linear solid mechanisms providing correct damping for the frequency band of interest (0.5 – 10 Hz).

2.3 Field experiments

Ambient vibration data used in this study were collected using Lennartz LE-3Dlite MkIII seismometers, which are three-component short-period devices with a flat response of 1 to 100 Hz. For the digitisation and recording of measurements, we used A/D converters with a bit-depth of 31 bits per sample. The positions of the sensors were measured using an accurate Differential GPS (DGPS) receiver

that provides 1 cm precision. The seismometers were placed on customised tripods, which allowed a comfortable setting (both for levelling and orientation). Whenever possible, sensors were placed in shallow pits of 20 cm to achieve better coupling with the ground, by removing the most unconsolidated soil layer, and to provide more protection against wind gusts.

We have deployed the seismic arrays at two locations to estimate the shear wave velocity structure of the crater infills (Figure 2.1). The centre of the first array was 90 meters north of the borehole and the centre of the second one was 110 m west of the MY-1 borehole. The borehole log shows only the lacustrine sediments within its whole depth of 80 m. The sediments comprise of interbedded sand, clay, and silt layers (Mrlina et al., 2009). The aim of the first array (Array 1) was to estimate the shear wave velocity of the maar's lacustrine sediments. It consisted of a station in the centre, 3 stations 5.5 meters from the centre and 120 degrees apart creating a triangle, and two pentagons rotated by 36 degrees to each other and with diameters of 25 and 50 meters respectively. The stations were positioned in the vertices of these geometrical shapes, 14 stations were used in total. The aim of the second array (Array 2) was to estimate the shear wave velocity of volcanic breccia. The geometry of Array 2 followed the geometry of Array 1, except for the smallest 5-meters triangle, which was at the southern vertex of the large 50 m pentagon, due to dense vegetation in the central part of Array 2. Moreover, ambient vibrations were recorded along a profile, to map seismic response from the centre to the border of the diatreme infills (Figure 2.1). A reference station was always placed at the southern edge of the crater. The measurements were performed in three different time periods and several reference positions were tested (MYR104, MYR007, MYR003), with no significant differences in the recordings. The country bedrock consists of competent phyllites, quartz phyllites, and quartz lenses with mica schists (Fiala & Vejnar, 1997; Tonica et al., 1998). The H/V spectral ratio calculated for the reference station did not show any peak through the studied frequency range from 0.5 – 10 Hz (see Figure S2.1 in the Supplementary material). At least one hour of continuous records was obtained for each of the setups.

2.4 Results

2.4.1 Array analysis

For creating the 3D velocity model, we estimated the seismic velocities at the selected site of the Mýtina maar using the array measurements. All Geopsy, Wavedec and ArrayTools3C codes were used for the estimation of the dispersion curves, resulting in a good agreement between the different estimates. The Wavedec dispersion curve was estimated in a narrower frequency band with respect to high-resolution methods. The results of three-component high resolution F-K analysis estimated by ArrayTools3C code are shown in Figure 2.2. Array 1, located on the lacustrine sediments, has yielded dispersion curves between 4 and 14 Hz of the fundamental mode of Love (L0) and Rayleigh (R0) waves (Figure 2.2a and 2.2b, respectively). In contrast, for Array 2, located on the volcanic breccia, we were not able to determine the L0 dispersion curve, and we could only use the R0 between 5 and 15 Hz (Figure 2.2c).

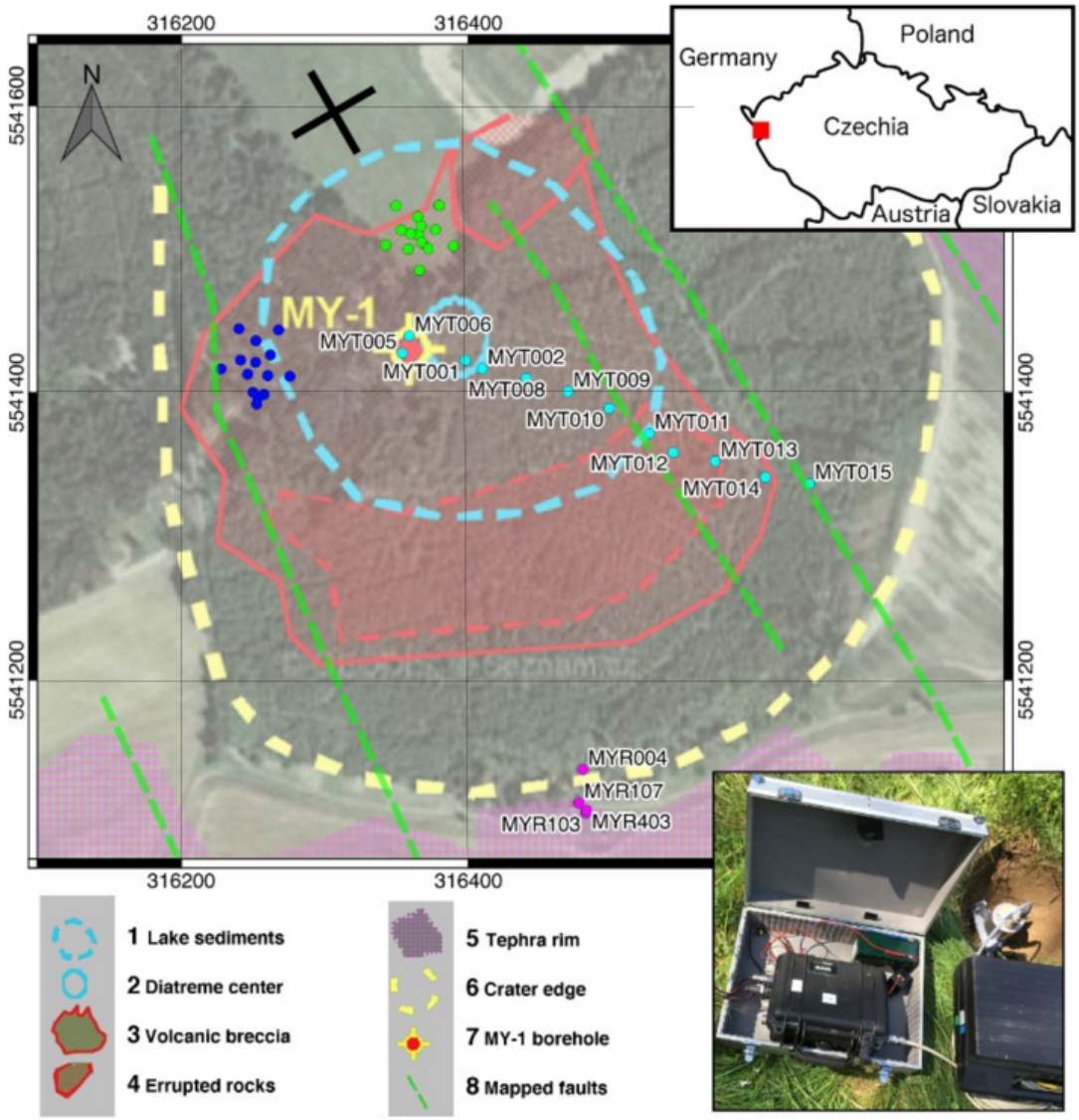


Figure 2.1 An overview map of the researched area showing the positions of the seismic sensors (dots) and mapped maar features (modified after Mrlina et al. 2009). Two array configurations are shown (green dots: Array 1 - lacustrine sediments; blue dots: Array 2 - volcanic breccia). Maar features as presented by Mrlina et al. (2009): 1) approximate contour of the lacustrine sediments; 2) centre of maar-diatreme; 3) volcanic breccia; 4) erupted magnetic rocks accumulations; 5) relicts of tephra rim outside the crater; 6) morphological edge of the crater; 7) MY-1 borehole; 8) Mapped faults of the Tachov fault zone (Flechsig et al., 2015). The positions of the consecutive double-station measurements are indicated by cyan dots. The positions of the reference stations at the southern edge of the crater are shown by purple dots. The black solid cross indicates the two dominant directions of the resonance (discussed later in the results section). The coordinates are given in m of WGS84 UTM projection in the 33N zone. The inset map (top right) displays the position of the Mýtina maar (red square) in a regional context, while the inset photo (bottom right) shows the typical field installation.

Inversion of the dispersion curves was done using the Dinver module of the Geopsy software. The inverted profile was divided into layers with increasing thickness and range of S-wave velocities to be searched through. We forced increasing velocity with the depth option since we did not expect any low-velocity

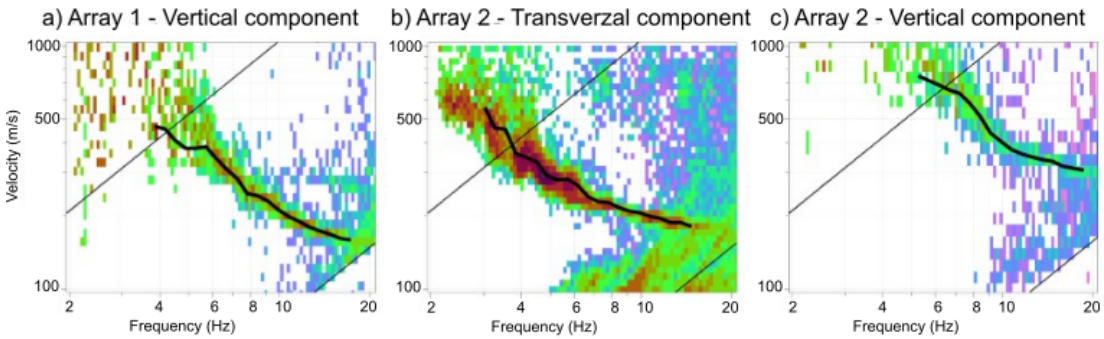


Figure 2.2 Three-component high-resolution F-K (3C-HRFK) processing results for the vertical component of Array 1 (a), the transversal component of Array 1 (b), and the vertical component of Array 2 (c). They correspond to the histograms of the analysed time windows at the respective frequency ranges. Thin solid and dashed black lines are the array resolution limits. Thick solid black lines are selected from the data, where the central line indicates the best-fitted values obtained by fitting a Gaussian.

layers according to the borehole log. The resulting profile of the first array show increase in velocities, but no distinctive interface (Figure 2.3c), however, the second array data results show an interface at 20 meters depth due to significant step-like increase of S-wave velocity (Figure 2.4b, Table 2.1). The velocity profile inversions resolution depth using dispersion data is usually related to a fraction of the maximum resolved wavelength in the phase velocity (λmax). For example, (Cox & Teague, 2016) proposed setting the resolution depth from λmax/3 to λmax/2. Considering the upper bound (λmax/2), the estimated resolution depths are 85 m and 75 m for Array 1 and Array 2, respectively. This is reasonable since the scatter of the inverted profiles starts to increase below these depths (Figures 2.3, 2.4). The best fitting velocity profiles were then used for characterization of the 80 meters-deep lacustrine fill and the superficial S-wave velocity of the volcanic breccia.

Depth (m)	Vs sediments (m/s)	Vs inner breccia (m/s)	Vs outer breccia (m/s)
0	166	193	221
20	256	312	369
40	564	668	772
60	625	764	903
80	741	947	1153

Table 2.1 Shear-wave velocities were obtained from array analysis. Array 1 corresponds to Vs sediments, Array 2 then to Vs outer breccia. Vs of the inner breccia in the first 100 metres was set as a mean value between the two arrays.

2.4.2 Development of the 3D model

The development of elastic 3D models material parameters (P-wave velocity, S-wave velocity, and density) of Mýtina maar was based on the density model in Mrlina et al. (2009). This model describes the near-surface geological parts of the maar. These include sedimentary fill lying on top of a volcanic breccia which is

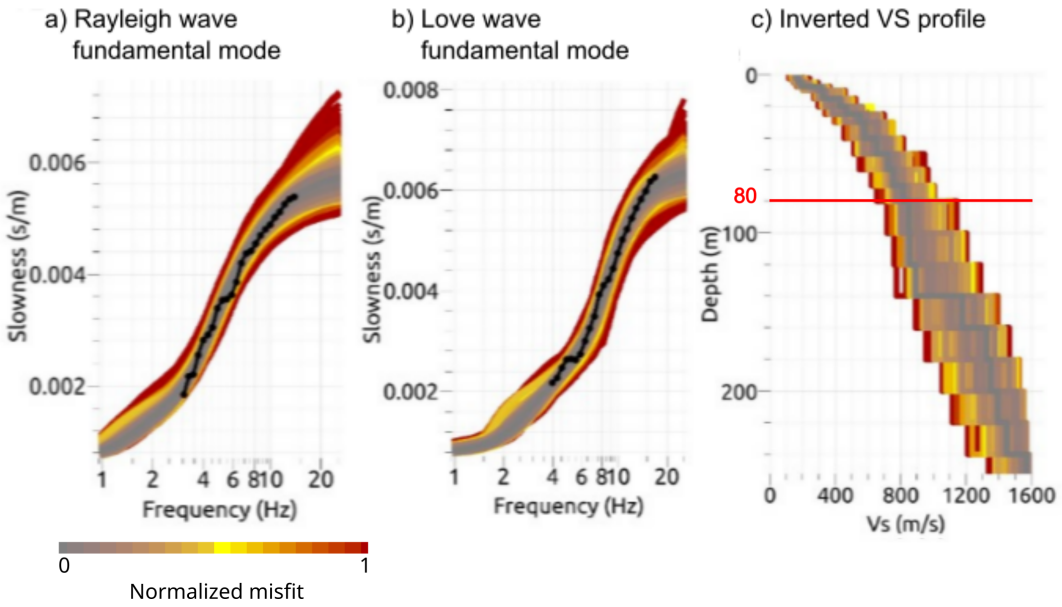


Figure 2.3 Inversion results for Array 1, (a) Array 1 – fundamental Rayleigh mode, (b) Array 1 – fundamental Love mode, (c) Array 1 – inverted Vs profile. Synthetic data from the inverted models are drawn using a colour scale. The depth of 80 m is the estimated resolution depth.

enveloped by an outer denser volcanic breccia, which has a similar density as a surrounding country bedrock (see Figure 2.1).

Superficial S-wave velocities of the maar infills were well constrained by the array analysis in the top 80 metres. Although the S-velocity is not well resolved below 80 m, we used the increase of the velocities observed in the inverted profile of Array 1 down to a depth of 200 m. Shear wave velocity of 1500 m/s was assumed as a maximum velocity of volcanic breccia and was kept constant below the depth of 200 m. For the country bedrock, we used values from regional tomography (Málek et al., 2005). The inverted velocity profile of Array 1 was used to simulate the lacustrine sediments, the profile based on Array 2 was then used for the breccia at the outside edges of the maar and in the depth also for the breccia under the lacustrine sediments. According to the gravimetric survey (Mrlina et al., 2009), the inner breccia has lower density and presumably lower Vs velocity with respect to the outer breccia. Since we have velocity profiles estimated only for two locations (Array 1 – central part of the maar; Array 2 - outer part of the maar infill) and not for the inner breccia (transition zone from the centre to the edge of the maar), we used a horizontally averaged value for the inner breccia. The P-wave velocity was set so that Vp/Vs ratio equals square root of 3 for the whole model.

The modelling aimed to test different 3D velocity models and to determine the depth of the volcanic breccia, which could not be obtained from the inversion of a gravimetric survey (Mrlina et al., 2009) and the sensitivity of synthetic seismic noise modelling to the changing depth of the models.

The initial material model was a 3D vertical cone of a maar structure in the regional bedrock (Málek et al., 2005). To test the depth sensitivity, we also created a vertical cylindrical model representing an infinitely long cone. After setting the lateral dimensions of the cone and determining the depth, we added

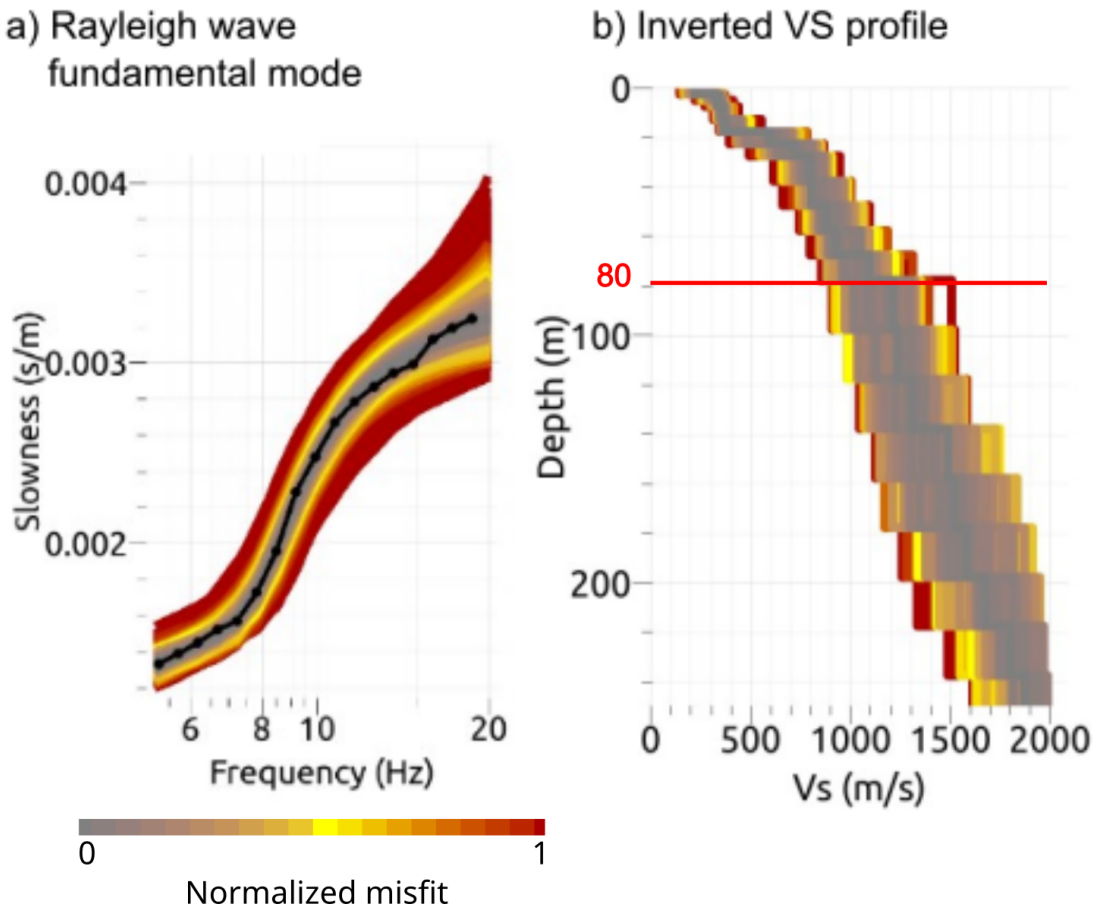


Figure 2.4 Inversion results for Array 2, (a) Array 2 – fundamental Rayleigh mode (b) Array 2 – inverted Vs profile. Synthetic data from the inverted models are drawn using a colour scale. The depth of 80 m is the estimated resolution depth.

the sedimentary fill in the top centre of the cone and tested its influence on the ground motion amplification levels. According to Mrlina et al. (2009), we also added a transition zone of the outer breccia (see Figure 2.5). As a next step, we likewise changed the shape to an elliptical cone to simulate different resonant frequencies in two perpendicular directions. Finally, we adopted a viscoelastic model described by quality factors Qp and Qp based on the empirical formulas of Campbell (2009). For Qs, we used the relation Qs = 7.17+0.0276*Vs, where Vs is seismic shear wave velocity in [m/s] at the depth, while Qp =2Qs.

2.4.3 Synthetic seismic noise analysis

The seismic noise simulation has been computed using the fourth-order finite differences code SW4 (N. A. Petersson & Sjögreen, 2015; N. Petersson & Sjogreen, 2017). The computational grid is 4 x 4 x 2 km with a horizontal and vertical spacing of 10 m with two refinement grinds at 100 and 40 meters in depth, each of them dividing the spacing to 5 and 2.5 metres, respectively and therefore keeping the requirement of at least 6 points per S-wave wavelength even for near surface low velocity layers.

The six selected stations (one located outside of the maar on the bedrock, and 5 stations in the maar aligned on a profile pointing from the centre of the maar

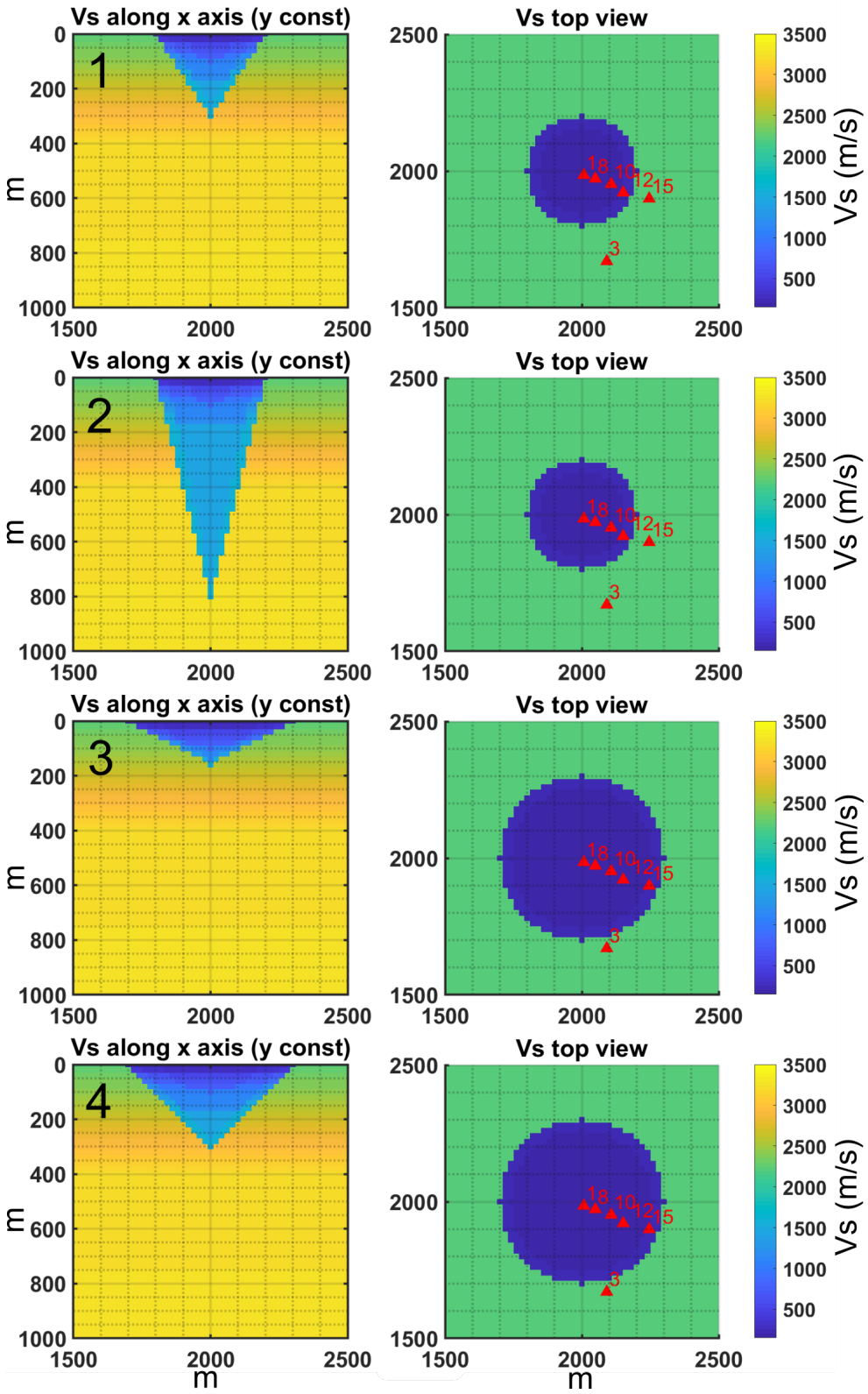


Figure 2.5 Cont'd.

to the edge) were adopted in the simulations. The seismic source is composed of independent body forces in 3 perpendicular directions and the displacement is registered in the same 3 directions for each of the forces resulting in 9 computed components of the Green's tensor for each receiver. We created two grids of 92 x

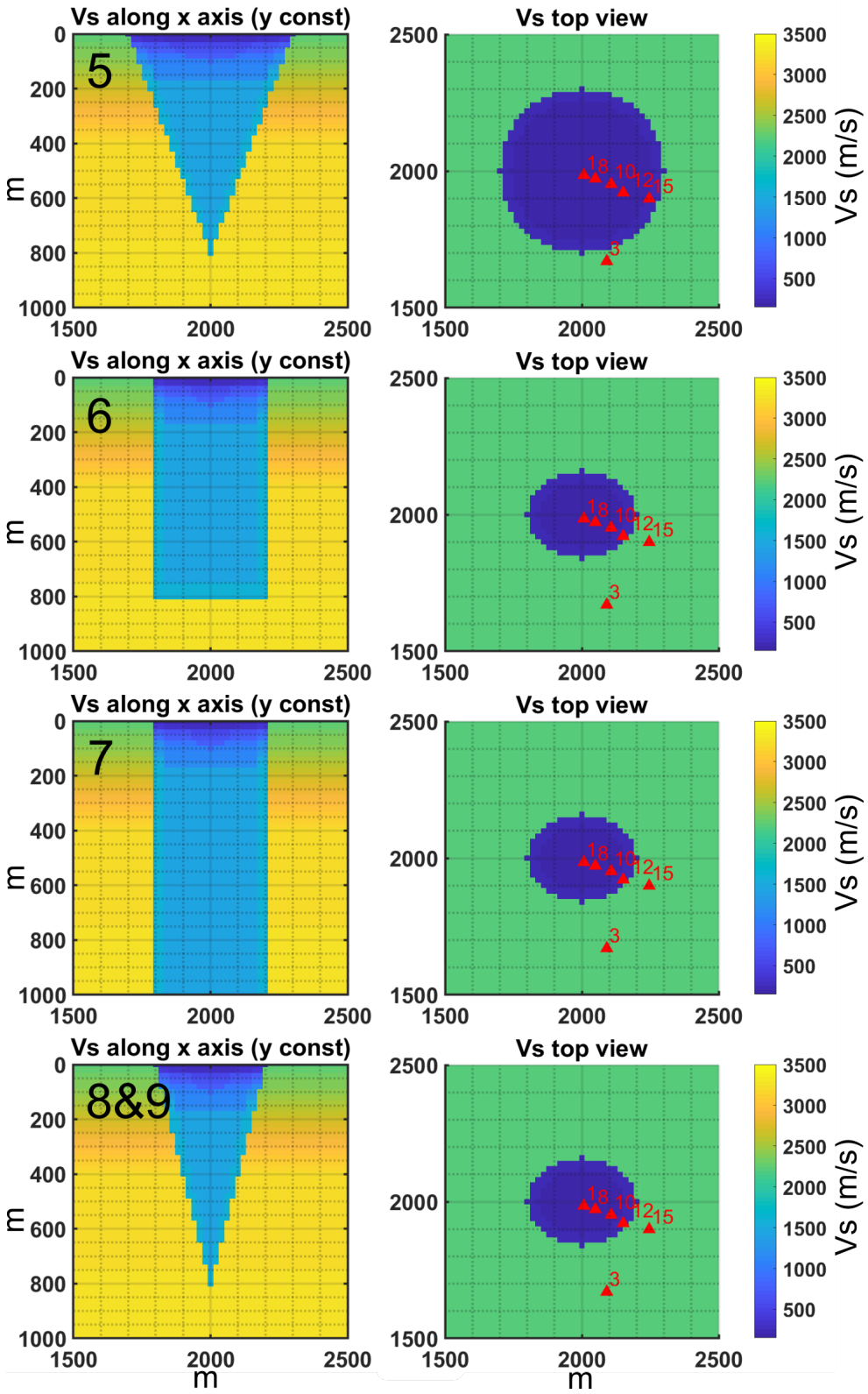


Figure 2.5 Shear wave velocity models' cross-sections. Left side: vertical shear wave velocity cross-section, Right side: horizontal view of shear wave velocity of models 1 to 8, sorted like in Table 2.2. Viscoelastic Model 9 has the same shear wave velocity as Model 8, which is purely elastic.

92 virtual receivers (locations of the noise sources) at depths of 0 and 1 km. The virtual receiver grids are spaced by 30 meters and are offset by 600 metres from the horizontal edges of the computational grid to avoid entering inside the absorbing boundary. Two hours of noise synthetics were then generated by summation of responses to randomly distributed point-force sources, convolved with randomized source time functions as in Burjánek et al. (2019).

The synthetic seismograms were analysed by Site-to-reference spectral ratio (SRSR), with the station outside of maar as a reference station. We computed Fourier spectra from 0.5 to 30 Hz of the seismograms. The spectra were then divided by the spectrum of the reference station outside of the maar, all for respective components. We searched the SRSR for the peak of the fundamental mode resonance frequency (automated search where the derivative of the curve is smaller than a set threshold for a certain number of values, starting the search from the lowest frequencies) and obtained the frequency and amplification level at that frequency. We compared these results with the observed data.

Several velocity models with an increasing level of complexity were tested. The sensitivity of the resulting resonance frequencies on the dimensions of the crater was explored. In addition, some of these models were further modified to fit the observed response. All models are listed in Table 2.2 and corresponding cross sections of the 3D velocity models are shown in Figure 2.5. Table 2.2 also shows modelled frequencies of the fundamental mode and corresponding amplification levels at station MYT001, which is situated right at the centre of the maar infill and the strongest amplification was observed at this station. All these models adopt lacustrine sediments, inner breccia, and a transition zone 40 metres wide of the outer breccia. The first five models shown are circular cones with various radii of sediments and breccia and differ in depth. Models 1 and 2 have depths of breccia cone set to 300 and 800 metres to test sensitivity to the absolute depth of the crater. The difference in resonance frequency is most significant on the vertical component, but also present on the horizontal components. The amplification levels are lower on all components in case of the Model 2.

The next three models – 3, 4, and 5 – have a longer radius of sedimentary fill and breccia by 100 metres compared to models 1 and 2 and are also tested for different maximum depths of breccia. The bigger diameter of the models results in both decrease in the resonance frequencies and the amplification levels, compared to models 1, and 2.

Models 6 and 7 are elliptical cylinders with circular sedimentary fill and elliptical breccia structures. The major 200 m axis and the minor 160 m axis are set to test the splitting of the resonance frequency in two perpendicular horizontal directions, which is later observed in the data. Furthermore, the maximum depth of 2000 metres for the breccia in model 7 is set to study the possible depth sensitivity of the resonant frequencies. The results show that models 6 and 7 differ only by 0.01 Hz at all components of the resonance frequency and only by a factor of 10 for the amplification ratio on the Y component. That is the fundamental frequency becomes insensitive to the maximum depth, and 2D resonance develops in case of models 6 and 7.

The last two models 8 and 9 are elliptical conical breccia structures with circular sedimentary fill and are the most complex ones. Model 8 is purely elastic, whereas model 9 also adopts visco-elasticity characterized by quality factors Qp

and Qs. The resonance frequency is the same in the case of both models, but the amplification level is strongly reduced (compare component in Figures 2.6a and Figure 2.7).

Model	Sediments rad. (m)	Sediments thick. (m)	Breccia rad. (m)	Breccia thick. (m)	f_0^X (Hz)	f_0^Y (Hz)	f_0^Z (Hz)	A_0^X	A_0^Y	A_0^Z
1	100	100	200	300	1.88	1.89	2.2	83	76	30
2	100	100	200	800	1.81	1.83	2	72	63	22
3	200	100	300	150	1.73	1.74	2	66	60	12
4	200	100	300	300	1.62	1.62	1.87	56	50	18
5	200	100	300	800	1.52	1.52	1.68	43	37	18
6	100	100	160-200	800	1.83	1.88	2.05	80	70	24
7	100	100	160-200	2000	1.82	1.87	2.04	78	60	24
8	100	100	160-200	800	1.85	1.91	2.1	82	70	30
9	100	100	160-200	800	1.85	1.91	2.1	35	31	20
obs					1.83	1.91	1.83	23	25	6

Table 2.2 Models' geometry and resulting resonant frequencies and amplification levels: radius of sediments; thickness of sediments; radius of breccia; thickness of breccia; f_0^X, f_0^Y, f_0^Z the fundamental frequency at components X, Y, Z; A_0^X, A_0^Y, A_0^Z – amplification levels (SRSR) for the components X, Y, Z at the corresponding resonance frequencies (f_0^X, f_0^Y, f_0^Z). See Figure 2.5 for the geometry of the models. Observed data marked with an abbreviation: obs

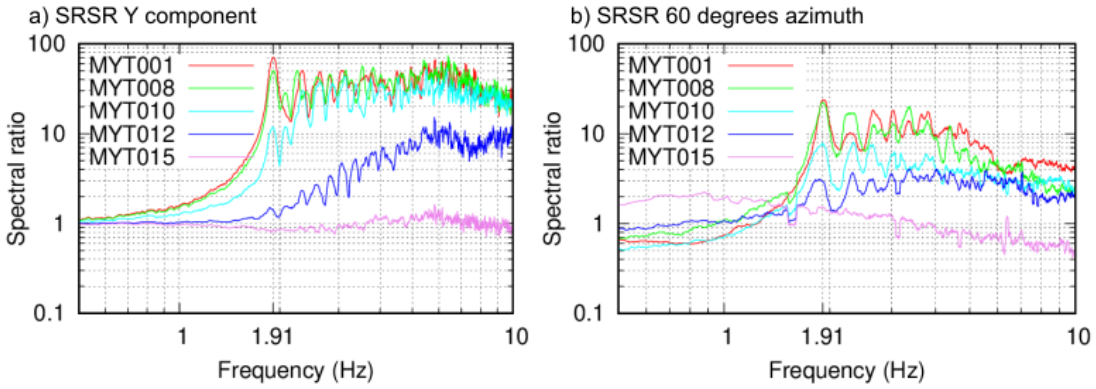


Figure 2.6 Simulated and observed site-to-reference spectral ratios: a) SRSR of the Y synthetic component for the elastic elliptical cone model 8, b) SRSR of the corresponding observed rotated data by 60 degrees clockwise from north).

2.4.4 Comparison with the observed data

The comparison of modelled and observed spectral ratios for five site-to-reference station pairs are provided in Figures 2.6 and 2.7. The recorded seismograms were systematically rotated around the vertical axis in order to decouple two perpendicular resonance modes observed on the horizontal components. In particular, SRSR were calculated for each of these directions and the optimum rotations were estimated. The observed data have a peak of fundamental mode resonance frequency at 1.91 Hz for the component rotated by 60 degrees clockwise from north (see Figure 2.6b) and 1.83 Hz for the component rotated by 150 degrees (Figure 2.7). The vertical component varies between these two values, creating

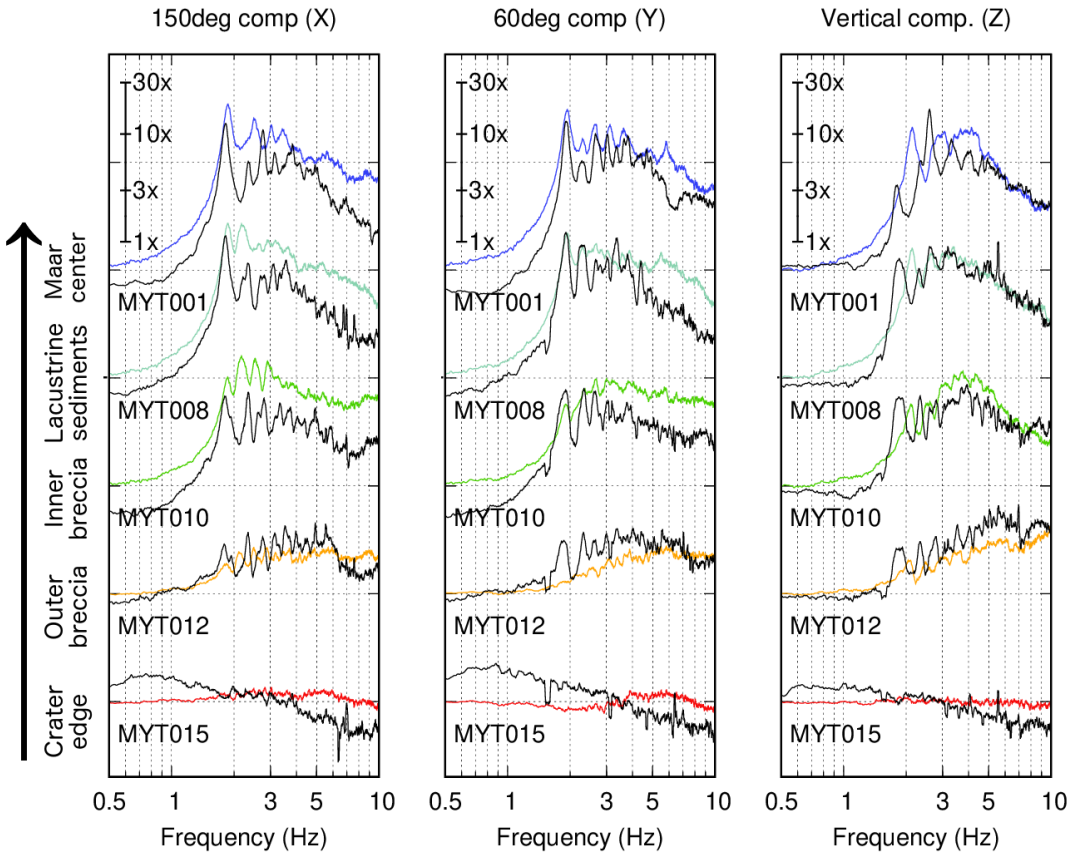


Figure 2.7 Simulated and observed site-to-reference spectral ratios considering the visco-elastic model 9 (color) and observed data (black) for two horizontal components (150 degrees and 60 degrees) and the vertical component of ground motion. The order of the curves in the plots (from bottom to top) roughly follows the profile from the center of the maar to its border.

a wide peak (Figure 2.7). The azimuth of 150 degrees is aligned with the slight elongation of the studied maar valley, which is also aligned in the same direction as TFZ (Flechsig et al., 2015), the azimuth of 60 degrees is then in agreeance with the minor elliptical axis of the valley. Since we do not observe any preferential directions of motions at reference station MYR003 which is located just at the crater edge of the maar and within the TFZ, the observed directionality originates in the maar infills. The observed directions of N150 and N60 might result from the geometrical shape of the crater, which could have been shaped by the lava effusions along the TFZ.

To simplify the modelling, we set the major and minor axis of the ellipse in the directions of the Cartesian coordinates X and Y of the computational domain respectively. The observed data Cartesian system was rotated by 60 degrees to have the azimuth 60 and 150 degrees, which is in agreement with the TFZ (oriented about 150 degrees NW-SE).

A detailed comparison with the measured data is performed for the most complex models 8 and 9, which show the best agreement with the observations. As we can see in Figure 2.6, the synthetics generated for model 8 agree with the observed data in terms of the resonance frequency of the fundamental mode, but the amplification level is much stronger in the case of synthetics. The resonance

frequency is the same at all the stations, that is, the whole maar resonates as a whole body and exhibits a 3D local effect. Also, the modelled amplification decreases at the stations (MYT008 and MYT010) further from the centre of the maar (station MYT001), in agreement with the observed trend. Stations MYT012 and MYT015 located at the very edge of the maar fills, are showing a low peak in both cases, which demonstrates the possibility of mapping the lateral dimensions of the maar infills by ambient noise measurements.

Finally, the comparison with the observed response is done for the visco-elastic model 9 (Figure 2.7). The synthetic amplification curves show a better fit to observed amplification curves for elastic model 8. For comparison see the Figure 2.8, which shows the best fit for the models 1-9. The frequency misfit was calculated using Equation 2.1:

$$misfit\ F = |syn\ f_0^x - obs\ f_0^x| + |syn\ f_0^y - obs\ f_0^y| + |syn\ f_0^z - obs\ f_0^z|, \quad (2.1)$$

where f_0^X, f_0^y, f_0^z are fundamental frequencies for the synthetic model (marked syn) and observed data (marked obs). The spectral ratio misfit was calculated using Equation 2.2:

$$misfit\ A = |log\ (syn\ A_0^x) - log\ (obs\ A_0^x)| + |log(syn\ A_0^y) - log\ (obs\ A_0^y)| + |log(syn\ A_0^z) - log\ (obs\ A_0^z)| \quad (2.2)$$

where A_0^X, A_0^y, A_0^z are spectral ratios for the synthetic model (marked syn) and observed data (marked obs).

In the case of the horizontal components, both the resonance frequency and amplification level of the fundamental mode are better explained, and, on top of that, the level of high-frequency amplification is fitted as well. In the case of the vertical component, the synthetics show still a higher resonance frequency of 2.1 Hz than the observed data (see Figure 2.7 and Table 2.2 for comparison between the models). All the tested conical and cylindrical models show the modelled vertical resonance is decoupled from the horizontal ones and the resonant frequency is generally higher for the vertical component, in contrast to the observations at Mýtina maar (Figure 2.7). Comparisons with the observed data for all models 1 – 8 is shown in Figure S2.2 of the Supplementary material.

2.5 Discussion

Although the presented models are rather simple, they fit surprisingly well with the observed response and can be used as a proxy for the crater's estimated depth. Nevertheless, these models can hardly be considered as unique subsurface images of Mýtina maar. The simulated resonant frequencies and amplification levels are dependent on many parameters, and some of them are not well constrained. To make reliable depth estimates, it is necessary to constrain the seismic velocities of the crater infills (lacustrine sediments, breccia). Seismic velocities used to create the maar material parameter models in this study were set according to the array measurements valid only for the shallow subsurface down to the depths of 80 m. For the deeper parts of volcanic breccia, the value of 1500 m/s for the shear wave

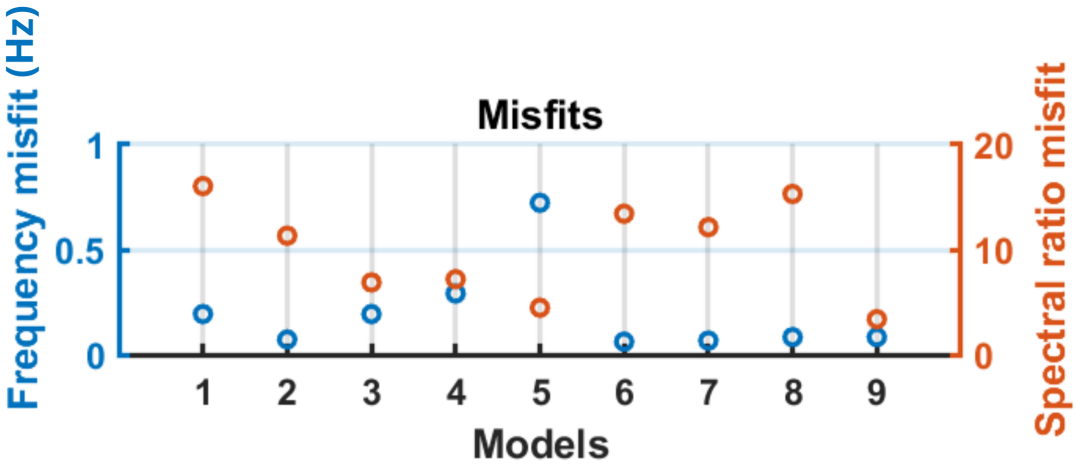


Figure 2.8 Comparison between the models and observed data on the station MYT001. The blue circles show frequency misfit of all 3 components combined, the red circles spectral ration misfit of all 3 components combined.

(S-wave) velocity was not constrained by any in situ data and was only assumed. However, it is in accordance with Gebhardt et al. (2011), who reported values of 2400 m/s for an acoustic wave (P-wave) in volcanoclastic breccia. Yet, the extrapolation of seismic velocity in breccia, as done in this study, might still cause a substantial error in the determination of the crater's depth.

The Vp/Vs ratio of the square root of 3 (1.73) was assumed for the entire model and was taken from the regional velocity model (Málek et al., 2005) for the seismically active zone of Nový Kostel, 25 km north of the Mýtina maar. Other Vp/Vs ratios were not tested, as we presumed low sensitivity of the resonant frequencies to the Vp velocity structure. It is likely, that the layer of the lacustrine sediments has a higher Vp/Vs due to high water saturation. Therefore, heterogeneous Vp/Vs ratios are another complexity, which might be introduced to such modelling in future.

The lateral dimension of the crater's infill has also a strong influence on the results (resonant frequencies, amplification levels). Therefore, before even testing the model's sensitivity to the crater's depth, one should constrain the lateral dimensions by available geophysical measurements. This can be taken, for example, from a map of geomagnetic anomalies or dense ambient vibration measurements.

The results for cylindrical models (models 6 and 7) shows that studied 3D resonance has a limiting threshold in sensitivity of depth determination. In particular, in case of deep craters with steep walls, 2D resonance develops and resonant frequencies do not depend on the absolute depth of the crater anymore.

Therefore, a priori knowledge of the shape and structure of the studied crater should be considered, if available. It is illustrated in Figure 2.8, where we observe the best frequency misfit between the models and the data at station MYT001 and synthetics of models 6 – 9. The results are very similar regardless of geometry (cylindrical versus conical) and depth (model 7 with depth of 2000 m, 6, 8, 9 models 800 m). Added to that, models 6, 7, and 8 exhibit a very similar spectral ratio misfit. Nevertheless, the model 9, with identical dimensions and the velocity parameters as model 8, has the best spectral ratio misfit due to the applied attenuation. Models 2, 6, 7 would have lower spectral ratio misfit comparable to model 9 if the attenuation is considered in the modelling. At the station MYT012, placed within the outer breccia, we observe that the vertical component resonance frequency is not split from the horizontal ones, and that it is fitting the observed data best of all cases (Figure S2.2 in Supplementary material). This indicates that the boundary between the maar and the bedrock might be steeper and/or have more complicated shape (e.g., parabolical) than it is suggested in models 8 and 9.

The modelled resonance was clearly decoupled on both horizontal and vertical components. The vertical component fundamental mode frequency was significantly higher with respect to horizontal components. In contrast, such decoupling is not observed for the recorded ground motions at Mýtina maar. That is, the same resonant frequencies were observed for the vertical and horizontal components. This is quite a fundamental inconsistency, which might be addressed by more sophisticated models. For example, the models assumed in this study are rotationally symmetrical along the vertical axis (except the elliptical models). However, crater infills could be generally more complex, containing lateral inhomogeneities in form of volcanic veins, and layers of high-velocity volcanic rocks as shown, for example, by Závada et al. (2011) for Boren diatreme.

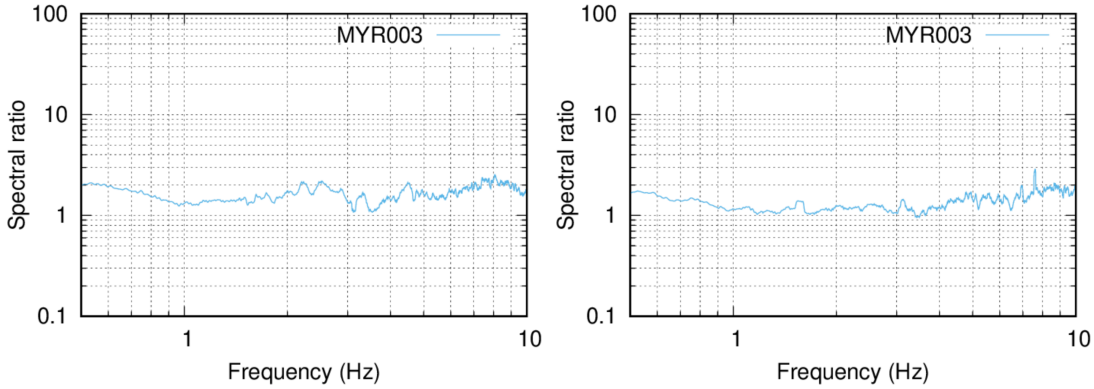
2.6 Conclusions

We propose a 3D model of the maar Mýtina comprising seismic velocities, density, and attenuation. The model was used for simulating seismic wave propagation in the maar infills. The modelled seismic wavefield shows amplification of seismic waves inside the maar relative to the reference station outside in the bedrock. The amplification is split into two modes, this can be explained by the elliptical shape of the maar cone, where each half-axis corresponds to each resonance frequency. The surface lateral dimensions of the maar were selected from previous studies and field measurements, leaving the model unconstrained in the larger depths. Using the synthetic noise data, we demonstrate possibility of mapping the lateral dimensions of the maar infills by ambient noise measurements. From modelling, the depth of the maar breccia cone was determined to be around 800 m. The depth resolution is better for the initial cylindrical cone model, where the vertical resonance frequency has changed more significantly than for the elliptical cone. The subsurface sedimentary layer causes stronger ground motion amplification and a shift in the resonance frequency of the entire structure and cannot be neglected. The simulations based on perfectly elastic models overestimate the observed amplification levels, while seismic attenuation can limit the amplification levels to reasonable values.

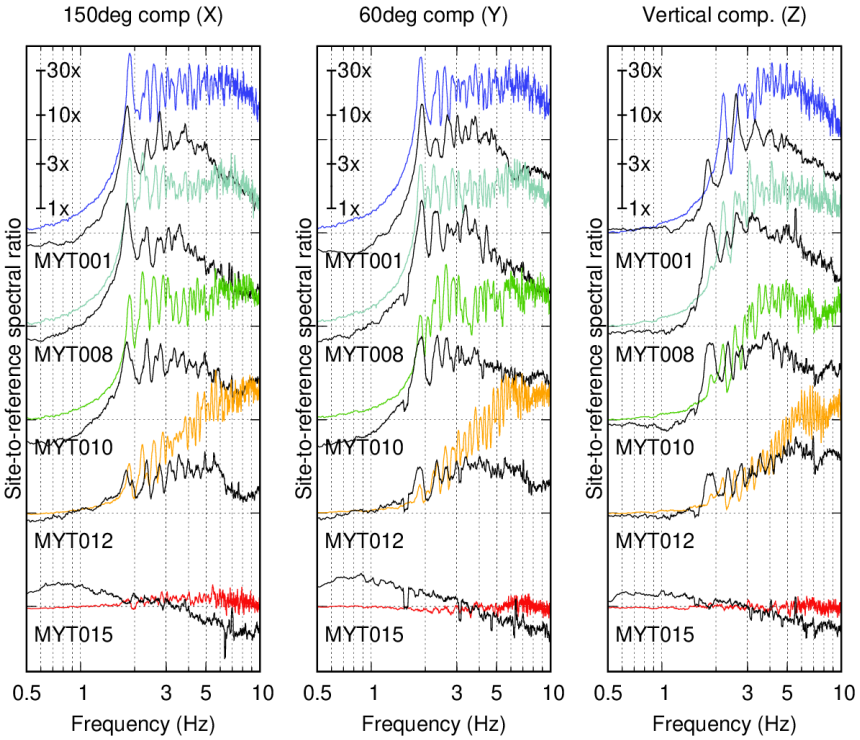
2.7 Acknowledgements

We would like to thank Shinichi Matsushima, Marta Pischiutta and anonymous reviewer for constructive comments and helpful reviews. We also thank Anders Petersson and Björn Sjögreen for making their FD code SW4 available. This work was supported by Czech Science Foundation (GACR), project no. GA20-15818S, and by the Ministry of Education, Youth and Sports of the Czech Republic through the e-INFRA CZ (ID:90140).

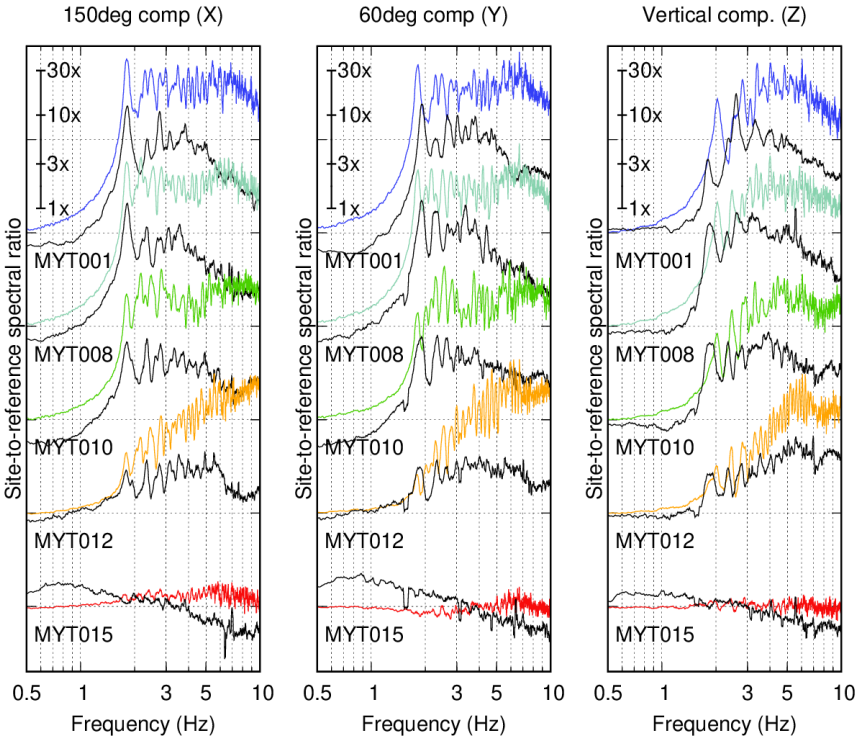
2.8 Supplementary material



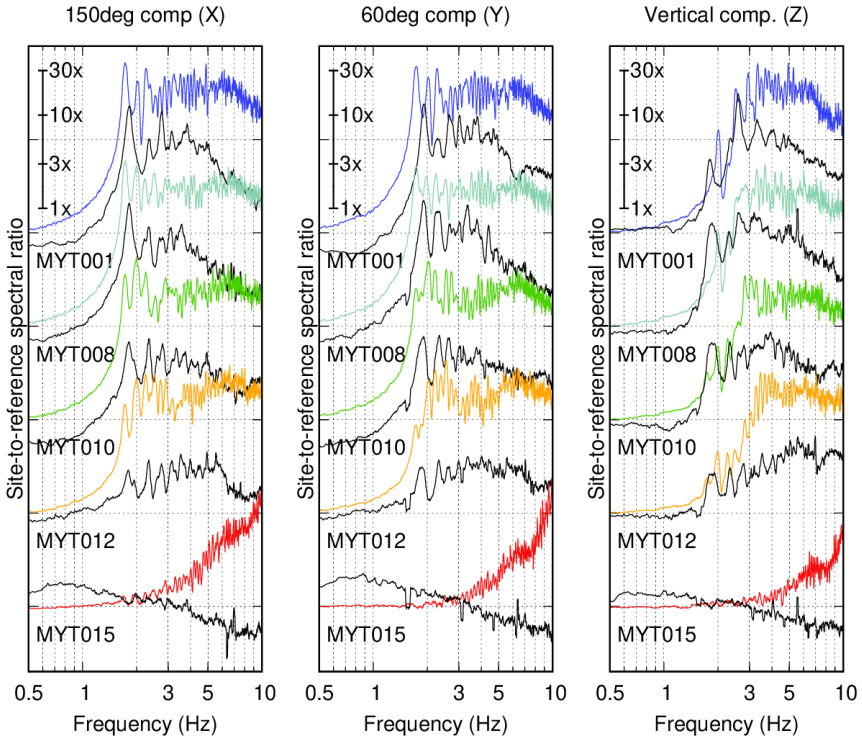
Supplementary Figure 2.1 Comparison between the models and observed data on the station MYT001. The blue circles show frequency misfit of all 3 components combined, the red circles spectral ration misfit of all 3 components combined.



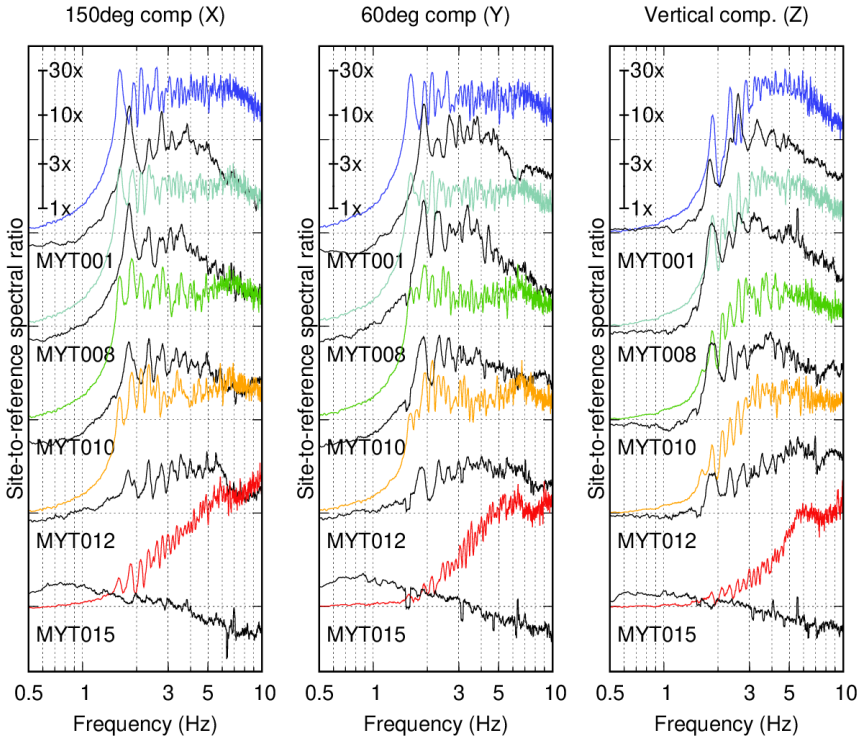
Model 1



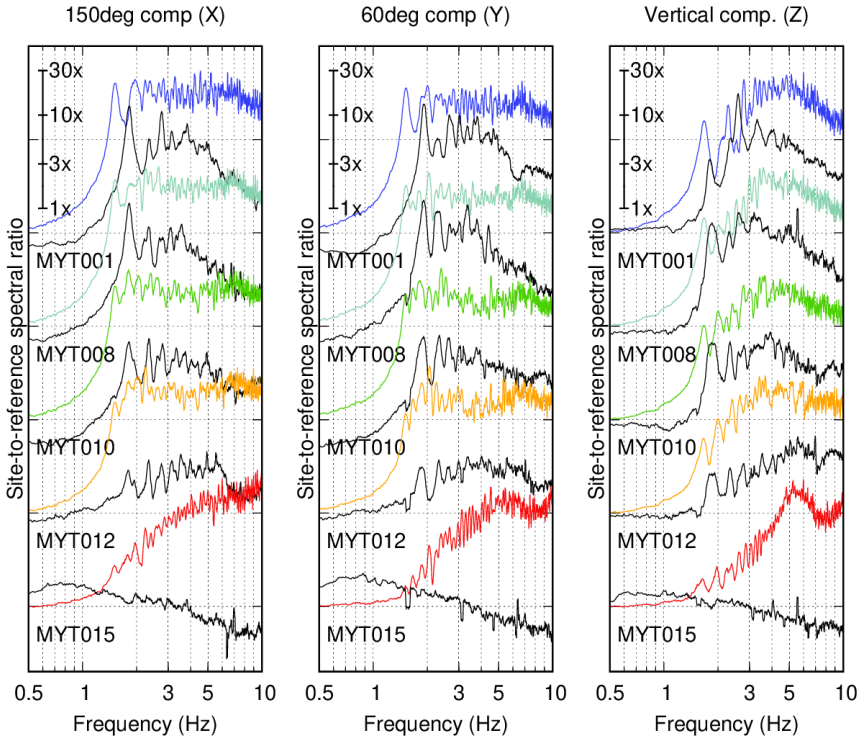
Model 2



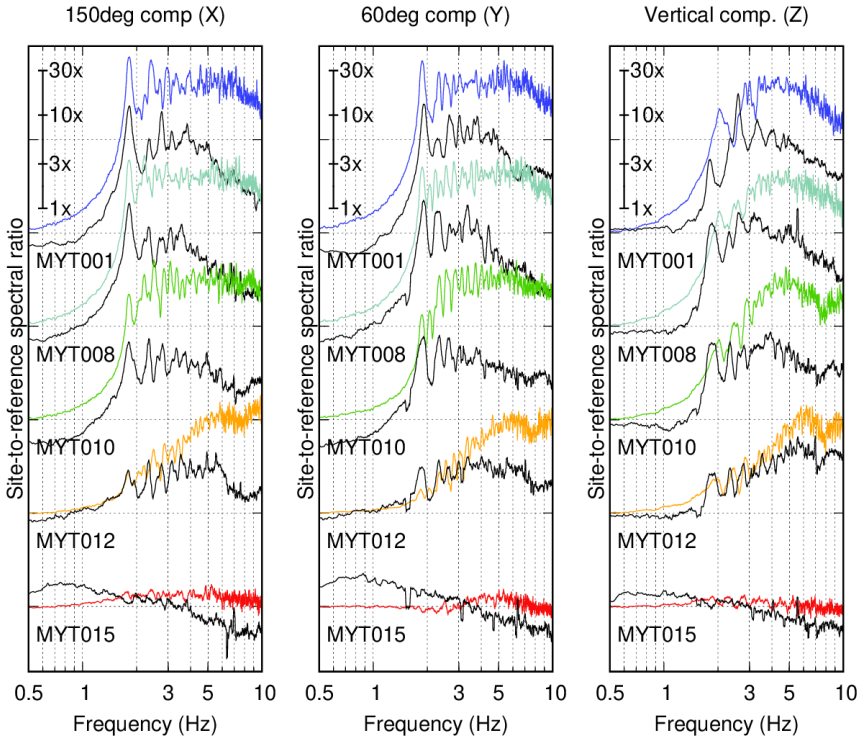
Model 3



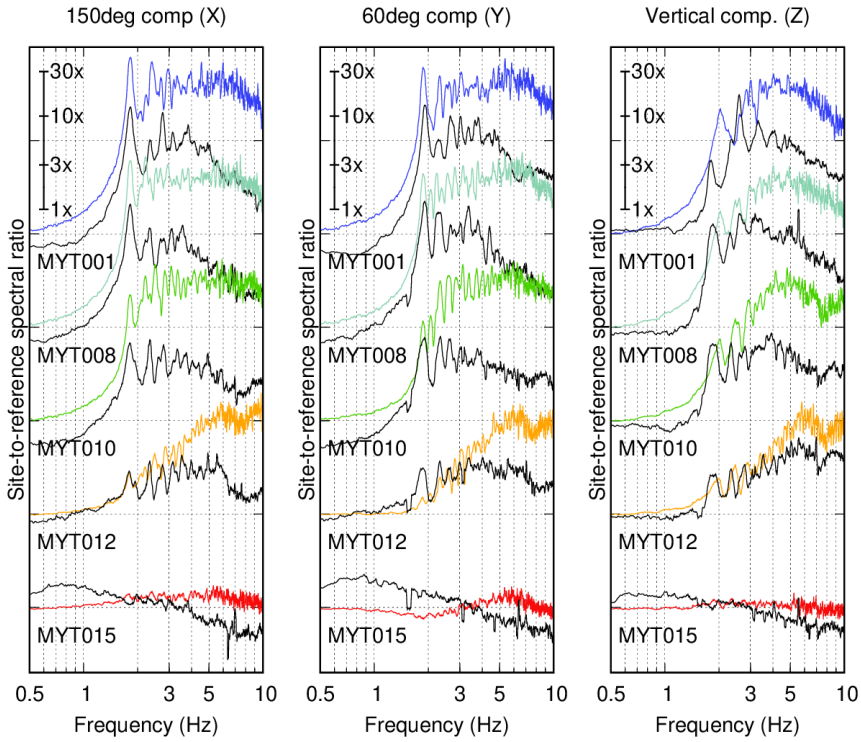
Model 4



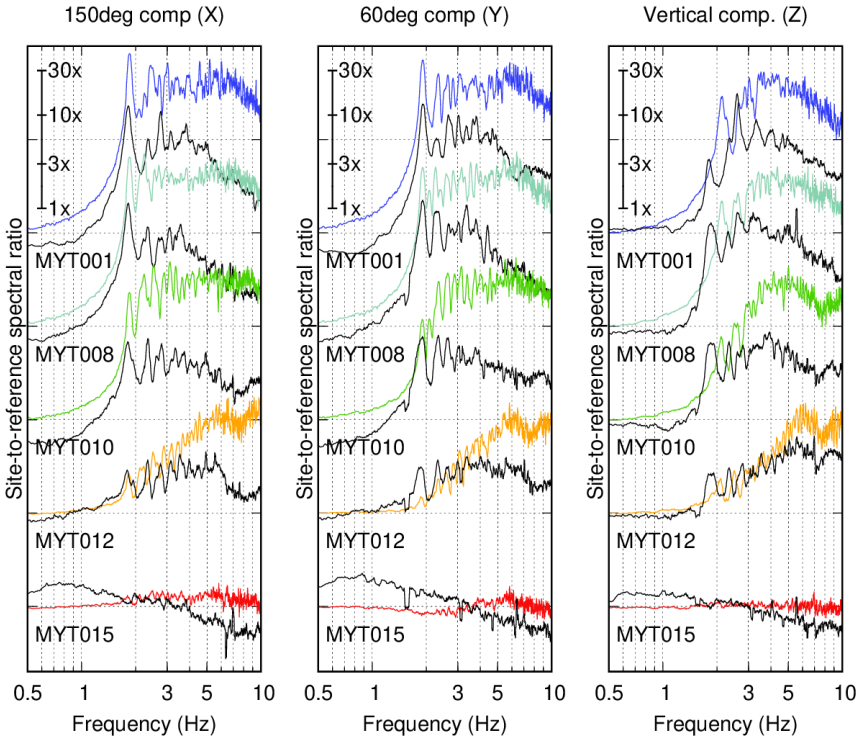
Model 5



Model 6



Model 7



Supplementary Figure 2.2 Model 8. Simulated and observed site-to-reference spectral ratios for models 1-8

3 Ambient Vibrations of a Deep Maar Resonator

This chapter was published as Labuta et al. (2025) in Soil Dynamics and Earthquake Engineering.

3.1 Introduction

Maar is a volcanic structure with a low-relief crater which was created by phreatomagmatic eruption. The top of the maar diatreme, typically several hundred meters in diameter, is filled with post-eruptive sediments, often a lacustrine type overlaying upper bedded and lower unbedded breccia layers. In the middle of the diatreme, there is a remnant of a feeding lava channel filled with pyroclastic deposits. Country rock breccia and megablocks are often scattered at the boundary of the diatreme cone and country bedrock. Magma propagates through a feeder dyke which forms the bottom tip of the diatreme, and, in case of felsic maars, it can propagate to the surface while pushing out magmatic rocks to form lava domes along the crater edge (Ross et al., 2017). Although maar diatremes are classified together with scoria cones as small, monogenetic volcanic structures (Ross et al., 2017), they still possess both syn- and posteruptive hazards. Posteruptive hazards include erosion and lahars, syneruptive hazards represent for example earthquakes, eruption clouds, tephra falls, volcanic bombs, gasses, etc. (Lorenz, 2007). Uneroded diatreme infills of past eruptions might be hidden in the terrain due to the crater's low relief. They contain unique information on past volcanic activity for a given region additionally, lacustrine sediments can also carry information on climate history (Macrì et al. 2023, and references therein). Moreover, maar diatremes can be a supply of natural resources, i.e., precious ores like gold in felsic maars in Mexico, or kimberlites in mafic maars in south Africa (White & Ross, 2011). Geophysical characterization of the diatreme structure is difficult, due to the geometry because the typical depth of the diatreme is larger than the lateral dimension.

In this study we focus on analyzing the maar diatreme ambient vibrations, which can be complementary to classical geophysical methods (for example, gravimetry, or electrical resistivity tomography). As a case study we selected a well-documented (Flechsig et al., 2015; Labuta et al., 2023; Lied et al., 2020; Mrlina et al., 2009) Mýtina maar in West Bohemia, Czechia, see Figure 3.1). The previous research done by Flechsig et al. (2015), Labuta et al. (2023), Lied et al. (2020), and Mrlina et al. (2007, 2009) includes borehole drilling a core logging at the center of the maar depression, gravimetric and magnetometric survey (Flechsig et al., 2015; Mrlina et al., 2009), electric resistivity tomography, shallow seismic refraction tomography, laboratory gamma spectrometry (Flechsig et al., 2015), optical and scanning electron microscopy with chemical analysis and rock magnetic analysis of volcanic bombs to determine cooling rates of pyroclastic deposits (Lied et al., 2020), and finally ambient seismic noise survey with numerical modelling (Labuta et al., 2023). The results of gravimetric and magnetic surveys denoted lateral dimensions of the maar volcanic deposits, mapped the border of lacustrine

sediments and relicts of tephra rim outside of the crater. Mrlina et al. (2009) also proposed shallow geophysical model of the maar based on magnetic and gravimetric survey and borehole drilling. Labuta et al. (2023) continued with the investigation of maar properties, determining depth of pyroclastic rocks up to depth of 800 m from numerical modelling of maar's seismic response.

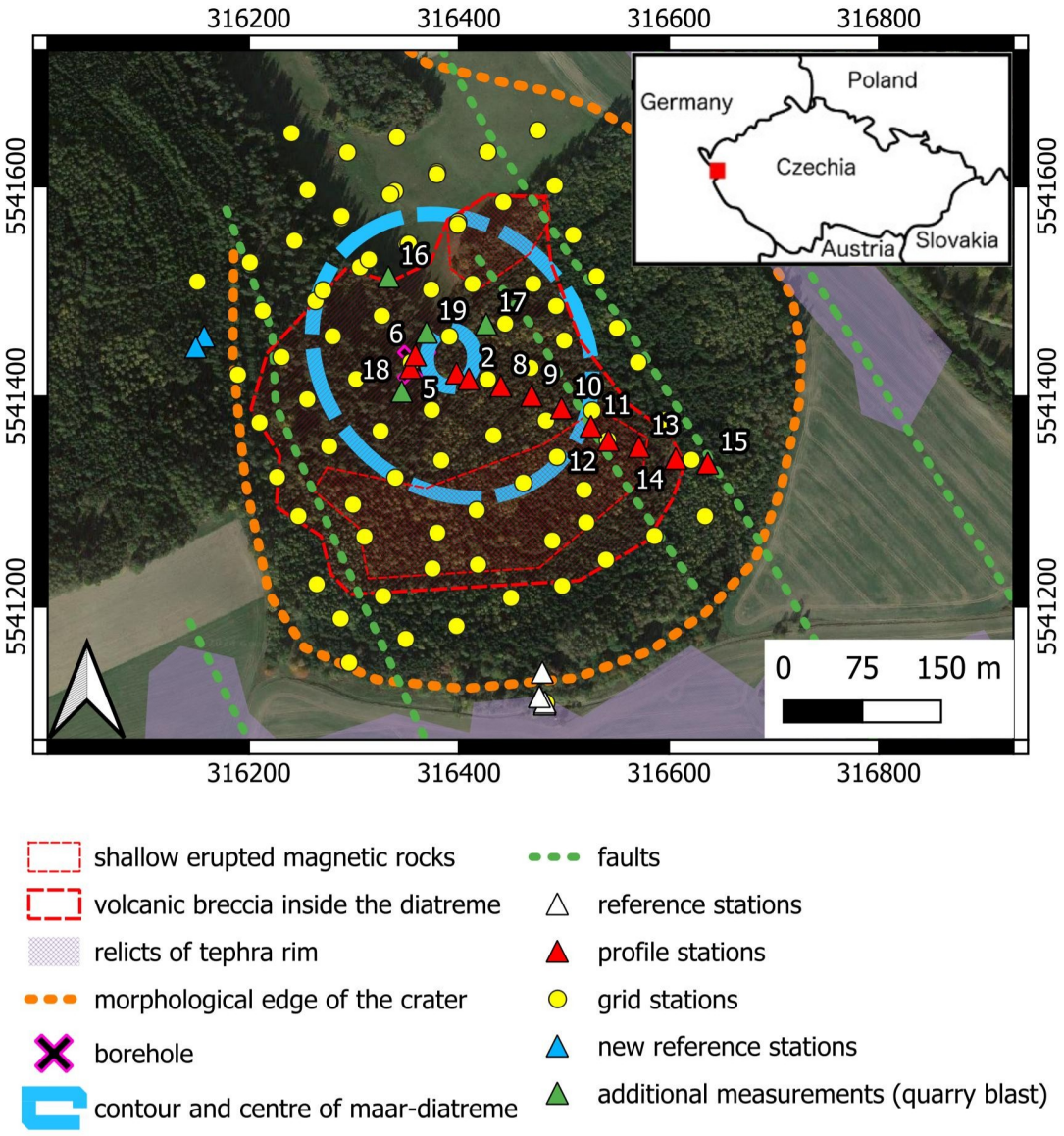


Figure 3.1 A schematic aerial view of Mýtina maar features modified after Mrlina et al. (2009) and conducted seismic measurements in this study. Reference stations for all measurements are represented by white triangles and noted as ref site 1, profile sensors are red triangles, stations used for recording the quarry blast are pink triangles, and the survey grid is represented by yellow dots with its new reference stations shown as blue triangles and noted as ref site 2. The yellow italic numbers left and right of the grid denote the individual lines of stations. The mapped faults (green dashed line) belong to the Tachov Fault Zone (Flechsig et al., 2015). The coordinates are in meters of WGS84 UTM projection in the 33N zone.

3.2 Geological setting

The Mýtina maar is located 10 km SE from Cheb at the Czech/German border close to the southern edge of the Cheb basin (Flechsig et al., 2015). The Cheb basin lies in the western part of Bohemian Massif, overlaying the westernmost part of the Eger Rift zone and it is filled with Tertiary and Quaternary sediments (Kopecký, 1978). The bedrock surrounding the Mýtina maar consists of Upper Cambrian to Ordovician muscovite–biotite mica schists formed during the Variscian orogeny event in the Saxothuringian zone (Vejnar, 2004). The broader area around the Cheb basin is also geologically characterized by granites – to the east Karlovy Vary and Zandov plutons, to the east Mitterteich and Flossenbürg Granites (Fiala & Vejnar, 1997; Richter & Stettner, 1993; Vejnar, 2004). The Cenozoic alkaline volcanic activity in West Bohemia is connected to the triple junction of the WSW–ENE oriented intra-plate Eger Rift zone, the NNW–SSE-oriented Cheb–Domažlice Graben and the N-S leading Regensburg–Leipzig–Rostock fault zone (Bankwitz et al., 2003). The Eger Rift started to evolve in Late Eocene and its development can divided according to Kämpf et al. (2005) into three steps: (1) Early Oligocene–Early Miocene (31–20 Ma); (2) Middle to Late Miocene (16.5–8.3 Ma) and finally (3) Middle Pleistocene (0.7–0.3 Ma). At the end of the last period, the Mýtina maar was formed (age: 0.29 Ma, Mrlina et al. 2007) on the NNW–SSE-oriented Tachov fault zone together with the scoria cone volcano Železná hůrka (Mrlina et al., 2009), which is located about 750 m SSE from the center of the maar depression.

3.3 Methods used to process ambient seismic noise

The ambient seismic noise approach is an effective method to survey geological structures in seismically less active or even inactivate setting, such as no earthquake occurrence, but it is unable to process explosions or to employ other artificial seismic sources. It utilizes all ambient seismic noise generated by man-made activity at frequencies higher than 1 Hz, which is subject to daily and weekly variations, and microseisms at lower frequencies between 0.005 and 0.3 Hz (Bonnefoy-Claudet et al., 2006).

3.3.1 Site-to-reference spectral ratio (SRSR)

To estimate the frequency-dependent amplification of ground motions in the maar, we have used the SRSR method applied on ambient seismic noise. The SRSR was originally used to analyze earthquake recordings (Borcherdt, 1970), later it was integrated into ambient noise analysis (Irikura & Kawanaka, 1980; Kleinbrod et al., 2017; Pischiutta et al., 2017). For this method, at least two simultaneously recording seismic stations are necessary. Let a single reference station be placed on an outcropping bedrock as near to the studied area as possible and let a field station (or stations) be placed inside the studied area. Then the reference-field stations pair layout allows us to obtain an estimate of the relative wave-field amplification between them. The Multitaper Fourier Spectra (MFS,

Prieto et al. 2009) of each component of field station is divided by the respective component of MFS of reference station recording. The resulting ratio is the estimate of the frequency-dependent amplification. The main assumption of the method is that the noise sources are far from the studied area, as in case of a distant earthquake, to assume the source and path effects are the same for field and reference stations and thus are eliminated in the field/reference MFS ratio. This method is therefore applicable for surveying areas far from seismic noise sources whether man-made or natural.

3.3.2 Frequency domain decomposition (FDD)

Frequency domain decomposition (FDD) was used for example by Bottelin et al. (2013) for unstable rock columns, Moore et al. (2019) for freestanding rock towers, large-scale mountain landforms Weber et al. (2022), or by Häusler et al. (2019, 2021) for rock slope instabilities. Although this method is typically applied to array measurements synchronized in time, it can be also applied to a single station measurement, effectively becoming equivalent to polarization analysis. In particular, the eigenvector of the cross-power spectral density matrix constructed for a single station measurement, associated with the largest eigenvalue, points in the direction of the largest amount of polarization (Burjánek et al., 2010).The FDD is based on estimation of cross-power spectral density matrix, which consists of complex-valued cross-power spectral densities calculated between all seismogram traces for a given frequency. The eigenvalues of this frequency-dependent matrix represent the auto spectral densities, and the largest eigenvalue has peaks at the natural frequencies of a local structure. The corresponding complex eigenvectors contain 3D modal vectors, which describe the particle motion of the mode across the studied site, including the relative phase shifts (see, e.g., Brincker and Ventura 2015; Poggi and Fäh 2010).

3.3.3 Time frequency polarization analysis (TFPA)

The TPFA of ambient seismic noise is used to characterize particle motion at a single seismic station. The method was introduced in the time domain by Vidale (1986) and extended to the time frequency domain by Burjánek et al. (2010). The particle motion is characterized by three frequency-dependent parameters: strike, dip and ellipticity and it is generally elliptical for a short recording (in hours) of seismic noise, which is assumed to be quasi-stationary (i.e., seismic noise sources are stationary in time). The strike represents orientation of the semi-major axis of the elliptical motion, dip describes how much tilted is the semi-major axis from horizontal plane. Ellipticity is computed as a ratio between the semi-minor and semi-major axes. The frequency resolution of the TFPA is controlled by the parameter , which represents the effective duration of the mother Morlet wavelet in terms of periods. For instance, if $\omega_0 = 6$, then the wavelet lasts for approximately 6 oscillations. A detailed description of the method can be found in Burjánek et al. (2010, 2012)

3.3.4 Horizontal-to-vertical spectral ratio (HVSR)

The Horizontal-to-vertical spectral ratio method was introduced by Nogoshi (1971) and popularized by Nakamura and Samizo (1989), Nakamura (1996), and Nakamura et al. (2000)) (therefore also called Nakamura's technique - Mucciarelli and Gallipoli 2001). Three component seismograms of single station are transformed from time domain into frequency domain and spectral ratios between the vertical and each horizontal component are computed. The spectral ratio peak (if any) represents a resonant frequency of S-waves (Bonnefoy-Claudet et al., 2006; Konno & Ohmachi, 1998), therefore this method is generally used to estimate the fundamental resonance frequency of the studied area.

3.3.5 Numerical modelling

To compute synthetic seismograms, we used the code SW4 developed by N. A. Petersson and Sjögreen (2015) and Sjögreen and Petersson (2012), which is a fourth-order finite difference solver of the visco-elastodynamic equation in Cartesian coordinates. We first computed Green's functions using the reciprocity theorem (e.g., Eisner and Clayton (2001)) by exchanging the positions of the modelled stations with the positions of seismic sources, which were uniformly distributed on the grid outside of the studied site. The Green's functions were then convolved with randomly generated source time functions to produce the required seismic noise seismogram of adequate duration (Burjánek et al., 2019). The geometric model of the maar structure was chosen as an elliptical cone, featuring a shallow sedimentary basin (depth up to 80 meters) and a transition zone layer of outer breccia covering the inner volcanoclastic rocks (according to Mrlina et al. 2007). The model consists of seismic velocities Vp and Vs, density rho, and attenuation factors Qp and Qs, with a selected total depth of 800 meters. The model was used to generate synthetic ambient vibrations which are compared with the recorded ones. This model showed the best misfit of fundamental modes' amplification frequency and ratio between the observed and recorded data (Labuta et al., 2023). Other 8 tested models comprised of cones with tested depths of 150, 300 and 800 m with diameter of either 200 or 300 m, or elliptical cylinders with depths reaching 800 or 2000 m. The models were tested by trial – error method in which we tried to compare the results for the SRSR, not for the HVSR. For more details on the model and numerical modeling, see Labuta et al. (2023).

3.4 Field experiments

The ambient seismic noise measurement was carried out using Lennartz LE-3Dlite MKIII 3 component seismometers with 1 Hz corner frequency in the initial phase of surveying the profile. The grid survey was conducted using the FairField Zland Node 5 Hz seismometers. We consistently utilized the same receiver type for both the bedrock reference and the field stations to mitigate potential errors in the sensor sampling frequency and gain. All measured points were located using differential GPS apparatus with 1 cm precision.

The location of the reference station was chosen based on gravimetrical survey results by Mrlina et al. (2009) and shallow seismic sensing by Flechsig et al. (2015),

south of the crater outline, Figure 3.1 The reference station was positioned in a shallow hole (ca 50 x 50 x 50 cm) to prevent it from being placed on top of shallow tree roots, as the location is at the forest edge. To validate the reliability of the reference station, an HVSR analysis was performed for its ambient noise recording: no significant HVSR peak (Figure S3.8) or predominant directionality from polarization analysis (Figure S3.7a) was observed in the studied frequency band (0.5-10 Hz). Selection of the position for the reference station does not significantly change the SRSR results, the resonance frequency of each mode remains the same, only the relative amplification factor is slightly affected.

The survey was carried out in three distinct phases. The initial phase involved a basic characterization of the maar's response through profile measurement extending from the center of the maar depression, denoted as MY-1 borehole (Mrlina et al., 2009), to the south-east edge of the crater. A station spacing of approximately 50 m was utilized, employing a total of 15 sensors (red triangles in Figure 3.1), with a recording duration of 2 hours of ambient seismic noise. Due to the limited number of seismic stations the points were measured in sequence (point by point), which means performing the FDD analysis at these points is not feasible. Merging the eigen vectors for the non-simultaneous recordings is not possible, when a common measurement point in the resonating body is not available (Brincker & Ventura, 2015).Merging such eigenvectors obtained from different datasets requires normalizing their lengths and synchronizing their phase requiring a common measurement point per pair of datasets, ideally close to an antinode of the given mode (ie., where the motion of the mode is strong). This common measurement point represents a common component in the eigenvectors, which can be used for the re-scaling of the entire eigenvector, assuming that phase and amplitude of the modal motion at this point is stationary. The reference station on the bedrock cannot be used for such purposes, as the resonance is not developed there.

Following that, during the second-phase survey, we deployed 3 profiles, aiming from the borehole towards azimuths of 80, 200 and 320 degrees. Each profile consisted of 4 stations with spacing similar to that of the profile section (green triangles in Figure S3.1). All the stations were situated in shallow holes like the one at the reference station. The aim of the second survey was to densify the observations beyond the first profile and test the possibility to retrieve surface waves' dispersion curves from ambient vibrations. By chance, a quarry blast was recorded during this measurement a with good signal to noise ratio, which provided an opportunity to show the resonance phenomena in the time domain.Finally, we covered a dense rectangular grid of 8 points per line by 9 lines with spacing of 50 meters between points and lines (yellow dots in Figure 3.1). With only 24 seismometers available, we initially measured profile lines 1, 4, and 7 overnight. During this survey, we managed to record the ML 3.9 earthquake located in Germany. Subsequently, we shifted these three lines by one line to 2, 5, and 8, and then once more to 3, 6 and 9. to achieve complete coverage of the grid rectangle. The lines 2, 5, 8 and 3, 6, 9 were recording only for 1 hour the following day after the lines 1, 4, 7. During these short-term surveys, one buried station close to the borehole and another at the reference point were recording continuously for one month. This one station in the center allowed us to connect the results of FDD analysis of these three (1, 4, 7; 2, 5, 8 and 3, 6, 9) stages of the survey. Hence the

reference point was the same for all of the measurements. Refer to the electronic supplement for a detailed annotated map (Figure S3.1).

3.5 Results

Initially, we processed the recorded ambient vibrations using the TPFA to obtain significant directions of particle motion over the studied frequency band up to 10 Hz. In order to get high spectral resolution for the TPFA, the ω_0 parameter of the mother Morlet wavelet was set to 96 Hz. Inside the maar, both profile and grid surveys exhibit two distinct TPFA peaks at 1.8 Hz and 1.9 Hz with ellipticity close to zero (Figure S3.7c), while no such peaks are observed outside the maar, such as at the reference stations (Fig S3.7a-b). This is manifested by nearly linear particle-motion azimuths of 150 and 60 degrees for 1.8 Hz and 1.9 Hz modes, respectively, for stations in the center of the maar. For stations closer to the maar borders, the azimuths for both modes deviate from the two dominant directions and are even close with directions facing towards the center of the maar. Additional details of the analysis are presented in the electronic supplement (Figure S3.2).

Before assessing the Site-to-reference spectral ratios (SRSR, i.e., relative amplification with respect to the reference station), the recordings were, for each station individually, rotated along the vertical axis into the two dominant ground-motion directions – first into the direction of mode 1 (Figure S3.2a), following by rotation into the direction of mode 2 (Figure S3.2b), previously identified by TFPA for each station. Subsequently, the rotated particle motions were processed by SRSR using sliding time window of 50 s between 0.5 and 10 Hz. The average SRSR for the MYT001-015 profile, as shown in Figure 3.2a-c, exhibits clear peaks at frequencies 1.83 Hz; 1.91 Hz; and 2.34 Hz on both, horizontal and vertical components. The resonant frequencies are the same for all stations within the maar sediments. In contrast, stations MYT014 and MYT015, located just outside of the maar sediments (as mapped by Mrlina et al. (2009)) do not show any peak at frequencies 1.83 and 1.91 Hz. The maximum SRSR reaches up to 30 at horizontal components and 25 at vertical component in the central area of the maar close to the borehole (see Figure 3.2), while the relative amplification is negligible (approaching 1) below 1 Hz. Overall, the spectral amplification gradually decreases from the center of the maar, near the borehole, to its outer edge, as evidenced by the diminishing spectral ratios. Spatial oscillatory-mode character of the maar (Figure 3.2a-b) is depicted by peak SRSR values evaluated within narrow frequency bands ranging from 1.8 to 1.85 Hz and 1.88 to 1.93 Hz, centered around main resonant frequencies of 1.83 and 1.91 Hz, respectively. The profile and grid station SRSR peaks were interpolated using the QGIS TIN interpolation method, which involves Delaunay triangulation of the nearest three points followed by bilinear interpolation within these triangles. However, certain stations (MYF107, MYF116, MYF122, MYF164, MYF165, MYF167, MYF170) were excluded from this interpolation due to high amplification ratio values below 1 Hz, likely caused by faulty installation such as poor coupling with the ground or interference with grass.

A comprehensive analysis of reference stations revealed a slight local effect between 1 and 10 Hz, leading to a reduction in the SRSR amplification ratio by an

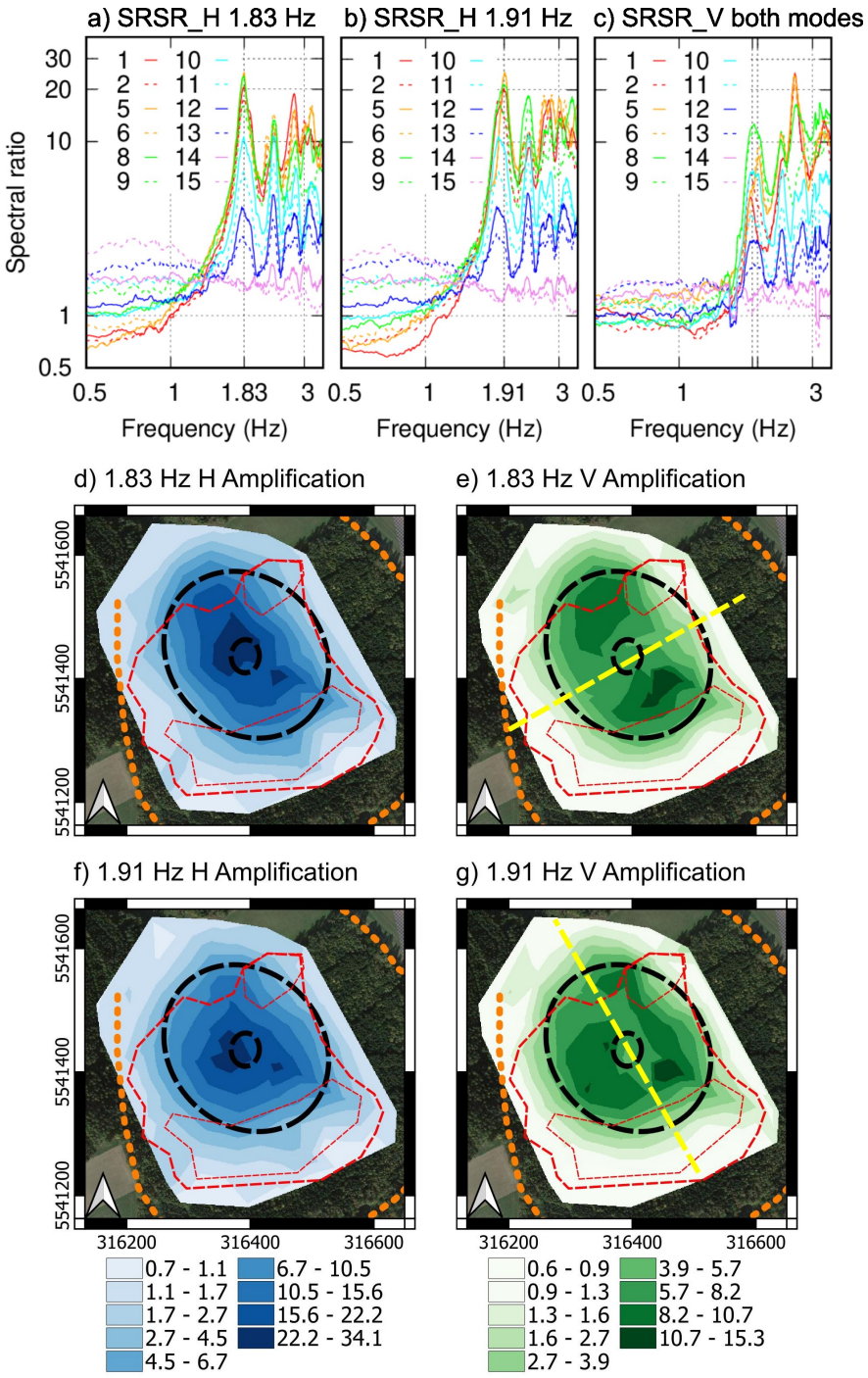


Figure 3.2 Maar SRSR amplification a) horizontal component for mode 1 (1.83 Hz), b) horizontal component for mode 2 (1.91 Hz), c) vertical component. Oscillatory modes 1 and 2 corresponding to SRSR amplification peaks: mode 1 amplification values at 1.83 Hz for horizontal (d), and vertical (e) component; mode 2 amplification values at 1.91 Hz for horizontal (f) and vertical (g) component. The blue and green color scales correspond to SRSR amplification for horizontal and vertical components respectively. The yellow dashed line represents symmetry in vertical ground motions, while the red and orange lines delineate the morphological surface limits, as shown in Figure3.1.

average factor of 0.8. Consequently, the resulting spectra of the profile stations are adjusted using SRSR of the old to new reference station (Kleinbrod et al.,

2019).

Frequency domain decomposition (FDD) was exclusively applied to the grid measurement recordings, segmented into three datasets due to the measurement's three-step process. The cross power spectral density matrix is Hermitian of real positive eigenvalues and generally complex eigenvectors with arbitrary lengths and phases. Merging such eigenvectors obtained from different datasets requires normalizing their lengths and synchronizing their phase requiring a common measurement point per pair of datasets, ideally close to an antinode of the given mode. The first 18 eigenvalues for one of the datasets are depicted in Figure 3.3a. The initial four peaks of the maximum eigenvalue (1.81 Hz, 1.92 Hz, 2.23 Hz, 2.34 Hz) align with the resonant frequencies derived from polarization and SRSR analysis, but they differ by 0.1 – 0.2 Hz for the first two mode. This can be caused by different length of time window used to calculate the frequency spectra for both methods and it can widen or sharpen the peak Corresponding eigenvectors (depicting particle motions of the modal motion) for the first three peaks are shown in Figure 3.3b-c. Specifically, the real part of the eigenvector illustrates the phase development (0, 2π). If the components are in-phase at a single station, then the motion is linear. The modal motion directions for the first two modes align with the dominant directions identified by TFPA. The motions of the first two modes resemble a pool seiche, while the third mode represents a torsional mode. The fourth mode shape (Figure S3.3) can be found in the electronic supplement. The observed spectral densities in a frequency band 1.5 – 2.5 Hz can be well reproduced by a sum of impulse responses of four single-degree-of-freedom (SDOF) oscillators with natural frequencies f_1 - f_4 (1.81, 1.92, 2.23, and 2.34 Hz, respectively) and damping ratios ζ_1 - ζ_4 (2.3, 2.0, 0.8 and 1.7 %, respectively), as shown by the color solid line in Fig 3.3a. Such modal parameters could be used as a constraint in a numerical modal analysis.

We have also recorded a distant earthquake with epicenter in SW Germany, ML 3.9, at an epicentral distance of 310 km, and a quarry blast 17 km away at the Hirschentanz mine (Germany)during the second phase of the survey. When SRSR of these events is compared with the results from ambient noise measurement, we observe a similarity between the amplification ratios in a frequency band 0.5 - 3 Hz, including the similar amplification of the four modes (Figure 3.4). The velocity recordings in the time domain from the quarry blast are shown in Figure 3.5. The recordings were rotated in horizontal plane in the two dominant directions (150° and 60°) and filtered using raised-cosine in a narrow frequency band 1.5 - 2.15 Hz ¬¬in order to extract the motion of the first two closely spaced modes. A strong amplification and prolonged duration of ground motion within the maar sediments is clearly visible. The peak ratio with respect to the reference station reaches 20 for the horizontal component and 17 for the vertical component. The duration of ground motion is prolonged from seconds to tens of seconds at all stations compared to the reference station. The filtered recordings indicate a possible coupling between the first two modes. Since the motions of the two modes are almost perpendicular at stations MYT17-19 and MYT006, they are well separated for the two directions of 150° and 60°. That is, mode 1 dominates in Figure 3.5a and mode 2 dominates in Figure 3.5b for those stations. Mode 1 clearly advances mode 2, which emerges when the mode 1 just reaches its maximum (Figure 3.5). The apparent (anti-)correlation between horizontal and vertical components agrees

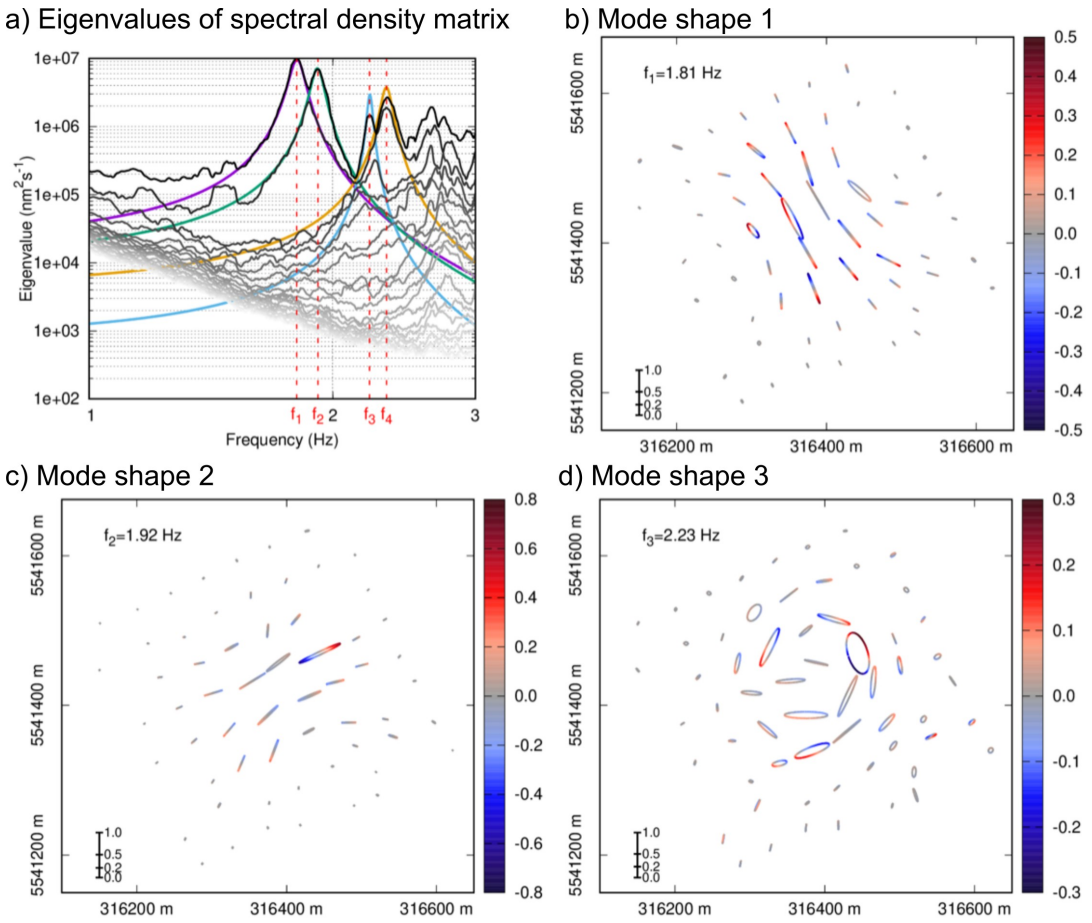


Figure 3.3 Results of the FDD modal analysis. a) 18 largest frequency-dependent eigenvalues (in grey scale) of cross-spectral density matrix for the grid survey identifying four modal frequencies f1 - f4 (1.81, 1.92, 2.23, and 2.34 Hz, respectively), with solid color lines represent the best fitting SDOF oscillator for each of the four modes. b) Particle motion of mode 1. c) Particle motion of mode 2. d) Particle motion of mode 3. In b, c, and d, the scale in the southwest indicates the dimensionless horizontal amplitude of mode particle motion, while the color scale depicts the dimensionless vertical amplitude of mode particle motion.

with the mode shapes retrieved by FDD (Figure 3.5). In contrast, the two modes are parallel at station MYT016, both oriented approximately to 150°, and their mixture dominates in Fig 3.5a.

3.6 Discussion

Our study demonstrates that ground motions of the Mýtina maar are primarily driven by normal mode motion. Seismic waves become trapped in the crater infills, leading to complex three-dimensional resonance through constructive interference. While conventional models for one-dimensional stratified media suffice for describing fundamental resonance frequencies and amplification levels over bedrock half-space, they fall short for the maar. The crater's geometry is essential and cannot be overlooked or reduced to a simplistic two-dimensional cross-section, as commonly done for deep elongated valleys (e.g., Ermert et al. 2014).

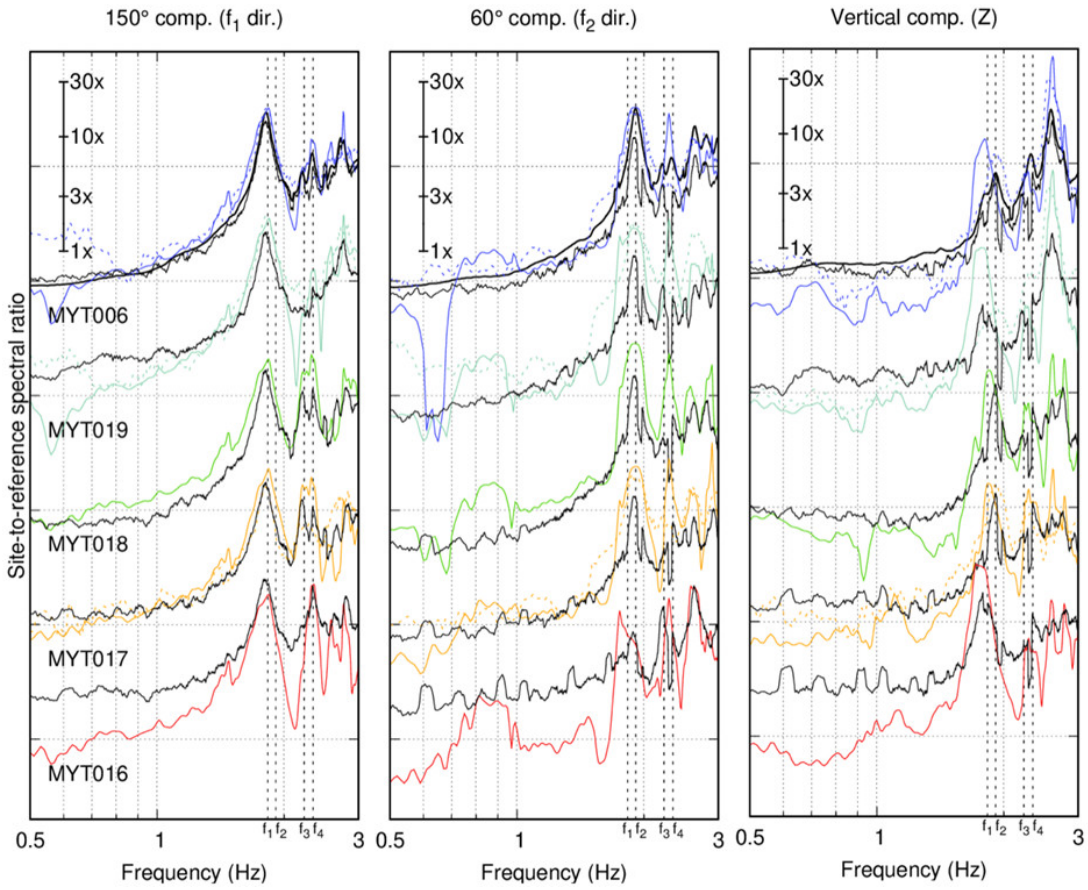


Figure 3.4 Comparison of SRSR for ambient noise, earthquake, and quarry blast recordings. The quarry blast is noted by the solid color line (Hirschentanz mine 17 km to the west from Mýtina, on 04-03-2020), the earthquake of ML 3.9 of 16-10-2022 04:13:19 GMT which occurred in Germany (ISC event ID 624909538, epicentral distance 310 km) is noted by the dashed color line; the black hairline represents one hour of seismic noise measurement, and the bold black line at station MYT006 is the mean of one-hour measurements continuously acquired for one month.

We clearly identified four oscillatory modes represented by the first four resonant frequencies from SRSR across the stations within the maar infills. These resonant frequencies remain consistent throughout the entire infill, encompassing both sedimentary rocks and the breccia outer rim. Corresponding maximum amplification values on both horizontal and vertical components are concentrated at the center of a morphological depression, gradually decreasing in all directions towards the edge. Halfway to the crater's morphological edge (Figure 3.2d-g), amplification ceases, marking the transition from anticipated breccia infill to country bedrock. These characteristics are typical for normal mode vibration of sedimentary basins, attributed to standing waves within the infills embodied in the bedrock. Modal analysis further confirms this, uncovering in-phase motion across the stations.

The resonant frequencies of the first two modes, 1.83 and 1.91 Hz, are very close yet distinctly separated (Figs. 3.2 and 3.3a), as the two modes are horizontally perpendicular to each other at the center of the maar (Figure 3.3b and c). In other words, a correct rotation around the vertical axis achieves perfect mode

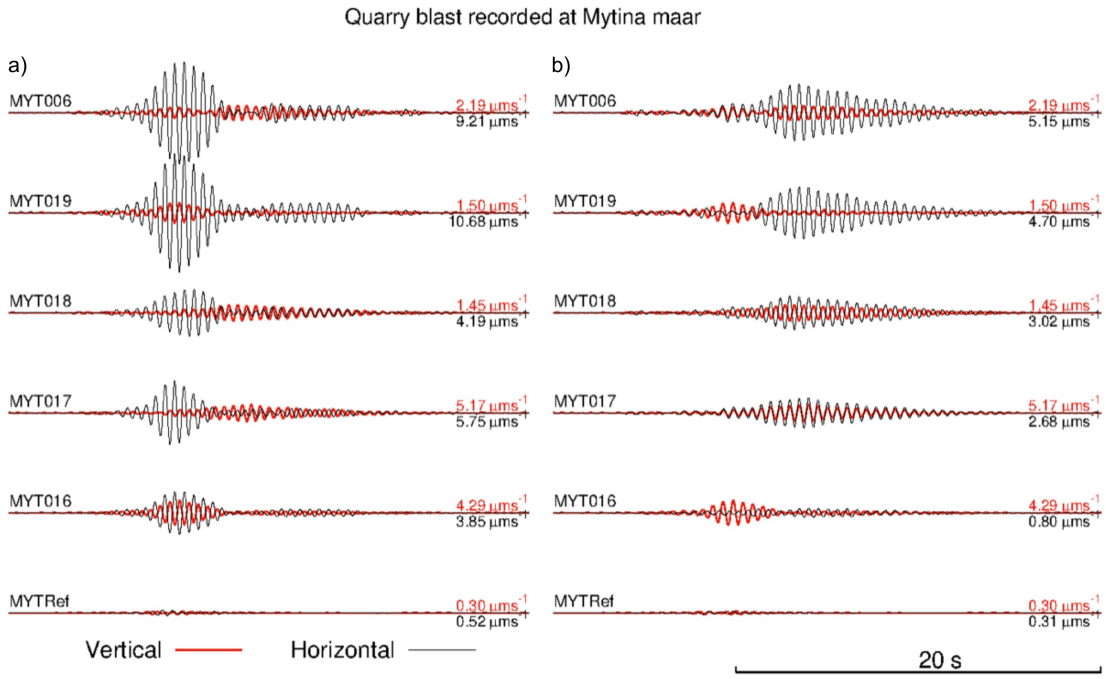


Figure 3.5 Quarry blast recorded at the Mýtina maar. All recorded velocity seismograms are band-passed between 1.5 and 2.15 Hz. a) Vertical (red) and horizontal (black) components rotated to the azimuth of 150 degrees clockwise from the north. b) Vertical (red) and horizontal (black) components rotated to the azimuth of 60 degrees clockwise from the north.

separation there. In contrast, at the breccia border the two modes are not perpendicular and occasionally run nearly parallel to each other. Both modes exhibit a significant vertical component, leading to broad SRSR peak across both frequencies for the vertical component (Figure 3.2c). The proximity in frequency between the two modes may indicate a single mode that has split into two due to broken crater symmetry. For instance, the crater's slight deviation from perfect circularity, potentially forming a slightly elliptical structure, could explain the proximity modes, as demonstrated by numerical modelling(Labuta et al., 2023). The elliptical structure's major semiaxis shares an approximate same azimuth (150 degrees clockwise from north) within Tachov Fault Zone (TFZ, Figure 3.1), indicating that both the morphological crater and maar infill are elongated along it, similarly to the elongation of SRSR amplification for both split modes and the orientation of ground motion resulting from modal analysis for the 1.83 Hz mode. While TFZ likely played a significant role in the formation of the maar, shaping its elliptical geometry, it does not directly influence the orientation of ground motion or the elongation of SRSR amplification. These are both driven by the geometry of sediments and breccia fills. For stations along the TFZ, which are outside of the crater, we did not observe any strong significant amplification or prevalent directions.

The symmetries in vertical ground motions delineated in Figure 3.2 d-g are further supported by the results of the modal analysis for all 4 identified modes. Especially the changes of polarity of vertical movement across the axis of the maar. These symmetries in the mode shapes reflect deeper symmetries of the maar infills within the elliptical crater. The symmetries of the higher modes (3.

and 4.) indicates the possible lateral symmetry of the maar structure at least near the surface.

The amplification at resonant frequencies serves to delineate the boundary between the breccia infill and bedrock. For example, stations 13 a 14, just 35 meters apart exhibit moderate amplification at station 13 and none at 14. This indicates that station 14 lies beyond the resonating mass, pinpointing the boundary between them. This is in contrast to findings in Mrlina et al. (2009), where the gravimetric anomaly fails to provide a clear boundary, necessitating a gravimetric inversion to specify it. While the magnetic anomaly aligns with the south-east part of the maar infill, ground motion amplification in the north-west extends beyond that of the magnetic anomaly. This might be an effect of the stream originating from the center of the crater and flowing to the northwest, eroding away the crater and carrying the maar sediments out. The resonant motion of the maar infills is partially transmitted into those alluvial sediments even beyond the former crater limits. Therefore, it is difficult to map an exact boundary in this area with the ground motion amplification only.

The frequencies of fundamental modes 1 and 2 are relatively low (1.83 Hz / 1.91 Hz, respectively), which indicates a deeper structure (at least several tenths of meters) considering typical site conditions (e.g., Hobiger et al. 2021). In comparison, for example Ermert et al., 2014 report frequencies of 0.3 Hz and depth of 900 meters for the Rhone valley in south-west Switzerland. The main difference is in the geometry, while the Rhone valley is an elongated 2-D structure approximately 2.5 km wide and tens of kilometers in length, the Mýtina maar infill is approximately 360 x 400 meters wide and at least 800 meters deep (Labuta et al., 2023).

All four resonance modes, clearly identified in the wave field, exhibit strong vertical components with amplitudes comparable to horizontal ones (Figure 3.2). This poses a challenge for widely used HVSR method, which may not be suitable for detecting and characterizing such resonances. Figure 3.6. presents a comparison of observed and simulated HVSR. While higher HVSRs are still observed at the center of the maar, with a peak corresponding to the fundamental frequency, the significant HVSR peak diminishes after approximately 50 m outward from the center. For instance, stations 8 and 10 exhibit broad, low-amplitude peaks in HVSR (lower than 3; Figure 3.6a), while the corresponding SRSR (Fig 3.2) shows sharp peaks referring to relative amplifications greater than 10. HVSR for station 12 is even flat. This trend is well captured by the HVSR from the simulated ambient vibrations, despite the coupling between the horizontal and vertical components is not being so well replicated in the numerical simulations.

The SRSR method assumes that the noise sources are distant from the studied structure. However, during one measurement, we encountered a forestry machine working in the wood just at the maar infills, acting as an artificial seismic source. This violated the assumption of distant sources, yet analyzing the biased SRSR remains a valuable exercise. At first, all biased SRSR were close to unity at low frequencies, indicating acceptable quality, since the SRSR quality typically evaluated at low frequencies, where motions should be identical regardless of site conditions. This may be attributed to the limited frequency band of the artificial source (machinery), which does not generate strong low frequency motions. While the frequencies of all four modes are identical, the amplification is significantly

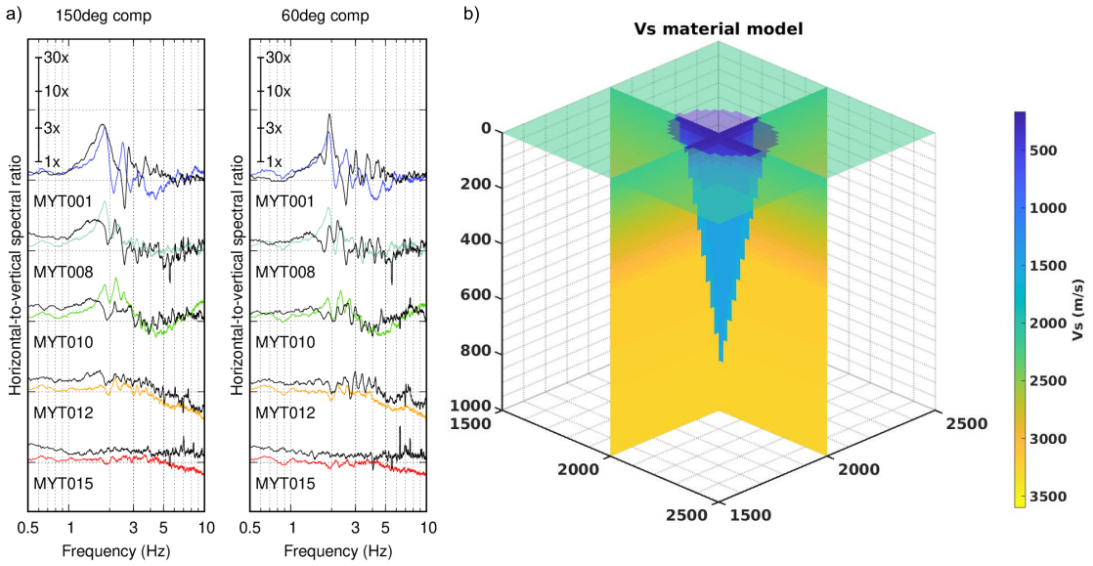


Figure 3.6 a) Simulated and observed HVRS ratios, considering the visco-elastic model (in color) and observed data (in black) for two horizontal components (150 degrees representing mode 1 at 1.83 Hz and 60 degrees – mode 2 at 1.91 Hz). b) Material model illustrating the shear wave velocity (Vs) of Mýtina maar used for computing synthetic seismograms in finite-difference modelling (by Labuta et al. 2023).

higher for biased SRSR (see Figure S3.4 in Supplement material). For example, at station 212, the unbiased SRSR of the vertical component of the first mode was 13, while the biased SRSR was 80, resulting in an apparent amplification approximately 6x stronger with the artificial source in the maar. It is important to recognize this bias in case of maars with any active seismic sources, whether man-made (inhabited areas) or natural (strong water streams, etc.) to avoid unrealistic estimates of amplification levels. However, this bias could be advantageous for detecting weak resonances especially near boundaries of maars.

The results of HVSR from the first profile surveying have shown a significant wide peak in resonance frequency amplification at only the first two modes, near geometrical center of the maar depression. The peak diminishes rapidly further away from the center, attributed to relatively high vertical amplification compared to horizontal components (compare SRSR on Figure 3.2 a, b, c with HVSR on Figure 3.6 a, b, such as station 10 – MYT010). Synthetic HVSR further confirms this observation. The resulting comparison for HVSR for all 9 models for selected stations is presented in Figure S3.5. For the station MYT001 we manage to fit the synthetic HVSR peak with observed data both in frequency and amplification for the visco-elastic model, but stations MYT008 and MYT010 have higher synthetic peak than observed. Stations MYT012 and MYT015 do not have any significant peak at studied frequency band 1.83 – 1.91 Hz, both for observed and synthetic data, however station MYT012 still shows SRSR amplification peak (dark blue solid line in Figure 3.2a - c) in observation.

During the maar survey, we applied multiple seismic methods, including HVSR, SRSR, TPFA and FDD. The primary advantage of HVSR and TPFA is their requirement of only a single seismic station, without the need for a reference station. However, as mentioned above, the HVSR may not perform reliably in the presence of strong vertical resonances and is not recommended for analyzing

maar resonances. On the other hand, TPFA was able to detect at least the first two modes of amplification and determine their direction, even at stations located at the border between the infill and bedrock (for example station 13). In contrast, the SRSR method requires at least a couple of sensors. The main challenge with SRSR is the selection of suitable location for the reference station. However, this is not an issue in the case of a maar structure, as the edge of the crater serves as a reasonable option. Therefore, SRSR is the preferred method for surveying the maar resonances and mapping the maar's boundary. Even a double-station measurement close to a maar's center provides the fundamental frequency and can distinguish deep infills from shallow terrain depressions. To better understand the ground motion, including the relative phase across a larger section or the entire maar, we employ the FDD. For more than one station, FDD provides information about the ground motion of identified modes and their phases. Thanks to FDD, we were also able to describe the third mode as a torsional one. Like HVSR and TFPA, FDD does not require a reference station on a bedrock outcrop outside the structure. Conversely, potential utilization of data at an extensive number of stations placed outside of the studied structure can impede a successful application as these recordings contain uncorrelated motions at the frequency of structure oscillation modes. In principle, it is possible to apply FDD for a single measurement as well, but the result is equivalent to polarization analysis (TFPA).

3.7 Conclusions

We examined seismic noise wavefield in the Mýtina maar volcanic structure. Our measurements indicate that ambient vibrations within maar infill are primarily driven by normal mode motions due to the 3D resonance of the crater infills. These resonances result in a strong ground motion amplification with respect to the bedrock. Remarkably, at the center of the crater, we observed amplification factors of 30 on the horizontal component and 15 on the vertical component, challenging the conventional belief that local site effects predominantly affect horizontal components. Consequently, the widely used H/V method proves unsuitable for investigating such sites, a conclusion further supported by our numerical model. Furthermore, we found that amplification factors estimated from ambient noise recordings hold ground motion predictive value only when the noise sources are located outside of the infills. Conversely, the presence of a seismic source within the infills, such as in inhabited craters, causes overestimation of amplification factors. Recent measurements at other maar volcanic structures within the Bohemian Massif suggest that these observations are not isolated incidents and justify the need for further exploration, which we intend to pursue in future studies.

Additionally, our ambient vibration data allow for precise mapping of the borders of the maar volcanic infills. This methodology offers simplicity and removes the requirement to solve inverse problems. Although the results presented in this study were obtained by very dense seismic deployment, basic characterization of such volcanic geological structure can be achieved simply by conducting double station noise measurements (point-by-point). Moreover, the observed amplification significantly increases seismic hazard and risk especially in inhabited maars (for example, like those in the Eifel region Dahm et al. 2020 in Germany). The strong

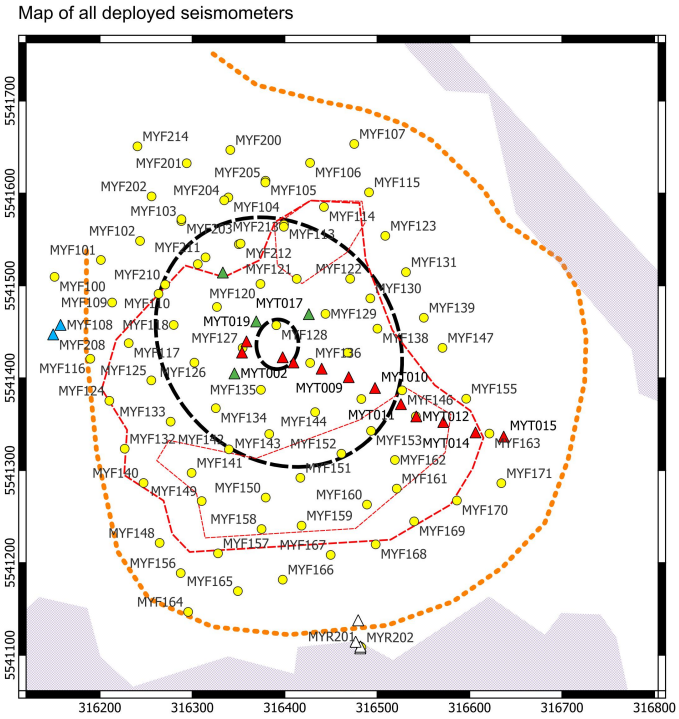
amplification and related increased duration of ground motions might result in increased risk of liquefaction in water-saturated maar sediments.

The observed coupling of the vertical and horizontal components, as well as the potential coupling of the two first modes, is not adequately captured by our numerical model. Therefore, further numerical studies are required.

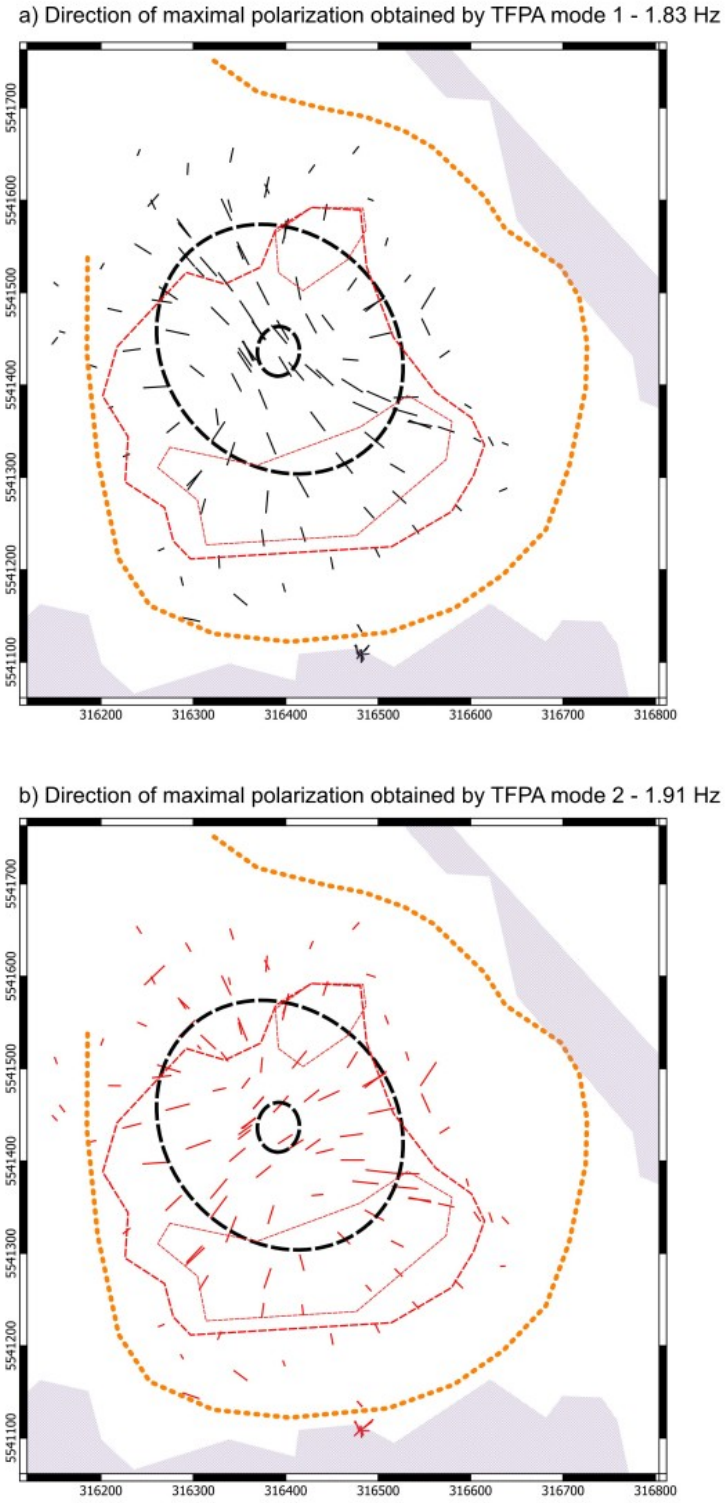
3.8 Acknowledgements

This work was supported by Czech Science Foundation (GACR), project no. GA20-15818S, and by the Ministry of Education, Youth and Sports of the Czech Republic through the e-INFRA CZ (ID:90254).

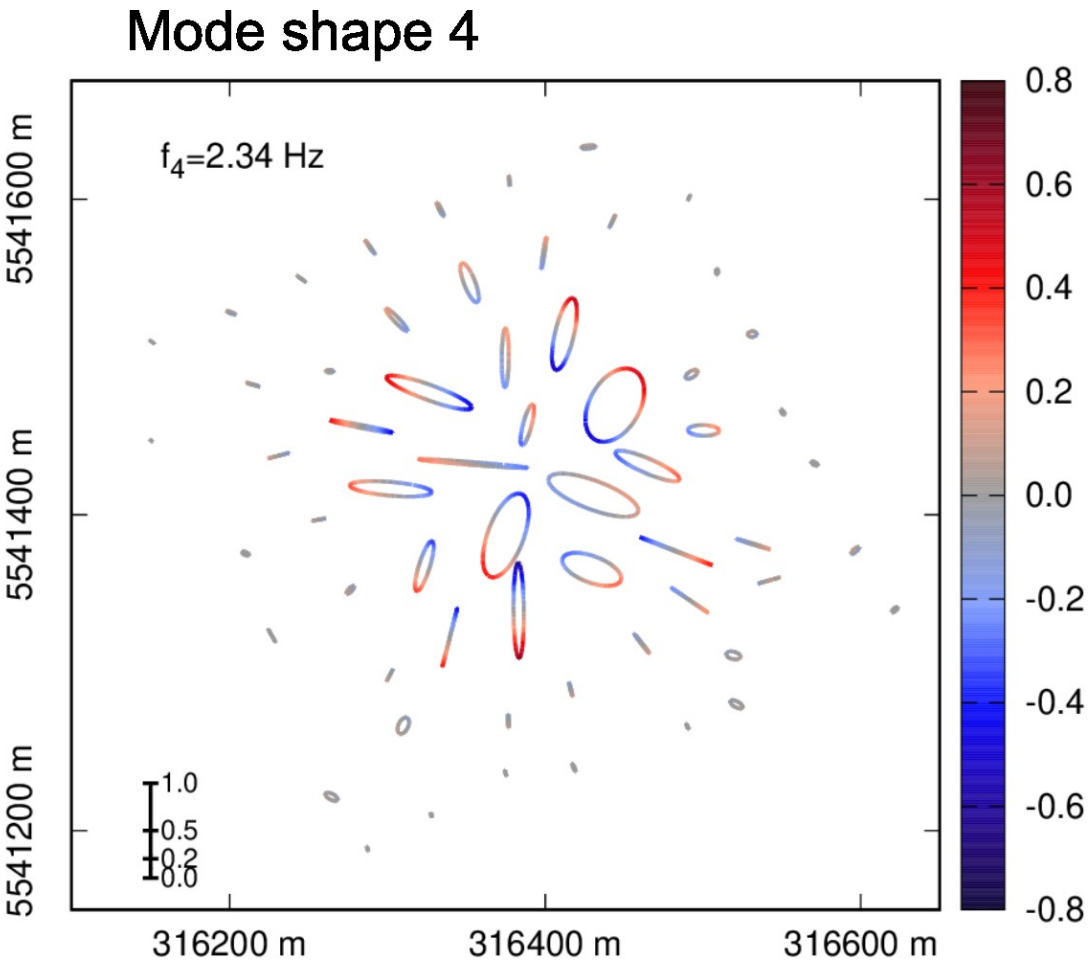
3.9 Supplementary material



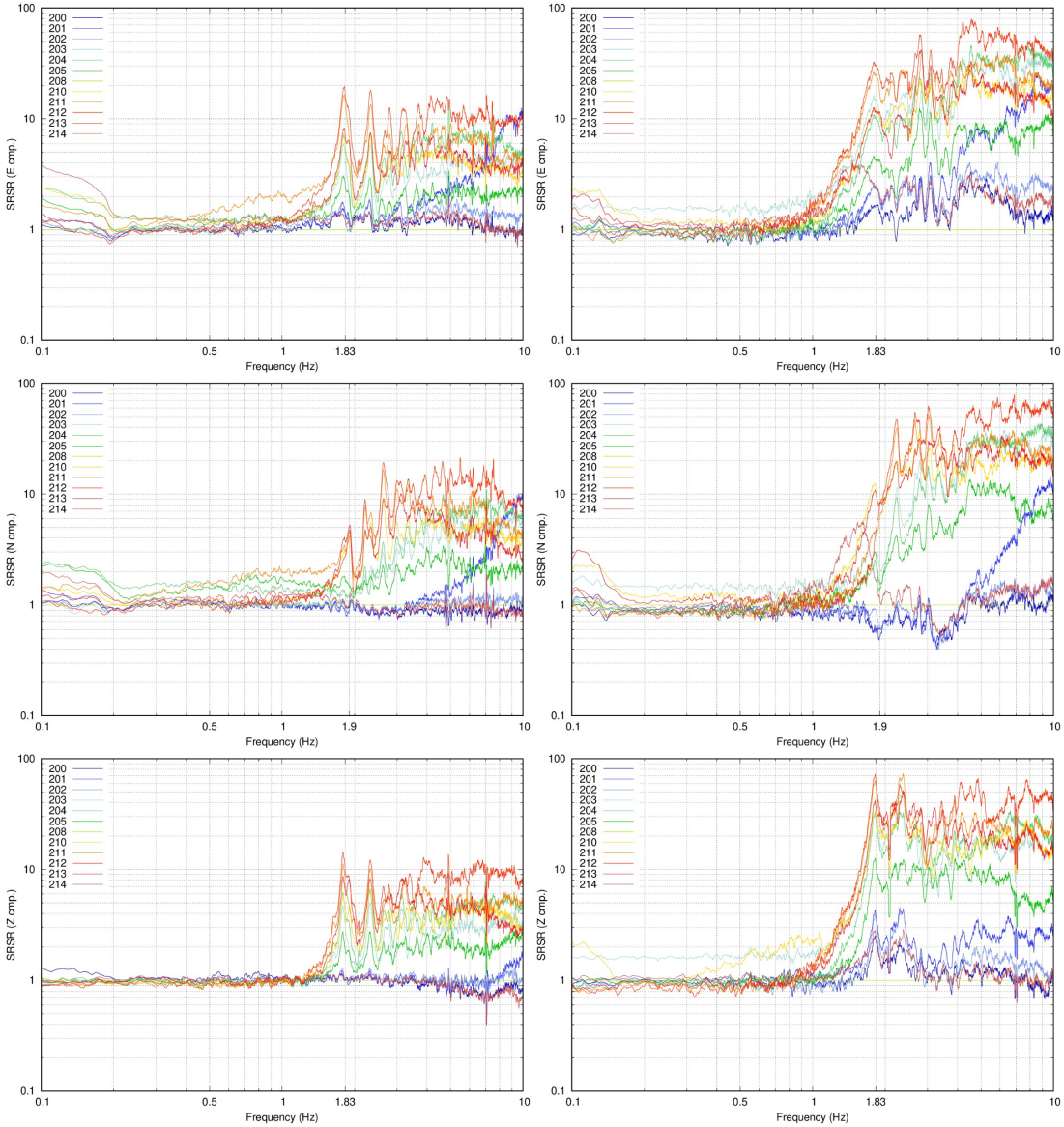
Supplementary Figure 3.1 Map of all deployed seismometers. Color scheme of deployed stations is the same as in Figure 3.1. in the main text.



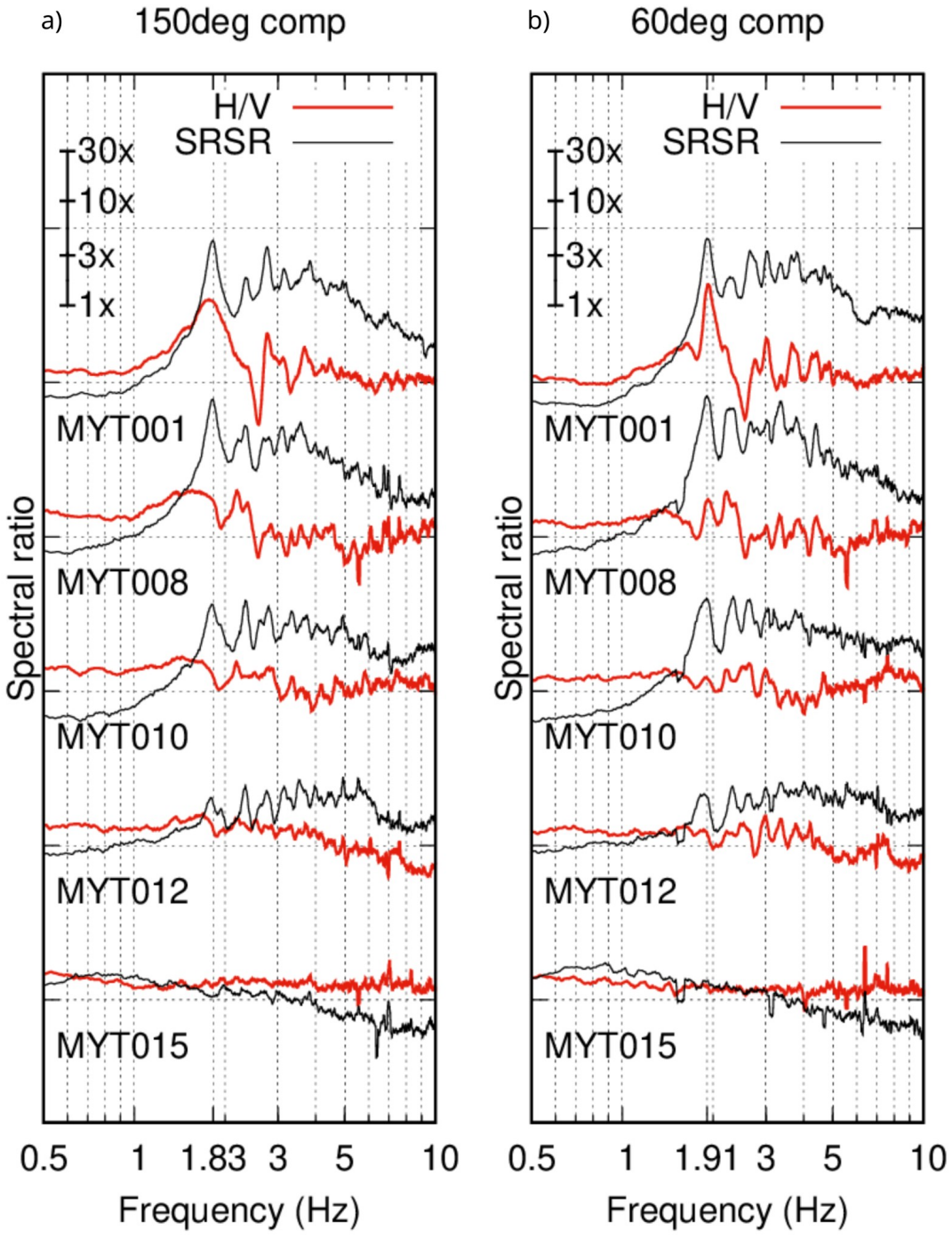
Supplementary Figure 3.2 Direction of maximal polarization obtained by TFPA. Length of the lines is related to particle motion of the given mode, and it is normalized with respect to the highest value. a) The black lines represent direction of the mode shape 1 (1.83 Hz). b) The red lines represent direction of the mode shape 2 (1.91 Hz).



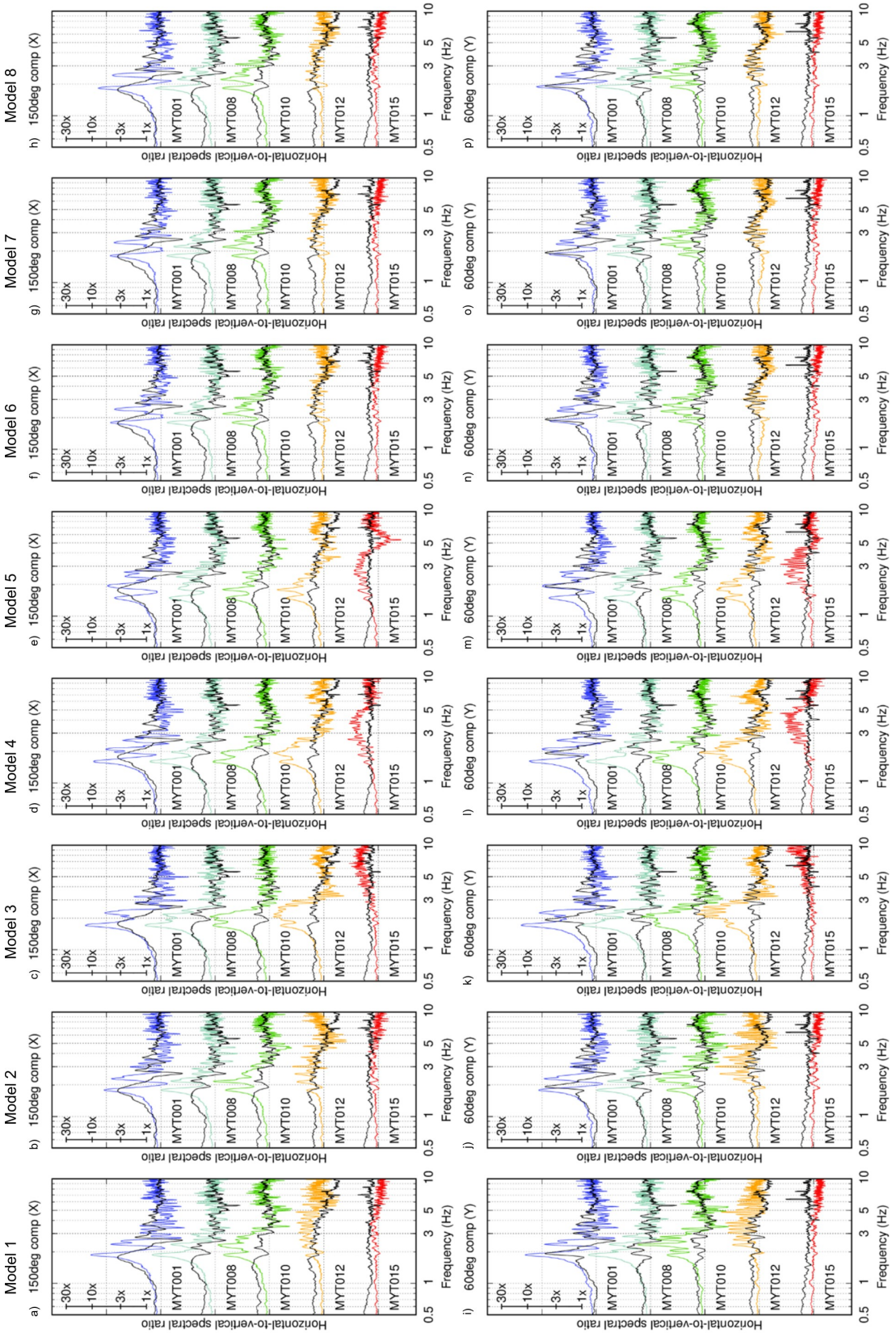
Supplementary Figure 3.3 Particle motion of mode 4



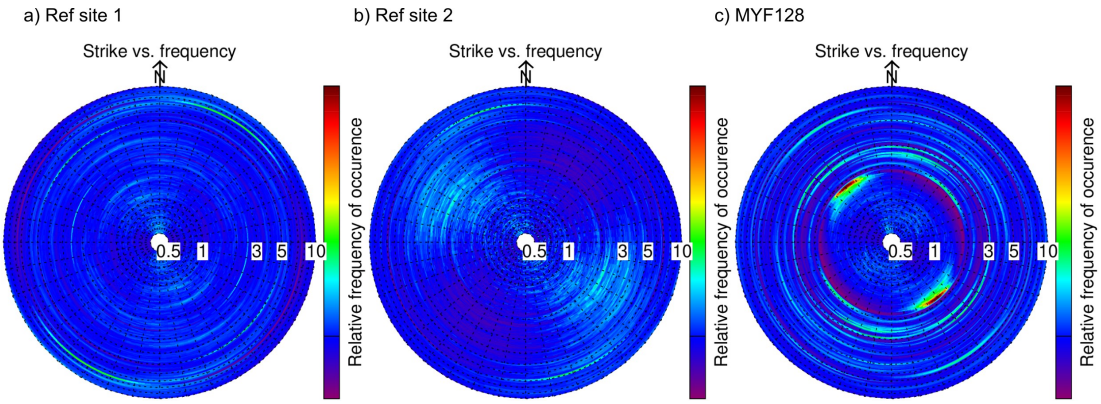
Supplementary Figure 3.4 Comparison of amplification without any internal active source (left column – top to bottom ENZ components), or with one (right column – top to bottom ENZ components). Color palette represents given stations.



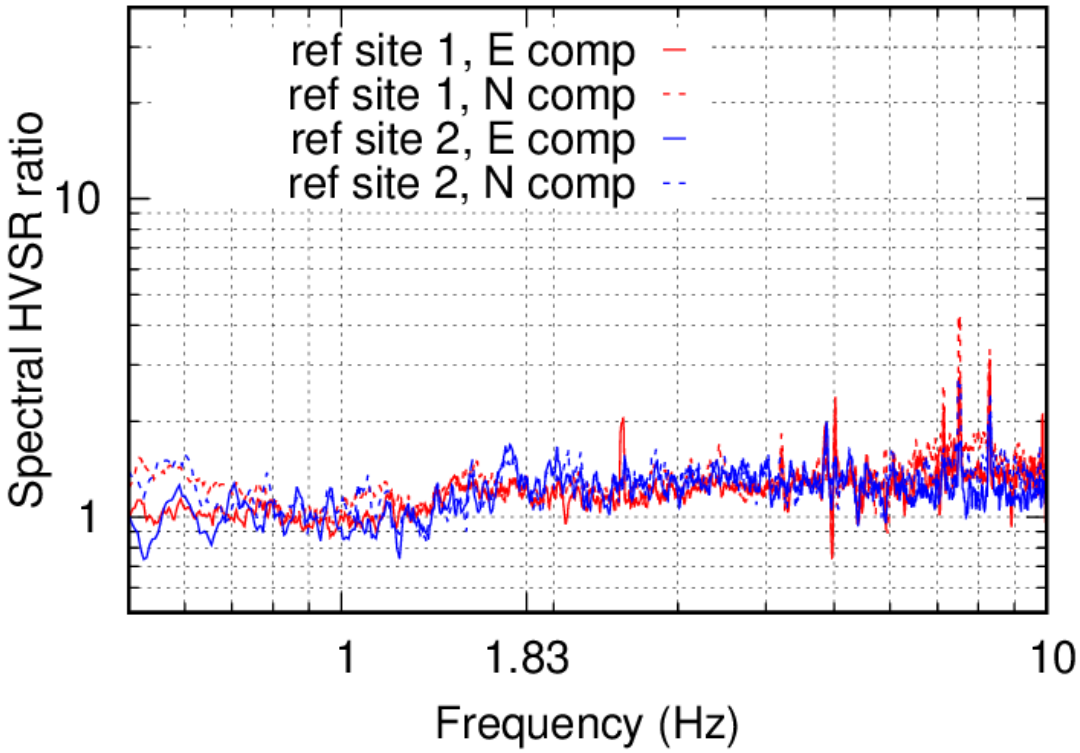
Supplementary Figure 3.5 Comparison between SRSR (black line) and HVSR (red line), a) for the horizontal component rotated 150 degrees from north, b) for the horizontal component rotated 60 degrees from north.



Supplementary Figure 3.6 Comparison of observed (black line) and synthetic (colorful line) HVSR for non-viscoelastic models 1 – 8 from Labuta et al. 2023. Subsets a) – h) represent the horizontal component rotated 150 degrees from north for models 1 -8, subsets i) – p) represent the horizontal component rotated 60 degrees from north for models 1 -8.



Supplementary Figure 3.7 Results of the TPFA strike orientation of ground motion in relation to frequency, a) for the reference site 1, b) for the reference site 2, c) for the station MYF128 close to the borehole.



Supplementary Figure 3.8 Results of the HVSR method for the reference station sites 1 and 2 for not rotated components E and N.

4 3D Resonance and Subsurface Structure of Newly Identified Felsic Maar-Diatremes in West Bohemia: A Multidisciplinary Geophysical Approach

4.1 Introduction

Maar diatreme-volcano undergoes an explosive phreatomagmatic eruption (i.e. eruption with a presence of groundwater) which usually creates a shallow crater depression surrounded by an ejecta ring of exploded material (White & Ross, 2011). The shallow crater can be post-eruptively filled with lake and subsequently lacustrine sediments, carrying information on climate history (Macrì et al. 2023, and references therein). If the lake dries out, the structure is called the dry maar (Sirocko et al., 2013). Below the sediments there is a conical structure of bedded and unbedded volcanic breccia with a feeding dyke connected from below (Ross et al., 2017). The maar-type volcanoes in general are the second most common volcanoes on land (Lorenz, 2007). The chemical composition of diatremes is characterized in most cases by mafic to ultramafic magmas (White & Ross, 2011). A few documented cases of felsic maar volcanoes describe these structures as rich in metallic ores, like gold and silver (White and Ross 2011 and reference therein).

The studied volcanic area (Figure 4.1c) in West Bohemia, Czechia (Figure 4.1d) belongs to the Cheb-Domažlice Graben (CDG) uplifted shoulder (Ulrych et al., 2003). The CDG together with the Eger rift zone (ERZ) creates a seismically active volcanic junction in the western part of the Bohemian Massif (BM) (Fischer et al., 2014; Horálek & Fischer, 2008; Horálek et al., 2000). The genesis of ERZ and CDG occurred during the Cenozoic Era as alkaline volcanic series, starting in Oligocene epoch, and lasting until Quaternary period (0.43 – 0.11 Ma) (Ulrych et al., 2003).

The area itself is located about 10 km east of the town of Teplá. In the area there are two distinguishable shallow depressions (Figure 4.1c), including man-made ponds and delimited by prominent hills consisting of volcanic rocks. The northern depression at the village Nežichov (Figure 4.1a), about 1.5 km in diameter is surrounded at the west side by hills Třebouňský vrch and Branišovský vrch (brown labels in Figure 4.1c), which were identified and dated in an abandoned quarry by Ulrych et al., 2003 as felsic trachyandesite aged 12.1 Ma. The southern depression east of the hill Sepuska, which is about half the diameter of the northern one or the hill itself were not dated or geochemically determined.

This study investigates whether the geomorphological depressions near the village of Nežichov and at Sepuska Hill represent volcanic diatremes, and explores how these features can be characterized using available geophysical methods. The previously studied maar diatremes in the Bohemian Massif (BM) include for

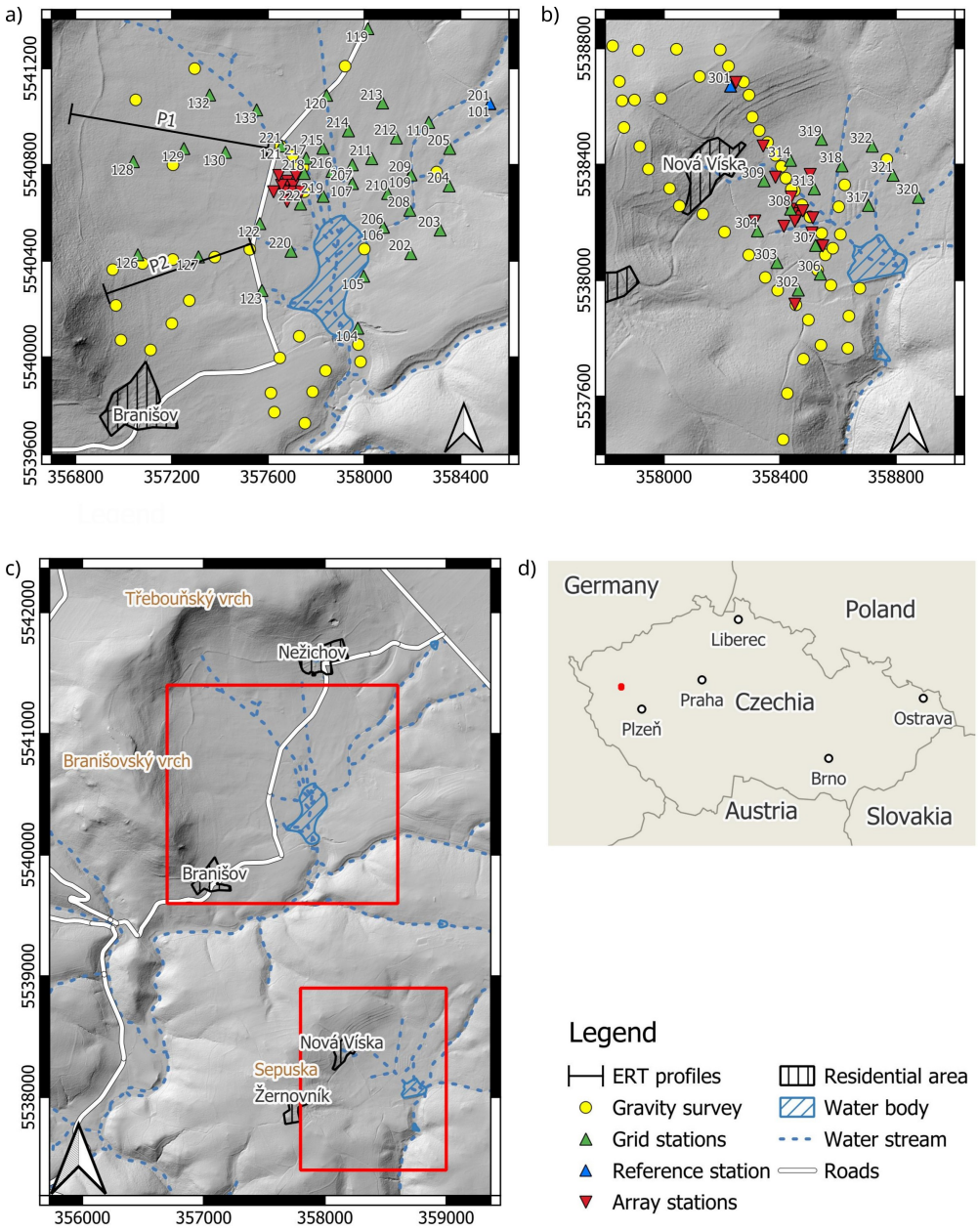


Figure 4.1 Schematics of the studied areas. Ambient seismic noise survey stations are denoted by triangles – green triangle for grid stations with their ID; blue triangle for reference stations used for Site-to-Reference Spectral ratio for the grid survey noted 101,201,301; red upside-down triangles for array stations. Points surveyed by gravimetry are denoted by yellow circle. Electric resistivity tomography (ERT) profiles P1 and P2 are marked by the black line with whiskers at both ends. The gray shaded base map is sourced from the Digital Terrain Model of the Czech Republic of the 5th generation provided by the Czech Office for Surveying, Mapping and Cadastre. The symbology for residential area, water body, water stream and roads for the base map is sourced from the OpenStreetMap. The coordinates are in meters of WGS84 UTM projection in the 33N zone. a) Map of a survey conducted on the Nežichov structure. b) Map of a survey conducted on the Sepuska structure. c) Overview map of both structures in relation to each other. d) Overview, where the studied area is in Czechia.

example the Mýtina maar where gravimetric, magnetic, and electrical survey were carried out (Flechsig et al., 2015; Lied et al., 2020; Mrlina et al., 2009), the Bažina maar (Hrubcová et al., 2023) or the most recent study on maars in north-eastern part of BM carried out by Kašing et al. (2025). The Mýtina maar was also surveyed by ambient seismic noise survey (ASNS) and numerical modelling (Labuta et al., 2023, 2025). A key advantage of the ASNS method is its ability to rapidly characterize a site using the Site-to-Reference Spectral Ratio (SRSR) approach with only two seismic stations. This allows for the identification of the structure's fundamental amplification frequency (FAF) and amplitude ratio. Subsequent measurements with multiple stations enable mapping of the FAF across the site, helping to confirm the presence of 3D local site effects—particularly when identical FAF values are observed above the structure, suggesting the presence of a maar (Labuta et al., 2025). The existence of a maar structure is usually confirmed by gravimetric survey by comparing the difference in the Complete Bouguer anomaly (CBA) (Mrlina et al., 2009), surveying the ejecta ring using magnetometry (Flechsig et al., 2015; Mrlina et al., 2009), difference in electric resistivity between the structure and the bedrock (Mrlina et al., 2009) or by drilling a borehole (Hrubcová et al., 2023; Mrlina et al., 2009).

4.2 Methods

Based on previous studies of Mýtina maar (Labuta et al., 2023, 2025), we have recorded ambient seismic noise at the sites of interest and processed it utilizing Site-to-reference spectral ratio (SRSR), Time frequency polarization analysis (TPFA), Frequency domain decomposition (FDD) and Frequency-wavenumber array (F-K) method. An advantage of using ambient seismic noise is its continuous presence, even in seismically quiet areas, as it is generated by human activity or consists of low-frequency microseisms—seismic tremors caused by oceanic and lacustrine wave action (Bonnefoy-Claudet et al., 2006). To interpret our results, we modeled synthetic ambient noise for which we developed a material model containing Vp, Vs and density, designed after the material model of Mýtina maar (Labuta et al., 2023) and analyzed it with the SRSR method. Furthermore, we also carried out a gravimetric survey and electric resistivity tomography (ERT) to better understand the results of the ambient noise survey, as the gravimetry is commonly used for maar structures (Mrlina et al., 2007, 2009; Mrlina et al., 2019).

4.2.1 Methods for processing the ambient seismic noise

Site-to-reference spectral ratio (SRSR)

To determine the frequency-dependent amplification of ground motions in the structure, we employed the SRSR method on the ambient seismic noise. Initially, the SRSR method was designed for analyzing earthquake recordings (Borcherdt, 1970) and was later adapted for ambient noise analysis (Irikura & Kawanaka, 1980; Kleinbrod et al., 2017; Pischiutta et al., 2017). This technique requires at least two seismic stations recording simultaneously. A reference station should be positioned on outcropping bedrock as close to the study area as possible, while a

field station (or stations) should be placed within the study area. This setup allows for estimating the relative wave-field amplification between the stations. The amplitude spectra, estimated using the multitaper method (Multitaper Fourier Spectra, MFS;(Prieto et al., 2009)), for each component at the field station are divided by the corresponding component of the MFS at the reference station. The resulting ratio provides an estimate of the frequency-dependent amplification of the field site relative to the reference site. The method assumes that noise sources are distant from the study area, so that the source and path effects are the same for both field and reference stations, and thus are eliminated in the field/reference MFS ratio. Therefore, this method is suitable for surveying areas far from both man-made and natural seismic noise sources.

4.2.2 Time frequency polarization analysis (TFPA)

The Time-Frequency Polarization Analysis (TFPA) characterizes particle motion within three-component seismograms. For short time windows, the motion can be approximated by an ellipse and is described by its strike, dip, and ellipticity, all of which are frequency-dependent (Burjánek et al., 2012, 2019).The particle motion's strike is described as an angle from north of the semi-major elliptical axis, the dip then the angle from the horizontal plane downwards, describing the tilting of the particle motion ellipse. The ratio between semi-major and semi-minor axis of the polarization ellipse then represents the ellipticity.

Frequency domain decomposition (FDD)

The Frequency Domain Decomposition (FDD) method was originally introduced for the modal analysis of buildings and other man-made structures (Brincker & Ventura, 2015; Michel et al., 2010). It enables the identification of a structure's natural vibration modes, resonance frequencies, and mode shapes. Later, this method was adopted in geosciences for unstable rock columns (Bottelin et al., 2013), sedimentary basins (Ermert et al., 2014), freestanding rock towers (Moore et al., 2019)), or for rock slope instabilities (Häusler et al., 2019, 2021). The method involves estimating the cross-power spectral density matrix, which consists of complex-valued cross-power spectral densities calculated between all seismogram traces for a specific frequency. The auto-spectral densities of the normal modes motion are described by the eigenvalues of the cross-power spectral density matrix. The largest eigenvalue exhibits peaks at the natural frequencies of a local structure. The associated complex eigenvectors contain 3-D modal vectors that describe the particle motion with the relative phase shift of the mode across the studied site (Brincker & Ventura, 2015; Poggi et al., 2014).

The frequency-wavenumber (F-K) array analysis

The F-K method, developed by Capon (1969), is used to estimate the phase velocities of planar seismic waves. The ambient seismic noise wavefield is commonly assumed to consist of a random set of planar waves arriving from various directions, an assumption that holds primarily when the sources are distant. Due to this randomness, an array measurement configuration is required to separate the incoming waves from the wavefield. In this study, we employ a high-resolution

three-component F-K analysis implemented in the Geopsy software package (Wathelet et al., 2018). The seismograms are divided into partially overlapping short time windows, for each of which the F-K spectrum is computed. These spectra are then averaged over the entire seismogram. The local spectral maxima then represent individual planar waves with given azimuth and frequency recorded at the array stations. The frequency resolution is determined by the spatial distribution of the stations – the minimum resolvable frequency depends on the maximal distance between the two farthest stations, the maximum frequency then on the minimal distance between two closest stations (e.g., Wathelet et al. 2008). Ambient seismic noise is dominated by surface waves (e.g., Bonnefoy-Claudet et al. 2006), with Rayleigh waves near the surface exhibiting elliptical particle motion in the radial–vertical plane relative to the direction of wave propagation. The ratio of the major semi-axes in the radial and vertical directions—known as Rayleigh wave ellipticity. In contrast, Love waves are analyzed on the horizontal component transverse to the direction of wave propagation. The phase velocities of both types of surface waves are frequency-dependent, resulting in dispersion curves from which individual surface wave modes can be identified using the Geopsy software (Wathelet et al., 2020). Rayleigh wave ellipticity is, in general, also frequency-dependent. Subsequently, we used the Dinver module of the Geopsy package to constrain vertical shear wave velocity profiles by the dispersion and ellipticity curves. Subsequently, we used the Dinver module of the Geopsy package to constrain vertical shear-wave velocity profiles using both dispersion and Rayleigh wave ellipticity curves. The modeling was based on assumed constraints, including a constant density of 2.2g/cm^3, increasing shear-wave velocity with depth, and progressively thicker layers. These constraints were intended to discourage the inversion from introducing artificial sharp velocity contrasts that are not required by the data Dinver randomly generates a set of velocity profiles that satisfy the prescribed constraints and computes the corresponding synthetic dispersion curves. These are then evaluated using the neighborhood algorithm to identify the best-fitting models (Sambridge, 1999; Wathelet et al., 2008).

4.2.3 Numerical modeling

The synthetic seismic noise was computed using the SW4 software (N. Petersson & Sjogreen, 2017; Sjögreen & Petersson, 2012) on the computational grid 4 x 4 x 2.5 km with horizontal and vertical spacing of 10 m between grid vertices and a mesh refinement in 60 m depth halving the spacing to 5 m to satisfy the requirement of 6 grid points per shear wave wavelength at maximum computation frequency of 5 Hz . Minimum shear wave velocity was obtained from the 1D profile from F-K analysis and dispersion curves inversion described above.

Using the reciprocity theorem, which allows for the interchange of seismic source and receiver locations (e.g., Eisner and Clayton 2001), we place three orthogonally oriented Ricker pulses—along the x, y, and z axes with a central frequency of 2Hz — at the location where ambient vibrations are to be simulated. We set a mesh of hypothetical receivers at depths 0 and 1000 m in a zone between the damping zone of the model and the conical structure in the middle, so we obtain Green's functions for each pair of source-receiver. This geometry ensures that no receiver—when treated as a seismic source under the reciprocity theorem—violates

the assumption of a uniformly azimuthal distribution of ambient noise sources situated outside the structure. The final one-hour long time series of the synthetic seismogram is then convolution of randomly summed point-force sources with randomized source time functions (Burjánek et al., 2019).

4.2.4 Gravimetry

The gravity data were processed in usual way with corrections for earth tides, gravimeter's drift, normal gravity field (latitude correction), elevation and terrain impact (terrain corrections to 167 km distance from each point). The final values of complete Bouguer anomalies were interpolated to provide grids for gravity maps. Since no significant regional trend was later identified in the gravity maps, the boundaries of negative gravity anomalies could be outlined using the contours of maximum horizontal gravity gradients. These prominent gradient contours delineate the edges of geological structures composed of rocks with contrasting densities.

4.2.5 Electric resistivity tomography (ERT)

Electrical Resistivity Tomography (ERT) is used for characterization of subsurface electrical resistivity in lateral and vertical directions. In principle, direct current I is injected into the ground, the potential difference U is recorded and apparent resistivity ρz is calculated through Ohm's law considering geometric factor k. By changing combination of current/potential electrodes along the profile, data corresponding to different positions and depths are acquired. Subsequently ρz is converted to the (true) subsurface resistivity ρ by an inversion process, which attempts to find a resistivity model explaining the measured data. The inversion process is carried out through iterative non-linear regularized inversion algorithms depending on data dimensionality in 2D, 3D or 4D (Ellis & Oldenburg, 1994; Loke & Barker, 1996). Considering wide range of natural earth materials resistivities, ERT can be used for imaging of various geological targets including e.g. karst features, faults, volcanic structures, landslides, or sedimentary successions (e.g. Comina et al. 2024; Hrubcová et al. 2023; McCalpin et al. 2023; Petronis et al. 2018).

4.3 Field experiments

4.3.1 Ambient seismic noise survey

Ambient seismic noise was recorded to identify the amplification frequency and ratio of the fundamental and higher oscillation modes using the SRSR method, and to perform modal analysis of the structure using FDD. For these methods, seismic stations were deployed in an irregular grid. To estimate the dispersion curve using F-K analysis and subsequently perform shear-wave velocity inversion, the stations were arranged in a mutually rotated pentagonal or spiral array geometry. Both Sepuska and Nezichov sites were surveyed with an irregular grid and an array station arrangement. Recordings of ambient seismic noise were acquired by

FairField Zland Node 5 Hz seismic stations. The stations' position was established by differential GPS apparatus with 1 cm precision.

All stations used in the grid survey were placed in shallow holes (approximately $50 \times 50 \times 50$cm) to limit the effect of wind and avoid interference from vegetation. The initial location of the reference station for the SRSR method was chosen based on topography and the geological map. It was close to the hypothesized maar, to fulfil the assumptions of the SRSR method. A horizontal-to-vertical spectral ratio of ambient noise recordings was calculated for the reference station and TPFA analysis was performed to verify the absence of local site effects.

Sepuska

The area east of the peak Sepuska was surveyed by an irregular grid of 15 stations with spacing ranging from 120 to 170 m (green triangles in Fig 4.1b.) between neighboring points. The reference station 301 (blue triangle in Figure 4.1b) was placed about 300 m NW from the area. All the stations were recording ambient seismic noise during a day for 3 hours continuously.

The array measurement (red triangles in Fig 4.1b) consisted of 16 stations laid-out as 3 branches of half-spirals with azimuths: 18, 138, 258 degrees, and increasing station radii from the center along each branch which contained 5 stations: 5, 12, 25, 60, 145 m. The last, 16th station was the center of the array. All stations recorded for 2 hours. During this stage, we also deployed the reference station to the north of the array and additional stations along the NW – SE trending profile to compute the SRSR. Unfortunately, due to their placement directly on the surface rather than in shallow holes, the array stations recorded high levels of nonseismic noise, mostly caused by wind, which made their data unsuitable for the SRSR method.

Nežichov

South of the village Nežichov we carried out two grid measurements and one array configuration. The first grid was aimed at surveying the wider area based on topology with greater station spacing spanning 200 – 320 m, while the second grid with spacing 100 – 160 m was proposed based on the SRSR results of the first measurement to cover the area of the observed amplification. During the first deployment, we utilized 19 stations plus 1 reference station (marked by a blue triangle and notation 101 in Figure 4.1a) 250 m NE from the area. All these stations were recording simultaneously during the night for 8 hours. The second deployment was carried out for 3 hours during the day, and it consisted of 21 stations plus 1 reference station, which was placed in the very same spot as the previous reference station (marked by a blue triangle and notation 201 in Fig 4.1a). Additionally, 4 more stations were placed in the same holes as previously to compare the reliability of the results. These pairs are marked in Figure 4.1a as 206-106, 207-107, 209-109 and 221-121.

The array deployment configuration differed from the Sepuska area due to the space constraints. We deployed 4 circles of 5 stations in each circle with radii 5, 12, 25, 60 m, the first station of each circle rotated by 36 degrees clockwise with respect to the previous circle. The array stations were recording the ambient seismic noise for 2 hours.

4.3.2 Gravity survey

To constrain the observations based on the ambient vibrations, a semi-detailed gravity survey was performed in both localities of Sepuska and Nezichov. The Scintrex CG-6 gravimeter was used to measure gravity values at 50 points at Sepuska and 30 points at Nezichov sites. At Sepuska, the measurements were arranged along two approximately north–south-oriented lines, one of which passed through the center of the morphological depression (see Figure 4.1b). At Nežichov, the stations were distributed in a non-regular pattern designed to efficiently cover the study area and adequately resolve the expected structure (see Figure 4.1a). The gravity survey was supported by GNSS observations of the coordinates of the gravity points. The Trimble R10 receiver was used for this survey in Real-Time Kinematic positioning (RTK) mode.

4.3.3 ERT

ERT data were collected using a five-channel ARES II resistivity system (GF Instruments, Brno, Czech Republic) with an inverse Wenner–Schlumberger (IWS) electrode array and 5m electrode spacing. The IWS configuration enabled multi-channel acquisition, significantly reducing the total measurement time. Profile P1 was 835m long, and profile P2 reached 635m. A total of 15 cable sections, each 40m in length, were used, allowing for a maximum profile length of 595m per setup. The final profile lengths were achieved using a roll-along technique, with 80m sections progressively shifted.

4.4 Results

4.4.1 Ambient noise processing for both structures

Ambient seismic noise data for both structures were processed using TFPA, F-K analysis, and shear-wave velocity inversion. Additionally, SRSR and FDD were applied iteratively: first, areas were mapped where the SRSR method indicated a fundamental-mode amplification peak on both horizontal and vertical components. Then, for seismograms showing such amplification, the waveforms were rotated around the vertical axis into the principal particle motion directions determined from FDD to compute the maximum amplification by SRSR.

Sepuska

We have applied FDD, TPFA, SRSR to the seismic ambient noise grid survey and F-K analysis to the array measurement. The FDD eigenvalues (Figure 4.2a) were obtained from the spectra computed with 300 s long sliding time window. Here we were able to distinguish between the first two close peaks at 1.14 and 1.17 Hz, plus we also observed a higher mode at 1.28 Hz. The eigenvectors corresponding to the first two modes (Figure 4.2b and c) exhibit linear particle motion and are aligned between stations along azimuths of approximately 30° for the first mode and 120° for the second. In contrast, the third mode (Figure 4.2d) shows elliptical particle motion at several stations and forms a circular pattern, with an apparent center located near the pond.

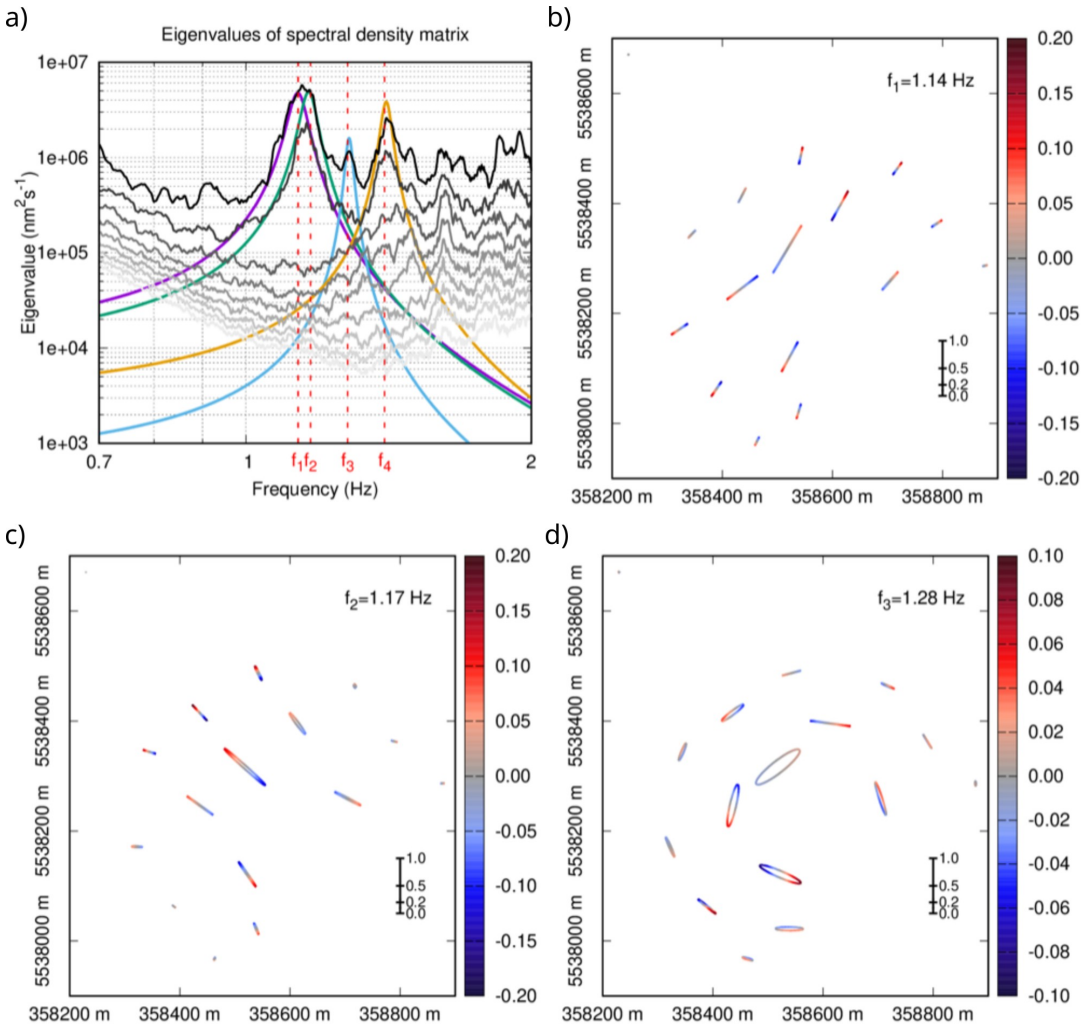


Figure 4.2 Results of the FDD modal analysis for the Sepuska structure. a) Frequency-dependent eigenvalues of cross-spectral density matrix carried out for the second grid survey from which we could identify 3 modal frequencies (f1, f2, f3) at 1.14, 1.17, 1.28 Hz with color solid lines describing the best fitting single degree of freedom (SDOF) oscillator for each mode. b) Particle motion of mode 1. c) Particle motion of mode 2. d) Particle motion of mode 3. In b, c, and d, the scale in the southwest indicates the dimensionless horizontal amplitude of mode particle motion, while the color scale depicts the dimensionless vertical amplitude of mode particle motion.

The recordings of all stations processed by the SRSR were then rotated into these two detected azimuths along the vertical axis, and their spectra were calculated also with a 200 s long sliding time window to get high spectral resolution. We also identified two closely separated peaks on horizontal components, at 1.14 Hz for 30 degrees and 1.17 Hz for 120 degrees rotated recordings (Figure 4.3d). The peaks are distinctive on all recorded stations. We also observed higher modes at 1.28 Hz and 1.61 Hz. The maximal observed amplification ratio for the first mode at 1.14 Hz reaches values of 20 and values of 14 for the second mode at 1.17 at the station 312 on the horizontal component. Vertical component has however highest values of 6 at 1.15 Hz at the station 318 close to the geomorphological edge of the surveyed structure. We used TIN interpolation in QGIS interface to generate a linearly interpolated map of natural logarithm of both horizontal

and vertical amplification ratios of modes 1 and 2. Linearly interpolated maps of horizontal component for both modes (Figure 4.3a and b) show similar shape of amplification distribution which is almost circularly shaped with slight elongation towards the southern part of structure. Map of vertical amplification (Figure 4.3c) does not follow this trend, instead the maximum is in the northernmost part of the surveyed area with a narrow elongation towards the south.

The TPFA was carried out with parameter ω_0 equal to 96 and in frequency band 0.5 – 5 Hz. We identified peak at 1.14 Hz representing significant direction of particle motion of the fundamental modes (first mode at 1.14 Hz and second at 1.17 Hz), the orientation of the peaks is pointing towards the center of the area with observed amplification (Figure 4.3a-c), close to the station 212. In this case, the station 212 follows the same azimuth as identified in FDD – 20 degrees from north.

Lastly, the F-K analysis yields the dispersion curve of Rayleigh waves in the frequency band between 2 and 6 Hz (Figure 4.4c). Here, the identified velocities are reaching values of 1100 m/s at 2 Hz and 200 m/s at 6 Hz for the fundamental Rayleigh (R0) mode. The inverted velocity model in Dinver with thin layers with increasing thickness and velocities constrains (both lower and upper possible velocity bounds) starts at 150 m/s Vs at the surface and increase to up to 300 m/s for depths between 15 to 35 meters, followed by a sharp velocity increase up to 1100 m/s below 35 meters of depth (Figure 4.4d). The model becomes poorly resolved below this depth.

Nežichov

For the Nežichov site we identified three peaks in the FDD frequency-dependent eigenvalues – at 0.92, 1.075 and 1.195 Hz (Figure 4.5a). We used ambient seismic noise recordings from the second survey and 300 s long sliding time windows to calculate the spectra. The corresponding eigenvectors to these eigenvalues describe the mode's particle motion. The motion is linear with a trend in azimuth around 120 degrees at all stations for the fundamental. Stations closer to the assumed country rock boundary show a slight tilt of the FDD angle for this mode, pointing more to the center of the morphologic depression (Figure 4.5b). The other two modes (Figure 4.5c and d) have a slightly elliptical shape, meaning there is a phase shift between the horizontal components. Moreover, the particle motion among the stations is rotated at each station in a way that it forms circular patterns for both modes, but the imaginary center of these circles moves from one mode to another. For the mode 1.075 Hz, the center lies between the stations 207, 211, and 216, while the mode 1.195 Hz has its center south of station 207, between stations 219 and 206, close to the pond.

The SRSR for Nežichov was computed from rotated seismograms, using azimuths of 120° and 210° as determined by FDD. To calculate the spectral ratio between 0.5 and 5 Hz we used a 100 s sliding window to calculate each spectrum. The highest vertical amplification (Figure 4.6d) for both modes was observed at station 215, at values of 3.4 for the first mode at 0.88 Hz and 5.2 for the second at 0.93 Hz; followed by station 209. Together, the two stations represent isolated amplification peaks on the western and eastern sides of the area with detected amplification. The bearing from station 215 to 209 is 105°, while the azimuth of the first mode's particle motion, as identified by FDD, is 120°, indicating that the

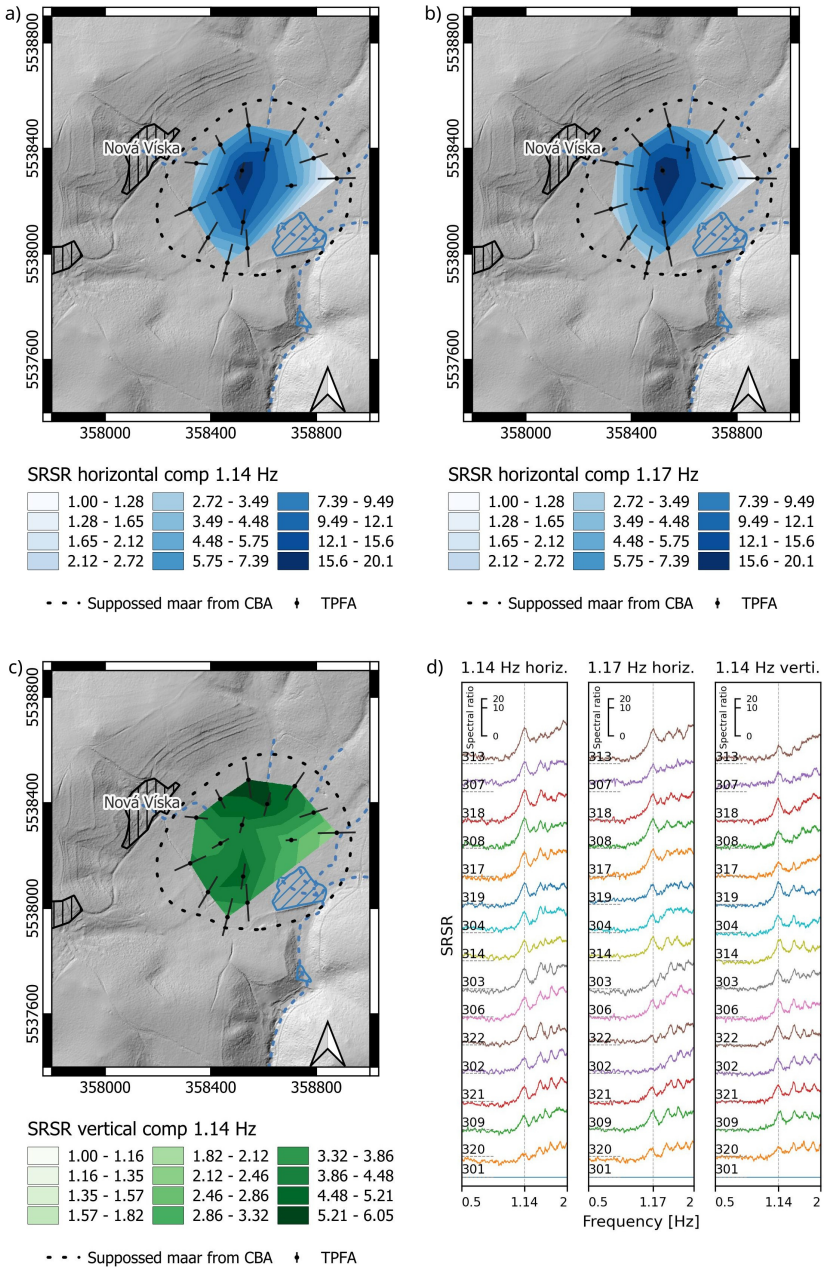


Figure 4.3 Sepuska SRSR amplification and orientation and amplitude of particle motion obtained from TPFA (relatively normalized black lines). The supposed maar structure obtained from gravimetric CBA denoted by the black dashed line. a) Interpolated amplification for the horizontal component rotated by 120 degrees at 1.14 Hz. b) Interpolated amplification of the horizontal component rotated by 30 degrees at 1.17 Hz c) Interpolated amplification of the vertical component at 1.14 Hz. d) SRSR for the horizontal component rotated by 120 degrees in the left box, by 30 degrees in the middle box and the vertical component in the right box. The short, dashed line below the station ID represents 1 – reference station 301.

alignment of these peaks—and the overall trend of vertical amplification—closely matches the orientation of the mode's particle motion.

The maximum horizontal amplification for both modes is, however, shifted to the neighboring station 216 with values of 15 and 16.5 for each mode, respectively.

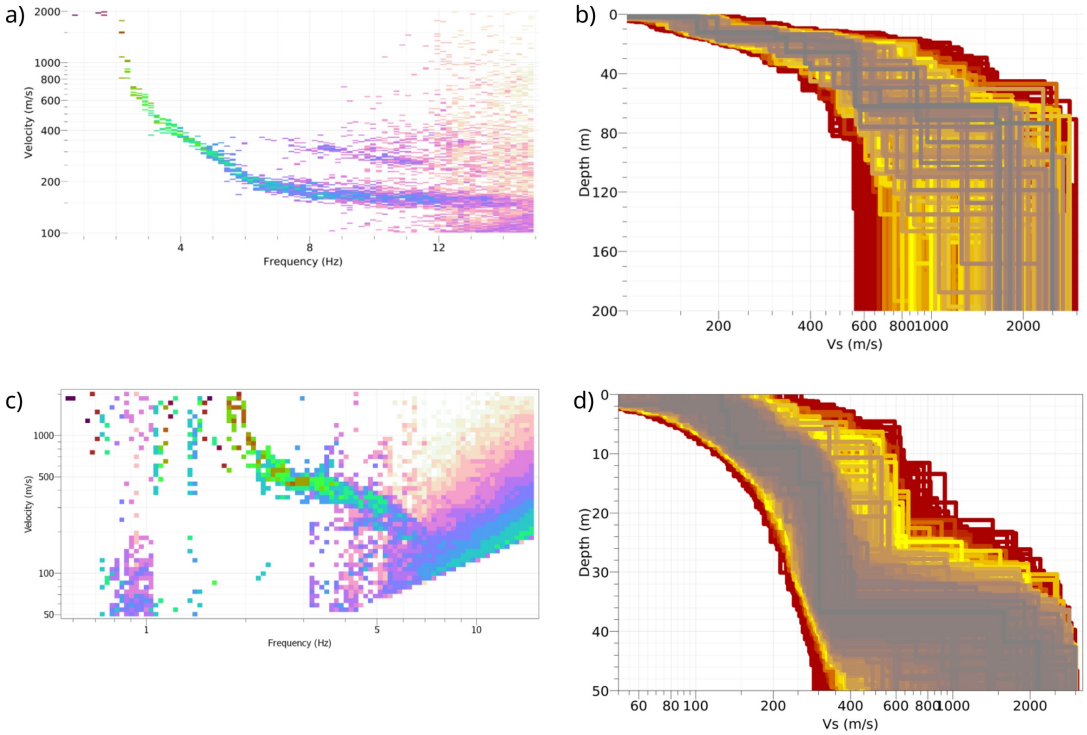


Figure 4.4 a) High-resolution F-K results of Rayleigh waves dispersion curve for the Nežichov structure between 2 – 12 Hz. b) Inverted shear wave velocity profile for the Nežichov structure from the Dinver software. c) High-resolution F-K results of Rayleigh waves dispersion curve for the Sepuska structure between 2 – 6 Hz. d) Inverted shear wave velocity profile for the Sepuska structure from the Dinver software.

The general trend of distribution of horizontal amplification follows an elliptical shape with the major semi-axis rotated again in direction of 120 degrees for the first mode (Figure 4.6a). The second mode has more circular shape and not such a profound identifiable orientation as the first mode (Figure 4.6b). The vertical component is similar in both modes with maxima at the stations 215 and 209 (Figure 4.6c).

The TPFA was also carried out in addition to FDD to determine the significant directions of particle motion in the studied frequency band 0.5 – 5 Hz. We used the ω_0 parameter of the mother Morlet wavelet with a value of 96 to obtain high spectral resolution. We observed one peak at 0.88 Hz at station 133 and all the stations east of the road, except for stations 101 and 104. The particle motion azimuth at this peak varies between stations. However, the general trend shows that the azimuths tend to point toward the center of the observed amplification area, located near station 107. At station 107 itself, the orientation of the azimuth has a W-E trend (Fig 4.6a-c).

The F-K analysis and inversion for the shear wave velocity profiles were carried out for the array measurement. We obtained a dispersion curve of Rayleigh waves and were able to identify the fundamental mode (R0) of the frequency band from 2 to 12 Hz with velocities ranging from 2000 m/s at 2 Hz to 150 m/s at 12 Hz (Figure 4.4a). The model was parametrized by multiple thin layers with increasing thickness and lower and upper bound of the shear velocity. Low-velocity layers—i.e., velocity inversions where a lower-velocity zone underlies a higher-

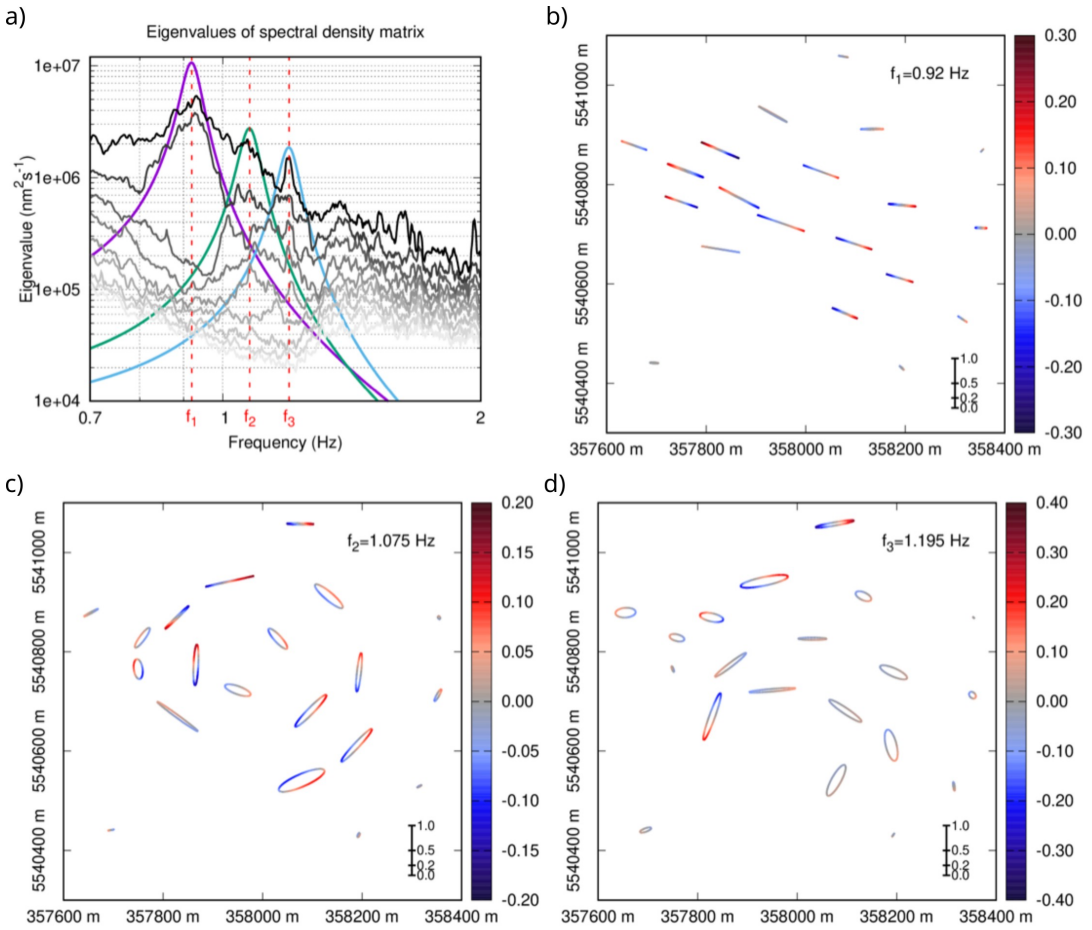


Figure 4.5 Results of the FDD modal analysis for the Nežichov structure. a) Frequency-dependent eigenvalues of cross-spectral density matrix carried out for the second grid survey from which we could identify 3 modal frequencies (f_1, f_2, f_3) at 0.92, 1.075, 1.195 Hz with color solid lines describing the best fitting single degree of freedom (SDOF) oscillator for each mode. b) Particle motion of mode 1. c) Particle motion of mode 2. d) Particle motion of mode 3. In b, c, and d, the scale in the southwest indicates the dimensionless horizontal amplitude of mode particle motion, while the color scale depicts the dimensionless vertical amplitude of mode particle motion.

velocity layer—are often challenging to interpret. In this study, we assumed a monotonically increasing shear-wave velocity with depth to avoid introducing poorly constrained velocity inversions. Low-velocity layers were only considered when supported by independent geological profiling, borehole data, or distinct features in the dispersion curve, such as pronounced peaks and troughs. The resulted inverted velocity model shows low Vs values down to 150 m/s at the surface, with an increasing gradient to 60 m where the velocity reaches 600 m/s, following a sharp increase to roughly 2000 m/s at 80 m depth (Figure 4.4b). Below that depth, the model lacks sufficient resolution, and the variability among inverted profiles increases significantly. The resulting velocity model was subsequently used to construct a material model for numerical simulations.

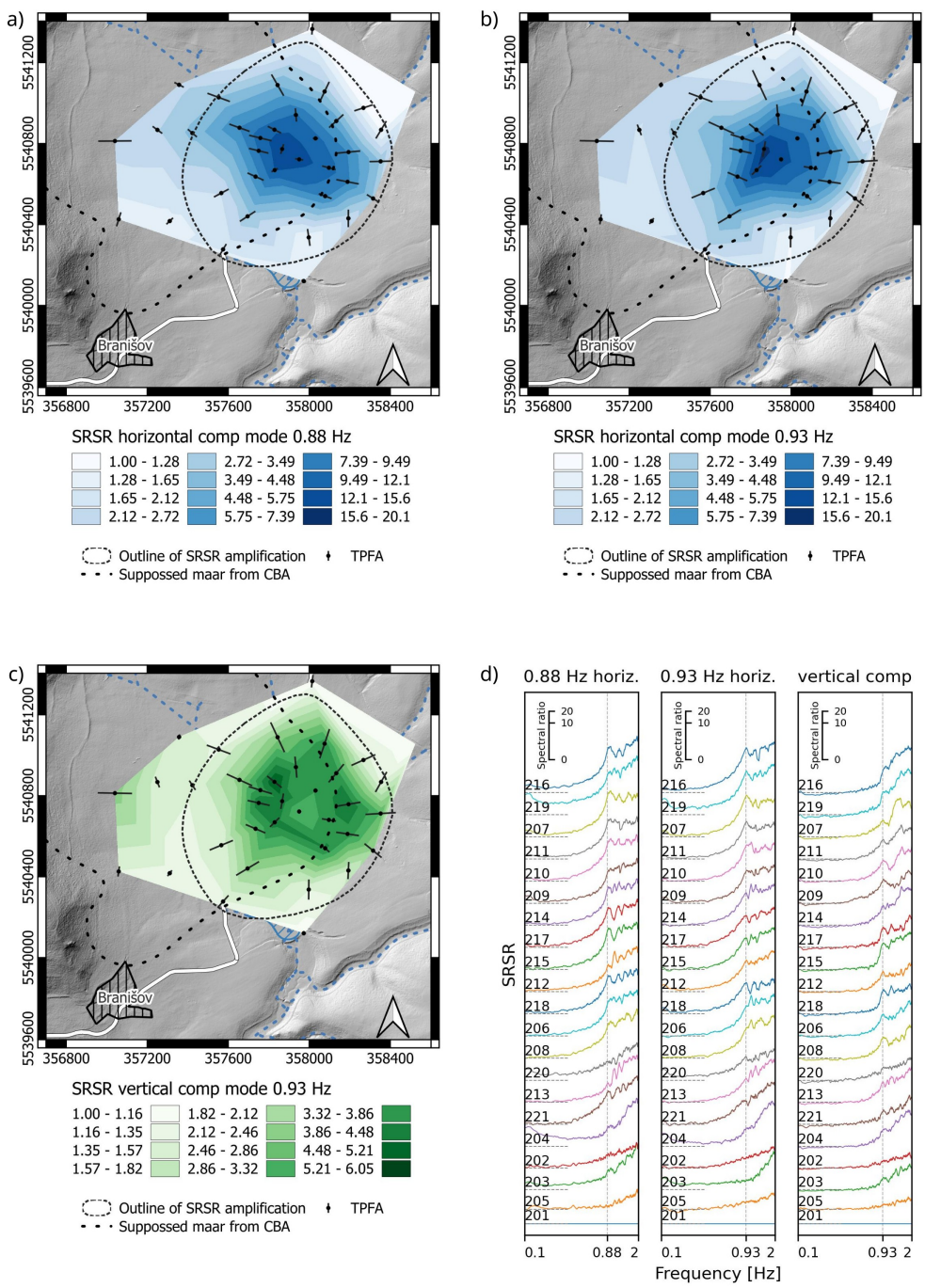


Figure 4.6 Nežichov SRSR amplification and orientation and amplitude of particle motion obtained from TPFA (relatively normalized black lines). The supposed maar structure obtained from gravimetric CBA denoted by the black dashed line. a) Interpolated amplification for the horizontal component rotated by 120 degrees at 1.14 Hz. b) Interpolated amplification of the horizontal component rotated by 60 degrees at 1.17 Hz c) Interpolated amplification of the vertical component at 1.14 Hz. d) SRSR for the horizontal component rotated by 120 degrees in the left box, by 60 degrees in the middle box and the vertical component in the right box. The short, dashed line below the station ID represents 1 – reference station 201.

4.4.2 Gravimetric processing for both structures

Negative gravity anomalies were observed at both study sites. In the smaller Sepuska structure, the amplitude of the anomaly is about 3.0mGal (Figure4.7b), while at Nežichov it reaches approximately 3.5 mGal (Figure4.7a). Despite no complete detailed survey was performed (rather a reconnaissance one) the results show a similar type of anomaly related to volcanic maar structures as found by Mrlina et al. (2009) in the Mytina maar, and later also by Mrlina et al. (2019) and Rohrmüller et al. (2018) in other maar structures. The negative anomalies in maar structures are typically caused by the presence of volcanic and country rock breccia filling the explosive channel. Additionally, the upper part of the maar fill is often composed of younger lake sediments deposited within the crater. Both breccia and, in particular, lake sediments have significantly lower densities than the surrounding country rock (see Mrlina et al. 2007, 2009).

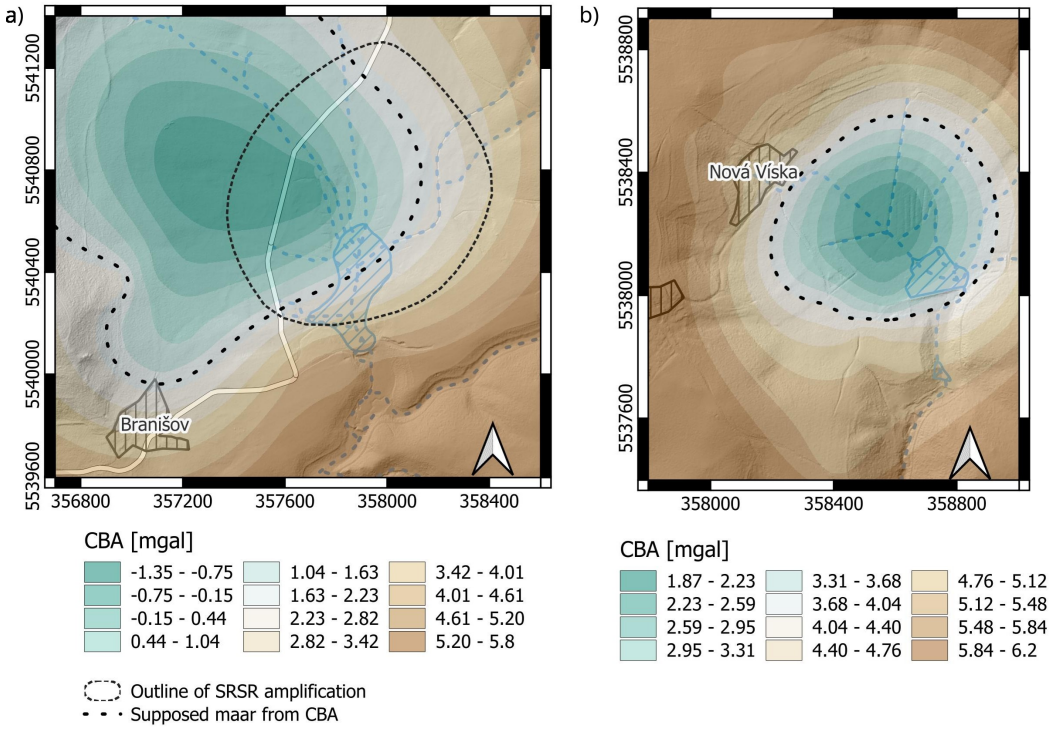


Figure 4.7 Gravity maps for: a) Nežichov and b) Sepuska; showing negative gravity anomalies indicating possible presence of maar structures. Dashed lines are partial boundaries of target structures derived from horizontal gravity gradients. The dotted line in Fig 7. a) denotes observed SRSR amplification.

While in Sepuska the structure seems to have a circular shape, in Nezichov the structure indicates certain prolongation in the NWW – SEE direction, see Figure 4.7a, with a small edge in SW. In Sepuska the location of the gravity low fits well with the result of the ambient vibration study. The positions of the structural boundaries also show good agreement between the two applied methods: the horizontal gravity gradient and the resonance locations identified from ambient vibration data. In contrast, in Nezichov the gravity anomaly center is located to the NWW of the center defined from the seismological one. On the other hand, the direction of seismological vectors seems to fit perfectly with this NWW-SEE

orientation.

4.4.3 Electric resistivity tomography

The acquired ERT data are of excellent quality, primarily due to wet field conditions and good electrode-to-ground coupling. Topographic data based on a LiDAR digital elevation model (Czech Office for Surveying, Mapping and Cadastre, 2017) were incorporated into all inversions. Initial data preprocessing involved preliminary 2D inversions in Res2Dinv using the L2 norm (Loke & Barker, 1996) to quickly assess RMS error statistics. Data points exceeding a predefined error threshold (approximately 5 %) were removed, and the cleaned datasets were saved for further processing. Final inversions were performed using the pyGIMLi library (Rücker et al., 2017), applying smooth constraints based on the L2 norm.

Profile P1 (Figure 4.8) can be clearly divided into two low-resistivity zones (below 20m) and two high-resistivity zones (above approximately 70m). The low-resistivity zone C1 is located between stationing 230–450m and reaches a thickness of nearly 100m, while the near-surface low-resistivity zone C2 lies between 600–800m with an approximate thickness of 50m. The high-resistivity anomaly R1 extends upward from depth and dominates the western part of the profile. Zone R2 separates the low-resistivity zones C1 and C2, and also partially overlies them.

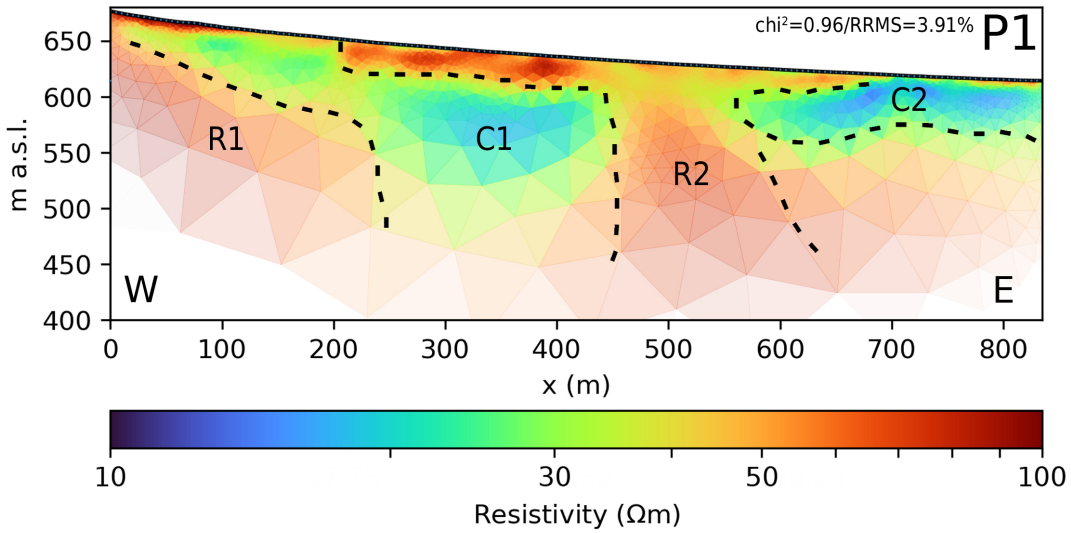


Figure 4.8 Electric resistivity tomography (ERT) of the profile P1. Low resistivity zone C1 and C2 marked by blue color while high resistivity zone R1 and R2 marked by red. Topography of the profile is based on LIDAR digital elevation model (Czech Office for Surveying, Mapping and Cadastre, 2017).

Profile P2 reveals a thinner low-resistivity zone (C3) with values below 30m located at the end of the profile, from stationing 400m onwards. Between 300–400m, a subvertical, intermediate-resistivity zone (C4) with values around 40m separates adjacent resistivity blocks. In the western part of the profile, a high-resistivity zone (R3) is present, with values ranging from 100 to 300m.

4.4.4 Numerical modeling of seismic response

3D material model of Nežichov structure

To simulate the seismic response at the Nežichov site, we developed a simplified material model based on the procedure outlined in Labuta et al. (2023). The visco-elastic model consists of density, P-wave and S-wave velocities, denoted Vp and Vs, and their respective attenuation quality factors Qp and Qs, which follow empirical formulas of Campbell (2009). Qs is linearly related to Vs through an equation Qs = 7.17+0.0276*Vs, Vs in [m/s] at the depth, and Qp is then double of Qs: Qp=2*Qs. Vp is set to Vs multiplied by the square root of 3 throughout the whole model.

The model is similar to the model of a Mýtina maar in West Bohemia (Labuta et al., 2023), an elliptical cone of volcanic breccia with a layer of sedimentary rock spanning from surface to the shallow subsurface on top of the breccia cone. For the Nežichov structure, the major and minor semiaxes of the ellipse are 750 m and 730 m at the surface, and the cone reaches depths of 2000 m (Figure 4.9d and e). The thickness of the sedimentary layer is set to 60 m according to the observed boundary from the F-K analysis and the diameter is set to 1300 m. The Vs rises from 150 m/s at the surface to 600 m/s at 60 meters of depth with a sharp increase in velocity with depth as the model enters the volcanic breccia with values of 1000 m/s at 100 m of depth up to 1450 m/s representing breccia fill from 200 m to the bottom of the cone at 2000 m of depth. The bedrock country rock velocities are the same as in Labuta et al. (2023), based on Málek et al. (2005).

Building on the results of the ERT survey, we prepared the Model B with the same parameters as the Model A, but added a block at top of the subsurface with a shear-wave velocity of 3000m/s and a thickness of 100m over one half of the cone to simulate the high-resistivity rocks, which are likely the result of a volcanic effusion (Figure4.9f and g). In both models, we evaluated the synthetic seismic response at three points on the surface: (1) in the center of the structure, (2) in the same location but with the overlying high-velocity block added, and (3) directly over the high-velocity block. These points are referred to in Figure4.9 as “center,” “center-block,” and “over-block,” respectively, and are marked by orange, brown, and red triangles in the model schematics.

Analysis of the synthetic seismic noise

We analyzed synthetic ambient noise using the SRSR method to compare simulated amplification characteristics with field observations.

The SRSR method can rely on a simple two-station setup: one station placed outside the structure serves as a reference, while the other is located inside the structure. This configuration makes it possible to efficiently compute synthetic seismograms, from which amplification ratios and fundamental frequencies can be estimated. These synthetic results can then be directly compared with field observations to assess the validity of the structural model. At the central point of the structure in Model 1, where the seismic response was simulated, we observed an amplification ratio of 7 at 0.95Hz on the horizontal components (Figure4.9a and b) and a ratio of 5.5 at 0.9Hz on the vertical component (Figure4.9c). These values are in reasonable agreement with the amplification observed at stations

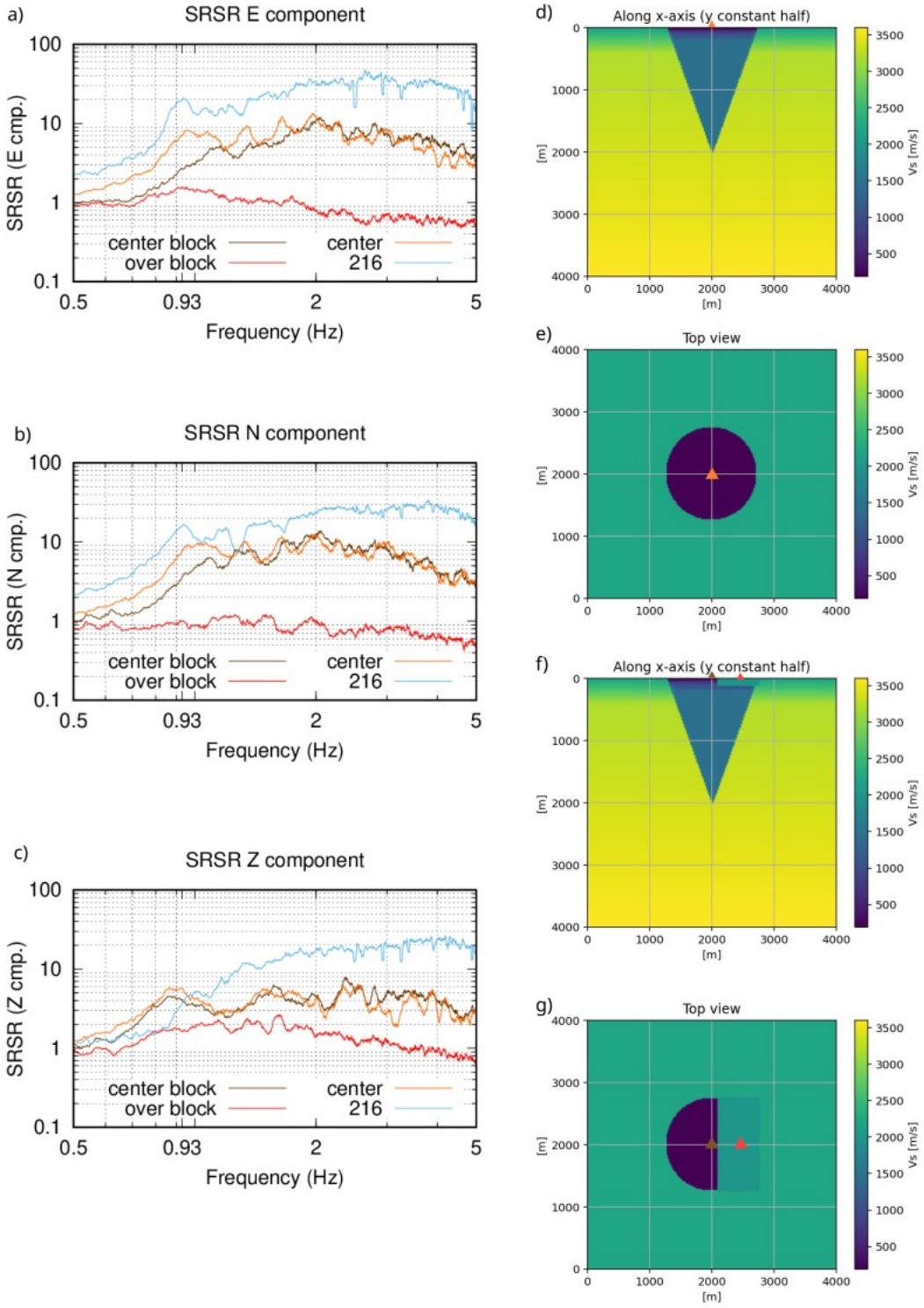


Figure 4.9 a) – c) Comparison of SRSR for the synthetic seismogram: "center" – station shown as an orange triangle in the figure d) and e); synthetic seismogram "center block" marked by brown solid line, shown as a brown triangle in the figure f) and g); synthetic seismogram "over block" marked by red solid line, shown as a red triangle in the figure f) and g); and observed station 216, marked by solid blue line. d) Nežichov maar cross-section of the shear wave velocity model (Vs) in [m/s]. e) Nežichov maar top-down view of Vs [m/s]. f) Nežichov maar cross-section with overlying block showing Vs [m/s]. g) Nežichov maar top-down view of the model with overlying block, Vs [m/s].

216 and 107. In the second model, an additional evaluation point was placed at the center of the overlying high-velocity block, 300m along the y-axis from the central location, to assess the effects of the assumed volcanic effusion. This point shows no visible amplification in the studied frequency band (0.5–5Hz) on any component, while the central point exhibits a 0.1Hz upward shift in the amplification frequency compared to the first model (Figure4.9a–c). This is in agreement with field observations at stations 126–130 and 132, where no significant amplification is observed within the same frequency band over the high-resistivity rocks.

4.5 Discussion

The ambient seismic noise data, gravity survey, ERT results, and numerical modeling all support the interpretation of maar-type volcanic structures, particularly when compared with the well-documented Mýtina maar in West Bohemia (Flechsig et al., 2015; Labuta et al., 2023, 2025; Lied et al., 2020; Mrlina et al., 2007, 2009). At both hypothesized maar structures, peak amplifications corresponding to specific oscillation modes were observed at the same frequency across the entire structure, indicating resonance of a 3D body—similar to that observed at the Mýtina maar (Labuta et al., 2025). Similarly, elongated Alpine valleys often exhibit 2D resonance. In such cases, the cross-sectional width is comparable to the depth, and the valley geometry remains relatively uniform in the direction perpendicular to the cross-section. As a result, resonance frequencies tend to be consistent along the cross-section, with only minor variations across the valley (e.g., (Ermert et al., 2014)).

The seismic response of the Sepuska structure appears to be very similar to that of the Mýtina maar. The main difference lies in the broader lateral extent of the SRSR amplification of the fundamental modes, observed at 1.14 and 1.17 Hz, and in the sharp increase in shear-wave velocity at a depth of approximately 60m. This velocity contrast is interpreted as the boundary between sedimentary infill and underlying volcanic breccia. In contrast, the Mýtina maar shows a deeper sedimentary sequence, with borehole data indicating about 100m of unconsolidated deposits (Mrlina et al., 2009). The estimated radius of the Sepuska maar is approximately 350 m - roughly twice the size of Mýtina (Labuta et al., 2023, 2025).

The horizontal amplification pattern derived from SRSR is roughly circular, with a slight elongation toward the south. This asymmetry may be an artifact caused by the absence of a measurement point near the pond, where the maximum negative gravity anomaly was observed. If a station were installed in this area, we would expect the amplification pattern to show elongation consistent with the direction of particle motion determined from the 1.17Hz mode in the FDD analysis.

TFPA results for Sepuska indicate that the particle motion of the first two modes is oriented toward the center of the area with maximum amplification. The FDD results further support this interpretation by confirming the TFPA-based estimate of the maar center. Both of the first two modes exhibit a vertical polarization reversal near the center of the structure, with their inferred axes being roughly parallel. The intersection of these axes likely represents a center of

rotation for the third mode, observed at 1.28Hz. This point coincides with the location of the maximum SRSR amplification of the fundamental modes and the strongest negative gravity anomaly, supporting its interpretation as the center of the maar.

The maximum vertical SRSR amplification observed in the northern part of the structure, as well as the detailed shape of the horizontal amplification pattern, remain open questions and should be addressed in future studies.

The Nežichov depression exhibits characteristics typical of a maar-like volcanic structure, including a deep, crater-shaped morphology filled with low-density sediments. However, in contrast to the Sepuska and Mýtina maars, the seismic and gravimetric responses at Nežichov suggest a more complex internal structure and evolution.

Despite this complexity, resonance effects are clearly observed in the ambient seismic noise data. The SRSR analysis reveals well-defined amplification peaks at frequencies of 0.88Hz and 0.93Hz, corresponding to the fundamental oscillation modes. These values are comparable to those identified at Sepuska and Mýtina, indicating the presence of a similarly resonant 3D body. The amplification pattern is spatially coherent, but its center does not coincide with the center of the negative gravity anomaly. Instead, the maximum amplification occurs in an area displaced eastward from the gravimetric low. Interestingly, the center of the gravity anomaly lies in a zone with very low observed amplification.

The TFPA results at Nežichov support the interpretation of the amplification center based on SRSR data. Particle motion directions for the first two modes are consistently oriented toward the area of strongest amplification, rather than toward the gravity minimum. This is further supported by the FDD results, which agree with both TFPA and SRSR observations in identifying the amplification center. However, in contrast to the clearer separation of mode shapes observed at Sepuska and Mýtina, the first and second modes at Nežichov appear to have very similar polarization patterns. This may indicate a less well-defined internal layering or structural irregularities that modify the modal response of the system. Moreover, the SRSR results show slight differences between the two surveys. For instance, station 207, which recorded during the day and was placed at the exact same location as station 107 (recorded during the night), showed an amplification ratio of 13.5 on both horizontal components and 2.5 on the vertical component. In contrast, the nighttime recording at station 107 showed lower amplification ratios of 9 on the horizontal and 2 on the vertical component. These differences may reflect variations in ambient noise sources. It is worth noting that the villages of Branišov and Nežichov are situated near the edge of the depression.

Comparison of the two ERT profiles provides valuable insight into the volcanic evolution of the Nežichov structure. The surface-reaching intrusion R2, located on the slope of the depression, likely represents the earliest intrusive phase—possibly emplaced before the formation of the main outer rim of the maar, when the surface was still relatively flat. Subsequently, the center of the structure may have subsided, or alternatively, a later intrusion (R1) may have uplifted the outer parts of the maar.

Profile P2, positioned along the edge of the presumed maar, reveals a thinner sequence of maar lake sediments (C3) compared to profile P1 (C2), and their lateral extent is also more limited. This observation is consistent with the expected

geometry of a maar, where sediment thickness decreases toward the rim.

Resistivities associated with anomalies R1 and R3 are assumed to represent similar materials forming parts of the outer rim. However, R3 exhibits notably higher resistivity values, more typical of trachyandesite. This discrepancy may be explained by hydrogeological conditions: the sediments in profile P1 (C1) are significantly thicker and closer to the rim, likely allowing for greater groundwater accumulation. The presence of groundwater could reduce the resistivity of R1 by penetrating fissures and cracks within the rock mass.

To explore the influence of the Nežichov maar's geometry on its seismic response, we developed a simplified numerical model approximating the structure as a conical body. The cone was designed with a diameter of 1500m and a depth of 2000m, parameters chosen to replicate the observed amplification ratios of both horizontal and vertical components within the fundamental resonance frequency band of 0.9–0.95Hz. This geometry results in a slope angle of approximately 70–75°, consistent with observed slopes at the Bažina maar (Hrubcová et al., 2023) and with numerical modeling results for the Mýtina maar (Labuta et al., 2023).

While this simplified conical model successfully reproduces the general resonance behavior observed in the seismic data, it fails to account for the absence of amplification in the western part of the structure—specifically in the area corresponding to the gravimetric minimum. To address this discrepancy, we tested the hypothesis of a secondary effusive or intrusive body intersecting the maar, as suggested by the ERT results. By introducing a high-velocity, laterally extensive block—representing the effusive material—into the model, we were able to reproduce two key observations: (1) preservation of the SRSR amplification ratios and frequencies in the central part of the structure, and (2) suppression of amplification across the high-velocity block.

This outcome supports the interpretation that the western zone of the maar is underlain by a dense volcanic intrusion or effusion, which dampens resonance effects by altering local impedance contrasts and wave propagation paths. The modeling thus provides an important link between the observed amplification asymmetry, the gravity anomaly, and the high-resistivity zone imaged in the ERT data, reinforcing the hypothesis of a complex, multi-phase volcanic evolution at Nežichov.

4.6 Conclusion

We confirmed the initial hypothesis of the existence of maar-type volcanic structures in the vicinity of the trachyandesite effusion of Třebouňský vrch in West Bohemia, Czechia. The investigated depressions—Sepuska and Nežichov—were analyzed using ambient seismic noise, gravimetric surveys, and electrical resistivity tomography (ERT).

Ambient vibration surveys at both sites revealed identical fundamental-mode amplification frequencies across each structure on both horizontal and vertical components, with spatial variation in amplitude. This pattern is characteristic of 3D resonance, consistent with observations at the Mýtina maar (Labuta et al., 2025), and supports the interpretation of both Sepuska and Nežichov as maar-type volcanic structures.

The Sepuska maar, located east of Sepuska hill and approximately 1km south

of Nežichov, exhibits SRSR results similar to those observed at Mýtina. The lower fundamental-mode frequency at Sepuska suggests larger lateral and vertical dimensions. These findings are corroborated by the gravity data, which reveal a broad negative anomaly consistent with a deep sediment-filled crater.

The Nežichov maar, located southeast of Třebouňský vrch, exhibits a more complex internal structure. The maximum SRSR amplification is spatially offset from the gravimetric minimum, indicating that the seismic and gravity signals reflect different subsurface features. F-K analysis suggests only a thin layer of lake sediments near the surface, and ERT revealed a volcanic effusion intruding through the maar fill in the western part of the structure. This effusive body likely suppresses amplification locally. Numerical modeling incorporating this high-velocity zone reproduced both the suppression of SRSR amplification and the overall resonance pattern. A simplified conical model suggests the maar is approximately 1500m in diameter and at least 2000m deep, consistent with the extent of both the amplification zone and the gravity anomaly.

These results highlight the value of combining seismic, gravimetric, and electrical methods to resolve the internal structure of maar-diatreme systems. Further investigations, including borehole data or denser seismic arrays, would help refine interpretations of the internal architecture and volcanic evolution of these features.

5 Concluding remarks and Future Directions

This thesis presents the first documented evidence of 3D resonance occurring in maar volcanic infills, expanding our understanding of their seismic response characteristics and a possible way how to model their structural properties. The well-documented Mýtina maar (Flechsig et al., 2015; Lied et al., 2020; Mrlina et al., 2007, 2009) served as a reference case for us (Chapter 2 and 3), on which the methods were first tested and validated. The results from Mýtina (Chapters 2, 3) were then used as a comparative framework for less studied structures in the region—specifically Sepuska and Nežichov maars (Chapter 4). Moreover, the seismic noise was acquired at Bažina, Ztracený rybník, and Neualbenreuth maars. While a detailed analysis of these sites lies beyond the scope of this thesis, we provide a brief overview in this section to illustrate that our observations are more general in nature and not limited to one or two specific locations. While the actual measurements at these sites are significantly denser, we present only representative examples here. Overview maps are shown in Figure 5.1 to illustrate the dimensions and terrain morphology of the sites. Figure 5.2 displays site-to-reference spectral ratio results for a representative receiver pair, located approximately at the center of the maar and at the reference site. At each site, all measuring stations installed within the structure exhibited resonance at identical frequencies (not shown here), indicating a strong three-dimensional resonance effect specific to that site. When excited by incoming ambient noise, the maar body vibrates as an entire structure, including the shallow sedimentary layers. This phenomenon highlights the significant role of the maar's morphology and internal architecture in shaping its response.

The fundamental resonance frequencies differ across the studied sites, ranging approximately from 0.6 to 2 Hz. These variations reflect differences in the geometry and internal structure of each maar. In Figure 5.2, the sites are arranged from top to bottom in order of decreasing fundamental frequency, providing a clear visual comparison of their resonance characteristics. For all sites, we recorded significant amplification of ground motion within the maars, for both the horizontal and vertical components. This amplification reached up to 100 times the original amplitude for one of the sites (Figure 5.2), which can be considered an extreme case. Such high amplification levels have previously been observed only in buildings, slender rock formations (Müller & Burjánek, 2023), or unstable slopes (Kleinbrod et al., 2017) —that is, in structures with very specific geometries. The amplification levels based on seismic noise might be biased in general (Perron et al., 2018). Nevertheless, when these results were compared with amplification observed during earthquake recordings at Mýtina (Figure 3.4), the resonance amplitudes matched closely. This supports that the SRSR method, based on seismic noise, can reliably predict the maar's response to earthquake excitation. The frequency and amplitude of the observed resonance modes primarily depend on the shape, size, and seismic velocities of the maar infills. This relationship can be used to constrain the depth and width of the infills. However, these dependencies are not straightforward. For example, it is not generally true that larger structures exhibit

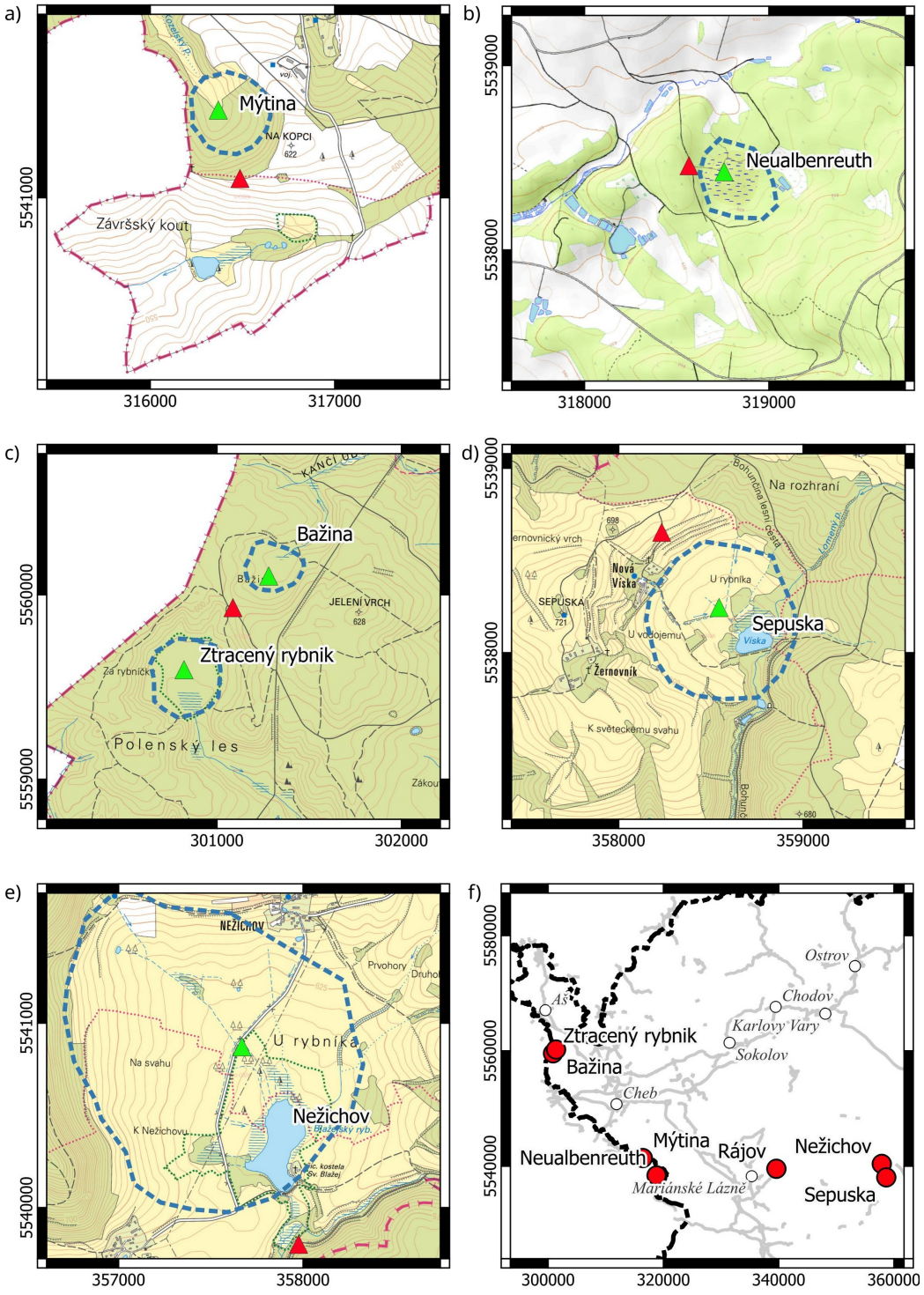


Figure 5.1 Local maps of studied maar volcanoes. Red triangle denotes the reference station, green triangle then station located within the maar structure. Blue dashed line denotes an approximate area of each maar. All maps are in the same scale and a coordinate system WGS 84 / UTM zone 33N, EPSG:32633. Base map: Basic topographic map ČR 1:25 000 by State Administration of Land Surveying and Cadastre, except Neualbenreuth – here we use OpenTopoMap.org a) Mýtina maar, b) Neualbenreuth maar, c) Bažina and Ztracený rybník, d) Sepuska maar, e) Nežichov maar, f) Overview map of maars in West Bohemia.

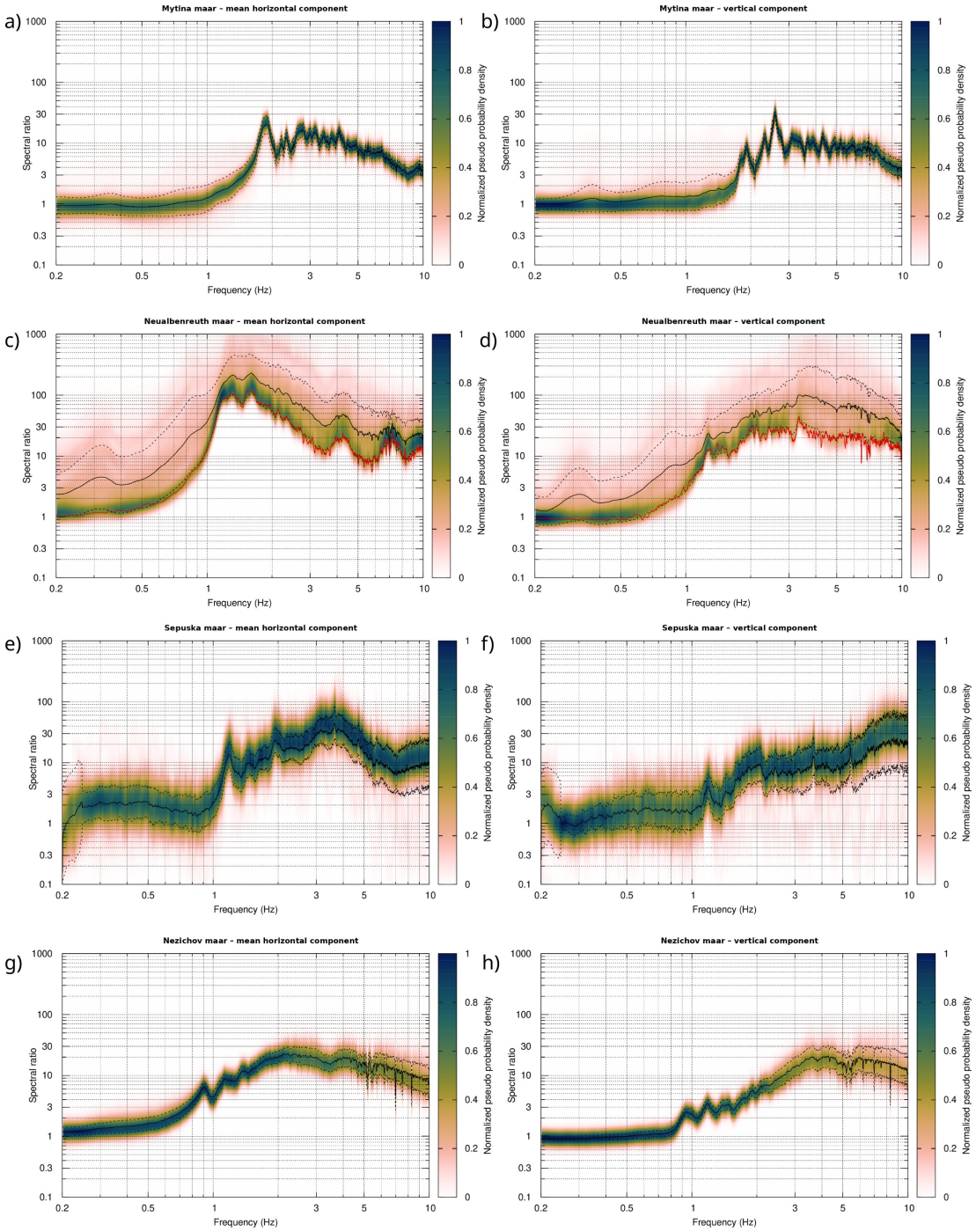


Figure 5.2 Cont'd.

lower fundamental frequencies. As illustrated in Figures 5.1 and 5.2, Ztracený rybník maar - despite having significantly smaller lateral dimensions than Nežichov or Sepuska maars - exhibits a lower fundamental frequency. This can be attributed to its distinct velocity structure, which includes an extremely soft peat layer (not shown here) that strongly influences the resonance characteristics. Constraining the geometry of the maars, particularly their depth, would require not only detailed measurements of shear-wave velocities but, more importantly, numerical modeling to account for the complex relationship between structural form and material properties. Numerical simulations using a viscoelastic cone-shaped model with

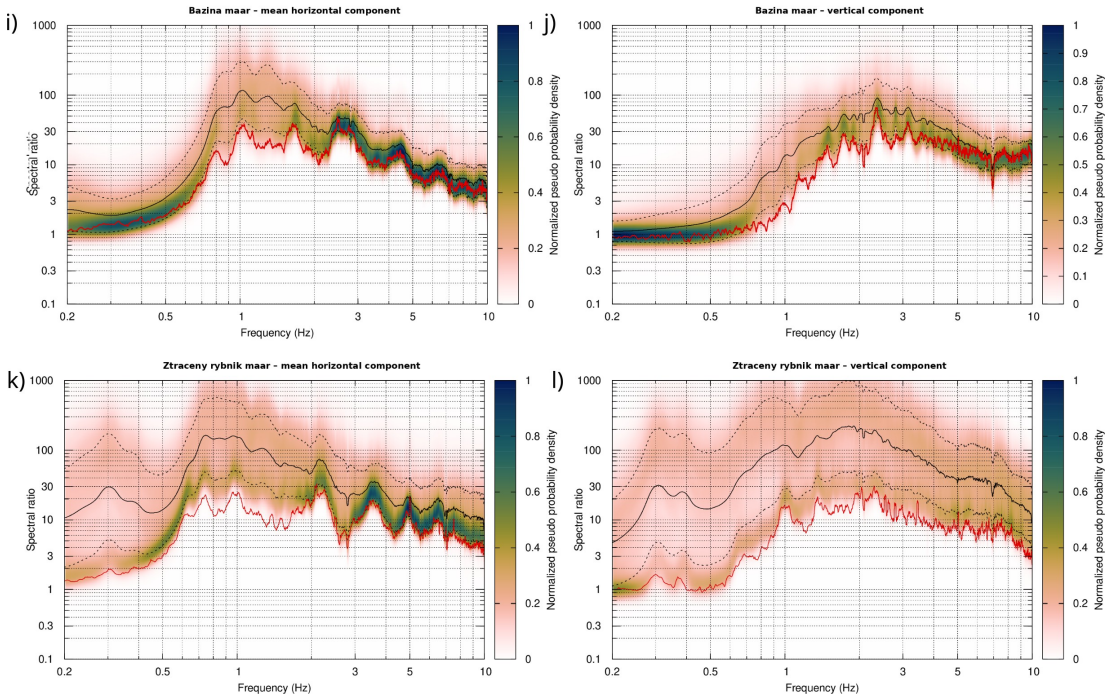


Figure 5.2 SRSR estimate based on a long-term deployment (one month, but only one day for Sepuska) measurements in selected maars. Black line denotes mean observed amplification ratio. Dashed lines constrain the interval of one standard deviation. Solid red line shows minimal observed amplification ratio from 1-hour of recordings in the maar with a peat layer, when the atmospheric conditions were favorable. The color scale describes the probability of observed amplification ratio from hourly recordings. i.e. normalized probability density function. Left column represents geometrical mean of the horizontal components (further abbreviated as X), the right column is vertical component (abbreviated as V). a) Mýtina X, b) Mýtina Z, c) Neualbenreuth X, d) Neualbenreuth Z, e) Ztracený rybník X, f) Ztracený rybník Z, g) Bažina X, h) Bažina Z.

material damping demonstrated that both the frequency and amplitude of the observed amplification could be realistically reproduced. The strongly reduced amplification observed in part of the Nežichov maar required more complex modeling to explain the observations. This was achieved by incorporating a volcanic intrusion in the central part of the structure, which disrupts the otherwise coherent resonance seen in the other maar craters. The presence of this intrusion, effectively sealing the sediments and limiting their resonant response, was later confirmed by Electrical Resistivity Tomography (ERT). In general, for maar infills containing additional volcanic intrusions—such as Rájov maar (Valenta et al., 2014) —a more complex resonance response can be expected.

A consistently observed phenomenon in all studied maar bodies is the splitting of the fundamental resonance mode into two distinct peaks. This effect is also apparent on the vertical component of the seismic signal as a broadening or doubling of the SRSR peak. This splitting is likely caused by the fact that the craters are not perfect circles but slightly elliptical, as also indicated by systematic geomorphological studies of maars (Graettinger, 2018). This interpretation is further supported by numerical modeling presented in this thesis (Chapters 1,2,3,4). The degree of ellipticity can likely be estimated from the ratio of the two resonant

frequencies, providing a potential quantitative supplement to the systematic geomorphological observations.

We propose the ambient vibration survey as a cheap and powerful method for the identification of maar structures, complementary to standard geophysical methods. We demonstrated the capability of the Site-to-Reference Spectral Ratio (SRSR) method to identify maar structures based on seismic noise. SRSR is a relatively inexpensive and not demanding method, both in station deployment, where, in principle, we only need 2 stations to jointly record seismic noise. The processing is also very straightforward, as only ratio of the Fourier spectra of the station located on the surface of the studied geological structure to the spectra of a nearby reference station is required. In cases where a high number of synchronously recording stations are available, Frequency Domain Decomposition (FDD) can be used in addition to retrieve the phase and shape of the resonance modes. In our case, this approach successfully imaged, for example, a torsional mode at the Mýtina maar.

Special attention must be given to sites containing a peat layer, as it can distort the measurements. These sites show a large scatter in the observed SRSR values, as illustrated in Figure 5.2 c – h (sites Ztracený rybník, Bažina, and Neualbenreuth in our dataset). Preliminary analysis suggests that trees rooted in the soft peat significantly affect the measurements. Across the entire frequency range investigated using the SRSR method, wind-speed-modulated effects were observed. Notably, peaks between 0.2 and 0.5 Hz were detected (Figure 5.2), most likely caused by the swaying of trees rooted in the peat. However, this interpretation requires further dedicated study, which is left for future work. Based on our experience, we recommend that ambient vibration measurements at such sites be conducted only during calm, windless nights to minimize this environmental noise. Nevertheless, a detailed analysis of the seismic response of maars containing a peat layer, as well as a more general comparative study based on a larger set of maars, is beyond the scope of this thesis and is left for future research.

Bibliography

Aki, K., & Richards, P. G. (2002). *Quantitative seismology* (2nd ed.). University Science Books.

Andreani, L., Stanek, K. P., Gloaguen, R., Krentz, O., & Domínguez-González, L. (2014). Dem-based analysis of interactions between tectonics and landscapes in the Ore Mountains and Eger Rift (East Germany and NW Czech Republic). *Remote Sensing*, *6*(9), 7971–8001.

Ashford, S. A., Sitar, N., Lysmer, J., & Deng, N. (1997). Topographic effects on the seismic response of steep slopes. *Bulletin of the seismological society of America*, *87*(3), 701–709.

Assimaki, D., Li, W., Steidl, J. H., & Tsuda, K. (2008). Site amplification and attenuation via downhole array seismogram inversion: A comparative study of the 2003 Miyagi-Oki aftershock sequence. *Bulletin of the Seismological Society of America*, *98*(1), 301–330.

Babuška, V., Plomerová, J., & Fischer, T. (2007). Intraplate seismicity in the western Bohemian Massif (central Europe): A possible correlation with a paleoplate junction. *Journal of Geodynamics*, *44*(3-5), 149–159.

Babuška, V., Růžek, B., & Dolejš, D. (2016). Origin of earthquake swarms in the western Bohemian Massif: Is the mantle CO2 degassing, followed by the Cheb Basin subsidence, an essential driving force? *Tectonophysics*, *668*, 42–51.

Bankwitz, P., Schneider, G., Kämpf, H., & Bankwitz, E. (2003). Structural characteristics of epicentral areas in Central Europe: Study case Cheb Basin (Czech Republic). *Journal of Geodynamics*, *35*(1-2), 5–32.

Bard, P.-Y., et al. (1999). Microtremor measurements: A tool for site effect estimation. *The effects of surface geology on seismic motion*, *3*, 1251–1279.

Blecha, V., Fischer, T., Táborík, P., Vilhem, J., Klanica, R., Valenta, J., & Štěpančíková, P. (2018). Geophysical evidence of the eastern marginal fault of the Cheb basin (Czech Republic). *Studia Geophysica et Geodaetica*, *62*(4), 660–680.

Bonnefoy-Claudet, S., Cotton, F., & Bard, P.-Y. (2006). The nature of noise wavefield and its applications for site effects studies: A literature review. *Earth-Science Reviews*, *79*(3-4), 205–227.

Borcherdt, R. D. (1970). Effects of local geology on ground motion near San Francisco Bay. *Bulletin of the Seismological Society of America*, *60*(1), 29–61.

Borcherdt, R. D. (1994). Estimates of site-dependent response spectra for design (methodology and justification). *Earthquake spectra*, *10*(4), 617–653.

Bottelin, P., Levy, C., Baillet, L., Jongmans, D., & Gueguen, P. (2013). Modal and thermal analysis of Les Arches unstable rock column (Vercors massif, French Alps). *Geophysical Journal International*, *194*(2), 849–858.

Brand, B. D., Mackaman-Lofland, C., Pollock, N. M., Bendaña, S., Dawson, B., & Wichgers, P. (2014). Dynamics of pyroclastic density currents: Conditions that promote substrate erosion and self-channelization—Mount St Helens, Washington (USA). *Journal of Volcanology and Geothermal Research*, *276*, 189–214.

Brandl, P. A., Genske, F. S., Beier, C., Haase, K. M., Sprung, P., & Krumm, S. H. (2015). Magmatic evidence for carbonate metasomatism in the lithospheric mantle underneath the Ohře (Eger) Rift. *Journal of Petrology*, *56*(9), 1743–1774.

Brauer, A., Endres, C., Günter, C., Litt, T., Stebich, M., & Negendank, J. F. (1999). High resolution sediment and vegetation responses to Younger Dryas climate change in varved lake sediments from Meerfelder Maar, Germany. *Quaternary Science Reviews*, *18*(3), 321–329.

Brincker, R., & Ventura, C. (2015). *Introduction to operational modal analysis*. John Wiley Sons.

Brincker, R., Ventura, C. E., & Andersen, P. (2001). Damping estimation by frequency domain decomposition. *Proceedings of IMAC 19: A conference on structural dynamics: Februar 5-8, 2001, Hyatt Orlando, Kissimmee, Florida, 2001*, 698–703.

Burjánek, J., Gassner-Stamm, G., Poggi, V., Moore, J. R., & Fäh, D. (2010). Ambient vibration analysis of an unstable mountain slope. *Geophysical Journal International*, *180*(2), 820–828.

Burjánek, J., Kleinbrod, U., & Fäh, D. (2019). Modeling the seismic response of unstable rock mass with deep compliant fractures. *Journal of Geophysical Research: Solid Earth*, *124*(12), 13039–13059.

Burjánek, J., Moore, J. R., Yugsi Molina, F. X., & Fäh, D. (2012). Instrumental evidence of normal mode rock slope vibration. *Geophysical Journal International*, *188*(2), 559–569.

Cajz, V., & Valečka, J. (2010). Tectonic setting of the Ohře/Eger Graben between the central part of the české středohoří Mts. and the Most Basin, a regional study. *Journal of Geosciences*, *55*(3), 201–215.

Campbell, K. W. (2009). Estimates of shear-wave Q and κ 0 for unconsolidated and semiconsolidated sediments in Eastern North America. *Bulletin of the Seismological Society of America*, *99*(4), 2365–2392.

Capon, J. (1969). High-resolution frequency-wavenumber spectrum analysis. *Proceedings of the IEEE*, *57*(8), 1408–1418.

Cas, R., & Wright, J. (1987). Volcanic successions: Ancient and modern. *Allen and Unin, London*.

Chaloupský, J. (1989). Major tectonostratigraphic units of the Bohemian Massif.

Comina, C., Motta, M., Muzzolon, W., Vagnon, F., & Vergnano, A. (2024). Challenging underground geophysical, geological and topographical surveys in the Borna Maggiore di Pugnetto karst collapse cave to delineate its genesis and actual structure. *Earth Surface Processes and Landforms*, *49*(15), 5390–5405.

Cox, B. R., & Teague, D. P. (2016). Layering ratios: A systematic approach to the inversion of surface wave data in the absence of a priori information. *Geophysical Journal International*, *207*(1), 422–438.

Dahlen, F., & Tromp, J. (1999). *Theoretical global seismology*. Princeton university press.

Dahm, T., Stiller, M., Mechie, J., Heimann, S., Hensch, M., Woith, H., Schmidt, B., Gabriel, G., & Weber, M. (2020). Seismological and geophysical signatures of the deep crustal magma systems of the Cenozoic volcanic fields

beneath the Eifel, Germany. *Geochemistry, Geophysics, Geosystems*, *21*(9), e2020GC009062.

Dellino, P., De Astis, G., La Volpe, L., Mele, D., & Sulpizio, R. (2011). Quantitative hazard assessment of phreatomagmatic eruptions at Vulcano (Aeolian Islands, Southern Italy) as obtained by combining stratigraphy, event statistics and physical modelling. *Journal of Volcanology and Geothermal Research*, *201*(1-4), 364–384.

Dèzes, P., Schmid, S. M., & Ziegler, P. A. (2004). Evolution of the European Cenozoic Rift System: Interaction of the Alpine and Pyrenean orogens with their foreland lithosphere. *Tectonophysics*, *389*(1-2), 1–33.

Dobry, R., Oweis, I., & Urzua, A. (1976). Simplified procedures for estimating the fundamental period of a soil profile. *Bulletin of the Seismological Society of America*, *66*(4), 1293–1321.

Downes, H. (1987). Tertiary and quaternary volcanism in the Massif Central, France. *Geological Society, London, Special Publications*, *30*(1), 517–530.

Eisner, L., & Clayton, R. W. (2001). A reciprocity method for multiple-source simulations. *Bulletin of the Seismological Society of America*, *91*(3), 553–560.

Ellis, R., & Oldenburg, D. (1994). Applied geophysical inversion. *Geophysical Journal International*, *116*(1), 5–11.

Ermert, L., Poggi, V., Burjánek, J., & Fäh, D. (2014). Fundamental and higher two-dimensional resonance modes of an Alpine valley. *Geophysical Journal International*, *198*(2), 795–811.

Fiala, J., & Vejnar, Z. (1997). The Cheb-Dylen Crystalline Unit, relations to the Moldanubian Zone. *Geologic Model of Western Bohemia related to the KTB borehole in Germany. J. Geol. Sci., Geology*, *47*, 56–57.

Field, E. H., & Jacob, K. H. (1995). A comparison and test of various site-response estimation techniques, including three that are not reference-site dependent. *Bulletin of the seismological society of America*, *85*(4), 1127–1143.

Fischer, T., Horálek, J., Hrubcová, P., Vavryčuk, V., Bräuer, K., & Kämpf, H. (2014). Intra-continental earthquake swarms in West-Bohemia and Vogtland: A review. *Tectonophysics*, *611*, 1–27.

Fischer, T., Štěpančíková, P., Karousová, M., Tábořík, P., Flechsig, C., & Gaballah, M. (2012). Imaging the Mariánské Lázně Fault (Czech Republic) by 3-D ground-penetrating radar and electric resistivity tomography. *Studia Geophysica et Geodaetica*, *56*(4), 1019–1036.

Flechsig, C., Heinicke, J., Mrlina, J., Kämpf, H., Nickschick, T., Schmidt, A., Bayer, T., Günther, T., Rücker, C., Seidel, E., et al. (2015). Integrated geophysical and geological methods to investigate the inner and outer structures of the Quaternary Mýtina maar (W-Bohemia, Czech Republic). *International Journal of Earth Sciences*, *104*(8), 2087–2105.

Gebhardt, A., De Batist, M., Niessen, F., Anselmetti, F. S., Ariztegui, D., Haberzettl, T., Kopsch, C., Ohlendorf, C., & Zolitschka, B. (2011). Deciphering lake and maar geometries from seismic refraction and reflection surveys in Laguna Potrok Aike (southern Patagonia, Argentina). *Journal of volcanology and geothermal research*, *201*(1-4), 357–363.

Graettinger, A. (2018). Trends in maar crater size and shape using the global Maar Volcano Location and Shape (MaarVLS) database. *Journal of Volcanology and Geothermal Research*, *357*, 1–13.

Graves, R. W., Pitarka, A., & Somerville, P. G. (1998). Ground-motion amplification in the Santa Monica area: Effects of shallow basin-edge structure. *Bulletin of the Seismological Society of America*, *88*(5), 1224–1242.

Häusler, M., Michel, C., Burjanek, J., & Fäh, D. (2021). Monitoring the Preonzo rock slope instability using resonance mode analysis. *Journal of Geophysical Research: Earth Surface*, *126*(4), e2020JF005709.

Häusler, M., Michel, C., Burjánek, J., & Fäh, D. (2019). Fracture network imaging on rock slope instabilities using resonance mode analysis. *Geophysical Research Letters*, *46*(12), 6497–6506.

Havíř, J., et al. (2005). Orientations of the principal paleostresses in the Western Bohemia seismoactive region and their comparison with recent stresses. *J. Czech. Geol. Soc*, *50*, 133–143.

Hensch, M., Dahm, T., Ritter, J., Heimann, S., Schmidt, B., Stange, S., & Lehmann, K. (2019). Deep low-frequency earthquakes reveal ongoing magmatic recharge beneath Laacher See Volcano (Eifel, Germany). *Geophysical Journal International*, *216*(3), 2025–2036.

Hessen, D. O., Andersen, T., Armstrong McKay, D., Kosten, S., Meerhoff, M., Pickard, A., & Spears, B. (2023). Lake ecosystem tipping points and climate feedbacks. *Earth System Dynamics Discussions*, *2023*, 1–34.

Hobiger, M., Bergamo, P., Imperatori, W., Panzera, F., Marrios Lontsi, A., Perron, V., Michel, C., Burjánek, J., & Fäh, D. (2021). Site characterization of Swiss strong-motion stations: The benefit of advanced processing algorithms. *Bulletin of the Seismological Society of America*, *111*(4), 1713–1739.

Holub, F. V., Rapprich, V., Erban, V., Pecskay, Z., Mlcoch, B., & Mikova, J. (2010). Petrology and geochemistry of the Tertiary alkaline intrusive rocks at Doupov, Doupovské hory Volcanic Complex (NW Bohemian Massif). *Journal of Geosciences*, *55*(3), 251–278.

Horálek, J., & Fischer, T. (2008). Role of crustal fluids in triggering the West Bohemia/Vogtland earthquake swarms: Just what we know (a review). *Studia Geophysica et Geodaetica*, *52*(4), 455–478.

Horálek, J., Fischer, T., Boušková, A., & Jedlička, P. (2000). The Western Bohemia/Vogtland region in the light of the WEBNET network. *Studia geophysica et geodaetica*, *44*(2), 107–125.

Hrubcová, P., Fischer, T., Rapprich, V., Valenta, J., Táborík, P., Mrlina, J., Dahm, T., Vylita, T., Beránek, R., Klanica, R., et al. (2023). Two small volcanoes, one inside the other: Geophysical and drilling investigation of Bažina maar in western Eger Rift. *Earth and Space Science*, *10*(8), e2023EA003009.

Hrubcová, P., Geissler, W. H., Bräuer, K., Vavryčuk, V., Tomek, Č., & Kämpf, H. (2017). Active magmatic underplating in western Eger rift, central Europe. *Tectonics*, *36*(12), 2846–2862.

Irikura, K., & Kawanaka, T. (1980). Characteristics of microtremors on ground with discontinuous underground structure. *Bulletin of the Disaster Prevention Research Institute*, *30*(3), 81–96.

Jousset, P., Haberland, C., Bauer, K., & Arnason, K. (2011). Hengill geothermal volcanic complex (Iceland) characterized by integrated geophysical observations. *Geothermics*, *40*(1), 1–24.

Kämpf, H., Peterek, A., Rohrmüller, J., Kümpel, H., Geissler, W., Koch, R., & Röhling, H. (2005). The KTB deep crustal laboratory and the western Eger Graben. *GeoErlangen 2005: System Earth-Biosphere Coupling/Regional Geology of Central Europe (Erlangen 2005)*.

Kašing, M., Jirásek, J., Matỳsek, D., Valenta, J., Rapprich, V., Táborík, P., & Pek, T. (2025). Almost eroded but still there: Oldest diatreme volcanoes of prequaternary age in the eastern Bohemian Massif, Czechia. *Geomorphology*, *475*, 109668.

Kawase, H. (1996). The cause of the damage belt in Kobe:"The basin-edge effect," constructive interference of the direct S-wave with the basin-induced diffracted/Rayleigh waves. *Seismological Research Letters*, *67*(5), 25–34.

Kawase, H., & Aki, K. (1989). A study on the response of a soft basin for incident S, P, and Rayleigh waves with special reference to the long duration observed in Mexico City. *Bulletin of the Seismological Society of America*, *79*(5), 1361–1382.

Kleinbrod, U., Burjánek, J., & Fäh, D. (2017). On the seismic response of instable rock slopes based on ambient vibration recordings. *Earth, Planets and Space*, *69*(1), 126.

Komatitsch, D., Ritsema, J., & Tromp, J. (2002). The spectral-element method, Beowulf computing, and global seismology. *Science*, *298*(5599), 1737–1742.

Konno, K., & Ohmachi, T. (1998). Ground-motion characteristics estimated from spectral ratio between horizontal and vertical components of microtremor. *Bulletin of the Seismological Society of America*, *88*(1), 228–241.

Kopecký, L. (1978). Neoidic taphrogenic evolution and young alkaline volcanism of the Bohemian Massif. *Sborník geologických věd. Geologie*, (31), 91–107.

Kühn, D., Ohrnberger, M., & Dahm, T. (2011). Imaging a shallow salt diapir using ambient seismic vibrations beneath the densely built-up city area of Hamburg, Northern Germany. *Journal of seismology*, *15*(3), 507–531.

Labuta, M., Opršal, I., & Burjánek, J. (2023). Modelling the seismic response of the Mýtina maar volcanic structure. *Earth, Planets and Space*, *75*(1), 80.

Labuta, M., Opršal, I., Landa, D.-A., & Burjánek, J. (2025). Ambient vibrations of a deep maar resonator. *Soil Dynamics and Earthquake Engineering*, *188*, 109072.

Lachetl, C., & Bard, P.-Y. (1994). Numerical and theoretical investigations on the possibilities and limitations of Nakamura's technique. *Journal of Physics of the Earth*, *42*(5), 377–397.

Lied, P., Kontny, A., Nowaczyk, N., Mrlina, J., & Kämpf, H. (2020). Cooling rates of pyroclastic deposits inferred from mineral magnetic investigations: a case study from the Pleistocene Mýtina Maar (Czech Republic). *International Journal of Earth Sciences*, *109*(5), 1707–1725.

Linnemann, U. (2007). Ediacaran rocks from the Cadomian basement of the Saxo-Thuringian Zone (NE Bohemian Massif, Germany): Age constraints, geotectonic setting and basin development.

Lirer, F., Sprovieri, M., Ferraro, L., Vallefuoco, M., Capotondi, L., Cascella, A., Petrosino, P., Insinga, D., Pelosi, N., Tamburrino, S., et al. (2013).

Integrated stratigraphy for the Late Quaternary in the eastern Tyrrhenian Sea. *Quaternary International*, *292*, 71–85.

Loke, M. H., & Barker, R. D. (1996). Rapid least-squares inversion of apparent resistivity pseudosections by a quasi-Newton method1. *Geophysical prospecting*, *44*(1), 131–152.

Lorenz, V. (1975). Formation of phreatomagmatic maar-diatreme volcanoes and its relevance to kimberlite diatremes. *Physics and Chemistry of The Earth*, *9*, 17–27.

Lorenz, V. (1985). Lorenz V. 1985. Maars and diatremes of phreatomagmatic origin, a review. Transactions of the Geological Society of South Africa, 88: 459-470. *Transactions - Geological Society of South Africa*, *88*, 459–470.

Lorenz, V. (1986). On the growth of maars and diatremes and its relevance to the formation of tuff rings. *Bulletin of volcanology*, *48*(5), 265–274.

Lorenz, V. (2003). Maar-diatreme volcanoes, their formation, and their setting in hard-rock or soft-rock environments. *Geolines*, *15*, 72–83.

Lorenz, V. (2007). Syn-and posteruptive hazards of maar–diatreme volcanoes. *Journal of Volcanology and Geothermal Research*, *159*(1-3), 285–312.

Macrì, P., Smedile, A., Minelli, L., Siravo, G., Caricchi, C., Scateni, B., Di Roberto, A., Re, G., Nicolosi, I., Caracciolo, F. D., et al. (2023). Setting the basis for a high-resolution record of the late Quaternary to present climate variability from Castiglione maar, central Italy: First results from AMUSED project. *Quaternary International*, *671*, 1–14.

Málek, J., Horálek, J., & Janský, J. (2005). One-dimensional qP-wave velocity model of the upper crust for the West Bohemia/Vogtland earthquake swarm region. *Studia geophysica et geodaetica*, *49*(4), 501–524.

Maranò, S., Hobiger, M., & Fäh, D. (2017). Retrieval of Rayleigh wave ellipticity from ambient vibration recordings. *Geophysical Journal International*, *209*(1), 334–352.

Maranò, S., Reller, C., Loeliger, H.-A., & Fäh, D. (2012). Seismic waves estimation and wavefield decomposition: Application to ambient vibrations. *Geophysical Journal International*, *191*(1), 175–188.

McCalpin, J., Ferrario, F., Figueiredo, P., Livio, F., Grützner, C., Pisarska-Jamroży, M., Quigley, M., Reicherter, K., Rockwell, T., Štěpančíková, P., et al. (2023). New developments in onshore paleoseismic methods, and their impact on Quaternary tectonic studies. *Quaternary International*, *664*, 59–76.

Merle, O., & Michon, L. (2001). The formation of the West European Rift; a new model as exemplified by the Massif Central area. *Bulletin de la Societé géologique de France*, *172*(2), 213–221.

Michel, C., Guéguen, P., El Arem, S., Mazars, J., & Kotronis, P. (2010). Full-scale dynamic response of an RC building under weak seismic motions using earthquake recordings, ambient vibrations and modelling. *Earthquake Engineering Structural Dynamics*, *39*(4), 419–441.

Mitchell, B. J., & Xie, J.-k. (1994). Attenuation of multiphase surface waves in the Basin and Range Province—III. Inversion for crustal anelasticity. *Geophysical Journal International*, *116*(2), 468–484.

Moczo, P., Kristek, J., Vavrycuk, V., Archuleta, R. J., & Halada, L. (2002). 3D heterogeneous staggered-grid finite-difference modeling of seismic motion

with volume harmonic and arithmetic averaging of elastic moduli and densities. *Bulletin of the Seismological Society of America*, *92*(8), 3042–3066.

Moore, J. R., Geimer, P. R., Finnegan, R., & Michel, C. (2019). Dynamic analysis of a large freestanding rock tower (Castleton Tower, Utah). *Bulletin of the Seismological Society of America*, *109*(5), 2125–2131.

Mrlina, J., Kämpf, H., Geissler, W., & Van den Bogaard, P. (2007). Assumed quaternary maar structure at the Czech/German border between Mytina and Neualbenreuth (western Eger rift, Central Europe): Geophysical, petrochemical and geochronological indications. *Z. geol. Wiss.*, *35*(4), 213–230.

Mrlina, J., Kämpf, H., Kroner, C., Mingram, J., Stebich, M., Brauer, A., Geissler, W., Kallmeyer, J., Matthes, H., & Seidl, M. (2009). Discovery of the first Quaternary maar in the Bohemian Massif, Central Europe, based on combined geophysical and geological surveys. *Journal of Volcanology and Geothermal Research*, *182*(1-2), 97–112.

Mrlina, J., Kämpf, H., Polák, V., & Seidl, M. (2019). Indikace dvou neznámých kvartérních maarových vulkánů u Libě v západních Čechách na základě gravimetrického průzkumu. *Zpravodaj Hnědé uhlí*, (2).

Mucciarelli, M., & Gallipoli, M. R. (2001). A critical review of 10 years of microtremor HVSR technique. *Bollettino di Geofisica Teorica ed Applicata*, *42*(3-4), 255–266.

Müller, J., & Burjánek, J. (2023). In situ estimation of effective rock elastic moduli by seismic ambient vibrations. *International Journal of Rock Mechanics and Mining Sciences*, *170*, 105459.

Nakamura, Y., & Samizo, M. (1989). Site effect evaluation of surface ground using strong motion records. *Proc. 20th JSCE Earthquake Eng. Symposium*, 133–136.

Nakamura, Y. (1996). Real-time information systems for seismic hazards mitigation UrEDAS, HERAS and PIC. *Quarterly Report-Rtri*, *37*(3), 112–127.

Nakamura, Y., et al. (2000). Clear identification of fundamental idea of Nakamura's technique and its applications. *Proceedings of the 12th world conference on earthquake engineering*, *2656*, 1–8.

Nogoshi, M. (1971). On the amplitude characteristics of microtremor, Part II. *Journal of the seismological society of Japan*, *24*, 26–40.

Okada, H. (2006). Theory of efficient array observations of microtremors with special reference to the SPAC method. *Exploration geophysics*, *37*(1), 73–85.

Olsen, K. (2000). Site amplification in the Los Angeles basin from three-dimensional modeling of ground motion. *Bulletin of the Seismological Society of America*, *90*(6B), S77–S94.

Perron, V., Gélis, C., Froment, B., Hollender, F., Bard, P.-Y., Cultrera, G., & Cushing, E. M. (2018). Can broad-band earthquake site responses be predicted by the ambient noise spectral ratio? Insight from observations at two sedimentary basins. *Geophysical Journal International*, *215*(2), 1442–1454.

Petersson, N. A., & Sjögreen, B. (2015). Wave propagation in anisotropic elastic materials and curvilinear coordinates using a summation-by-parts finite difference method. *Journal of Computational Physics*, *299*, 820–841.

Petersson, N., & Sjogreen, B. (2017). SW4, version 2.01 [software]. *Computational Infrastructure of Geodynamics, doi*, *10*.

Petronis, M., Valenta, J., Rapprich, V., Lindline, J., Heizler, M., van Wyk de Vries, B., Shields, S., Balek, J., Fojtíková, L., & Tábořík, P. (2018). Emplacement history of the Miocene Zebín Tuff Cone (Czech Republic) revealed from ground geophysics, anisotropy of magnetic susceptibility, paleomagnetic, and 40Ar/39Ar geochronology data. *Geochemistry, Geophysics, Geosystems*, *19*(10), 3764–3792.

Pischiutta, M., Fondriest, M., Demurtas, M., Magnoni, F., Di Toro, G., & Rovelli, A. (2017). Structural control on the directional amplification of seismic noise (Campo Imperatore, central Italy). *Earth and Planetary Science Letters*, *471*, 10–18.

Poggi, V., Ermert, L., Burjanek, J., Michel, C., & Fäh, D. (2014). Modal analysis of 2-D sedimentary basin from frequency domain decomposition of ambient vibration array recordings. *Geophysical Journal International*, *200*(1), 615–626.

Poggi, V., & Fäh, D. (2010). Estimating Rayleigh wave particle motion from three-component array analysis of ambient vibrations. *Geophysical Journal International*, *180*(1), 251–267.

Preiswerk, L. E., Michel, C., Walter, F., & Fäh, D. (2019). Effects of geometry on the seismic wavefield of Alpine glaciers. *Annals of Glaciology*, *60*(79), 112–124.

Prieto, G. A., Parker, R. L., & Vernon Iii, F. (2009). A Fortran 90 library for multitaper spectrum analysis. *Computers Geosciences*, *35*(8), 1701–1710.

Rajchl, M., Uličný, D., Grygar, R., & Mach, K. (2009). Evolution of basin architecture in an incipient continental rift: The Cenozoic Most Basin, Eger Graben (Central Europe). *Basin Research*, *21*(3), 269–294.

Rapprich, V., Valenta, J., Brož, M., Kadlecová, E., van Wyk de Vries, B., Petronis, M. S., & Rojík, P. (2019). A crucial site in the argument between Neptunists and Plutonists: Reopening of the Historical Adit in the Komorní hůrka (Kammerbühl) Volcano after 180 years. *Geoheritage*, *11*(2), 347–358.

Richter, P., & Stettner, G. (1993). Lithologische und geochemische Profilierung im Kambroordovizium des südlichen Waldsassener Schiefergebirges. *Geol. Bavarica*, *98*, 175–217.

Ritter, J. R., Jordan, M., Christensen, U. R., & Achauer, U. (2001). A mantle plume below the Eifel volcanic fields, Germany. *Earth and Planetary Science Letters*, *186*(1), 7–14.

Rohrmüller, J., Kämpf, H., Geiß, E., Großmann, J., Grun, I., Mingram, J., Mrlina, J., Plessen, B., Stebich, M., Veress, C., et al. (2018). Reconnaissance study of an inferred Quaternary maar structure in the western part of the Bohemian Massif near Neualbenreuth, NE-Bavaria (Germany). *International Journal of Earth Sciences*, *107*(4), 1381–1405.

Ross, P.-S., Carrasco Núñez, G., & Hayman, P. (2017). Felsic maar-diatreme volcanoes: A review. *Bulletin of Volcanology*, *79*(2), 20.

Rücker, C., Günther, T., & Wagner, F. M. (2017). PyGIMLi: An open-source library for modelling and inversion in geophysics. *Computers Geosciences*, *109*, 106–123.

Sambridge, M. (1999). Geophysical inversion with a neighbourhood algorithm—I. Searching a parameter space. *Geophysical journal international*, *138*(2), 479–494.

Sanchez-Sesma, F. J., & Luzon, F. (1995). Seismic response of three-dimensional alluvial valleys for incident P, S, and Rayleigh waves. *Bulletin of the Seismological Society of America*, *85*(1), 269–284.

Sato, H., Fehler, M. C., & Maeda, T. (2012). *Seismic wave propagation and scattering in the heterogeneous earth* (Vol. 496). Springer.

Schmincke, H.-U. (2004). *Volcanism* (Vol. 28). Springer Science Business Media.

Schmincke, H.-U., Park, C., & Harms, E. (1999). Evolution and environmental impacts of the eruption of Laacher See Volcano (Germany) 12,900 a BP. *Quaternary International*, *61*(1), 61–72.

Schulmann, K., Catalán, J. R., Lardeaux, J. M., Janoušek, V., & Oggiano, G. (2014). The Variscan orogeny: Extent, timescale and the formation of the European crust.

Schulmann, K., & Gayer, R. (2000). A model for a continental accretionary wedge developed by oblique collision: The NE Bohemian Massif. *Journal of the Geological Society*, *157*(2), 401–416.

Sebazungu, E. (2006). Investigations on maar-diatreme volcanoes by inversion of magnetic and gravity data from the Eifel area, Germany.

Sirocko, F., Dietrich, S., Veres, D., Grootes, P. M., Schaber-Mohr, K., Seelos, K., Nadeau, M.-J., Kromer, B., Rothacker, L., Röhner, M., et al. (2013). Multi-proxy dating of Holocene maar lakes and Pleistocene dry maar sediments in the Eifel, Germany. *Quaternary Science Reviews*, *62*, 56–76.

Sjögreen, B., & Petersson, N. A. (2012). A fourth order accurate finite difference scheme for the elastic wave equation in second order formulation. *Journal of Scientific Computing*, *52*(1), 17–48.

Skácelová, Z., Rapprich, V., Valenta, J., Hartvich, F., Šrámek, J., Radoň, M., Gaždová, R., Nováková, L., Kolínský, P., & Pecskay, Z. (2010). Geophysical research on structure of partly eroded maar volcanoes: Miocene Hnojnice and Oligocene Rychnov volcanoes (northern Czech Republic). *Journal of Geosciences*, *55*(4), 333–345.

Skilling, I. P., White, J. D., & McPhie, J. (2002). Peperite: A review of magma–sediment mingling. *Journal of Volcanology and Geothermal Research*, *114*(1-2), 1–17.

Spudich, P., Hellweg, M., & Lee, W. (1996). Directional topographic site response at Tarzana observed in aftershocks of the 1994 Northridge, California, earthquake: Implications for mainshock motions. *Bulletin of the Seismological Society of America*, *86*(1B), S193–S208.

Steidl, J. H., Tumarkin, A. G., & Archuleta, R. J. (1996). What is a reference site? *Bulletin of the Seismological Society of America*, *86*(6), 1733–1748.

Steininger, J. (1819). *Geognostische studien am Mittelrheine*. F. Kupferberg.

Štěpančíková, P., Fischer, T., Stemberk Jr, J., Nováková, L., Hartvich, F., & Figueiredo, P. M. (2019). Active tectonics in the Cheb Basin: Youngest documented Holocene surface faulting in Central Europe? *Geomorphology*, *327*, 472–488.

Tavsanoglu, U. N., Maleki, R., & Akbulut, N. (2015). Effects of Salinity on the Zooplankton Community Structure in Two Maar Lakes and One Freshwater Lake in the Konya Closed Basin, Turkey. *Ekoloji Dergisi*, *24*(94).

Tokimatsu, K., Shinzawa, K., & Kuwayama, S. (1992). Use of short-period microtremors for V s profiling. *Journal of Geotechnical Engineering*, *118*(10), 1544–1558.

Tomek, F., Černý, J., Lutovský, M., Pospíšil, L., Vitouš, P., Sokol, L., Danielová, E., & Hájková, Z. (2025). Did Forefather Czech know he was standing on a fossil lava lake? Revisiting the Oligocene říp Hill volcano, Bohemian Massif. *International Geology Review*, 1–23.

Tonica, J., Opletal, M., Cicha, I., & Cihelka, M. (1998). Geologická Mapa ČR.

Ulrych, J., Dostal, J., Hegner, E., Balogh, K., & Ackerman, L. (2008). Late Cretaceous to Paleocene melilitic rocks of the Ohře/Eger Rift in northern Bohemia, Czech Republic: Insights into the initial stages of continental rifting. *Lithos*, *101*(1-2), 141–161.

Ulrych, J., Lloyd, F. E., & Balogh, K. (2003). Age relations and geochemical constraints of Cenozoic alkaline volcanic series in W Bohemia: A review. *Geolines*, *15*, 168–180.

Valenta, J., Rapprich, V., Skácelová, Z., Gaždová, R., & Fojtiková, L. (2014). The newly discovered Neogene maar volcano near the Mariánské Lázně, Western Bohemia. *Acta Geodyn Geomater*, *11*, 107–116.

Valentine, G. A., & White, J. D. (2012). Revised conceptual model for maar-diatremes: Subsurface processes, energetics, and eruptive products. *Geology*, *40*(12), 1111–1114.

Vejnar, J. F.-.-Z. (2004). The lithology, geochemistry, and metamorphic gradation of the crystalline basement of the Cheb (Eger) Tertiary Basin, Saxothuringian Unit. *Bulletin of Geosciences*, *79*(1), 41–52.

Vespermann, D., & Schmincke, H.-U. (2000). Scoria cones and tuff rings. Academic press.

Vidale, J. E. (1986). Complex polarization analysis of particle motion. *Bulletin of the Seismological society of America*, *76*(5), 1393–1405.

Wathelet, M., Chatelain, J.-L., Cornou, C., Giulio, G. D., Guillier, B., Ohrnberger, M., & Savvaidis, A. (2020). Geopsy: A user-friendly open-source tool set for ambient vibration processing. *Seismological Research Letters*, *91*(3), 1878–1889.

Wathelet, M., Guillier, B., Roux, P., Cornou, C., & Ohrnberger, M. (2018). Rayleigh wave three-component beamforming: Signed ellipticity assessment from high-resolution frequency-wavenumber processing of ambient vibration arrays. *Geophysical Journal International*, *215*(1), 507–523.

Wathelet, M., Jongmans, D., & Ohrnberger, M. (2004). Surface-wave inversion using a direct search algorithm and its application to ambient vibration measurements. *Near surface geophysics*, *2*(4), 211–221.

Wathelet, M., Jongmans, D., Ohrnberger, M., & Bonnefoy-Claudet, S. (2008). Array performances for ambient vibrations on a shallow structure and consequences over V s inversion. *Journal of Seismology*, *12*(1), 1–19.

Weber, S., Beutel, J., Häusler, M., Geimer, P. R., Fäh, D., & Moore, J. R. (2022). Spectral amplification of ground motion linked to resonance of large-scale mountain landforms. *Earth and Planetary Science Letters*, *578*, 117295.

Weinlich, F., Bräuer, K., Kämpf, H., Strauch, G., Tesař, J., & Weise, S. (1999). An active subcontinental mantle volatile system in the western Eger rift, Central Europe: Gas flux, isotopic (He, C, and N) and compositional fingerprints. *Geochimica et Cosmochimica Acta*, *63*(21), 3653–3671.

White, J. D., & Ross, P. (2011). Maar-diatreme volcanoes: A review. *Journal of Volcanology and Geothermal Research*, *201*(1-4), 1–29.

Wohletz, K., & Heiken, G. (1992). *Volcanology and geothermal energy* (Vol. 432). University of California Press Berkeley.

Wood, C. A. (1980). Morphometric evolution of cinder cones. *Journal of Volcanology and Geothermal Research*, *7*(3-4), 387–413.

Závada, P., Dědeček, P., Mach, K., Lexa, O., & Potužák, M. (2011). Emplacement dynamics of phonolite magma into maar-diatreme structures—correlation of field, thermal modeling and AMS analogue modeling data. *Journal of volcanology and geothermal research*, *201*(1-4), 210–226.

Ziegler, P., & Dèzes, P. (2006). Crustal evolution of western and central Europe.

List of Publications

Labuta, M., Opršal, I., & Burjánek, J. (2023). Modelling the seismic response of the Mýtina maar volcanic structure. Earth, Planets and Space, 75 (1), 80.

Labuta, M., Opršal, I., Landa, D.-A., & Burjánek, J. (2025). Ambient vibrations of a deep maar resonator. Soil Dynamics and Earthquake Engineering, 188, 109072.